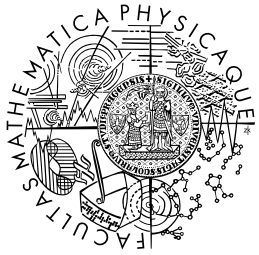

FACULTY
OF MATHEMATICS
AND PHYSICS
Charles University

DOCTORAL THESIS

Tomáš Duchoň

Electronic and structural properties of model catalysts based on cerium oxide

Department of Surface and Plasma Science

Supervisor of the doctoral thesis:	RNDr. Kateřina Veltruská, CSc.
Study programme:	Physics
Study branch:	F-4 Surface and Interface Physics

Prague 2017

I declare that I carried out this doctoral thesis independently, and only with the cited sources, literature and other professional sources.

I understand that my work relates to the rights and obligations under the Act No. 121/2000 Sb., the Copyright Act, as amended, in particular the fact that the Charles University has the right to conclude a license agreement on the use of this work as a school work pursuant to Section 60 subsection 1 of the Copyright Act.

In ..... date ..... signature of the author

Title: Electronic and structural properties of model catalysts based on cerium oxide

Author: Tomáš Duchoň

Department: Department of Surface and Plasma Science

Supervisor: RNDr. Kateřina Veltruská, CSc., Department of Surface and Plasma Science

Abstract: Catalysts based on cerium oxide are ubiquitous in industrial-scale chemical conversion. Here, a thorough study of their fundamental properties is undertaken via a model system approach with the goal of furthering rational design in heterogeneous catalysis. A focus is put on understanding the behavior of oxygen vacancies in cerium oxide with respect to atomic co-ordination and electronic structure perturbations. Utilizing state-of-the-art probing techniques, a scalable model system framework is developed that allows for control over both the oxygen vacancy concentration and local co-ordination. High precision of the innovative approach facilitated observation of new phases of substoichiometric cerium oxide and lead to a first-of-a-kind investigation of the electronic structure of cerium oxide throughout isostructural transition from CeO_2 to Ce_2O_3. The acquired results advance fundamental understanding of essential properties of cerium oxide that are relevant to its utilization in heterogeneous catalysis and open new pathways for functionalization of cerium oxide-based materials. Furthermore, the methodology developed in the thesis is transferable to other important reducible oxides.

Keywords: heterogeneous catalysis, cerium oxide, oxygen vacancies, photoemission spectroscopy

There are many people who, either directly or indirectly, shape a work of the scale of a doctoral thesis. Here, I would like to thank each and every one who has helped me across the finish line.

First and foremost, I would like to thank my supervisor, Dr. Kateřna Veltruská, for the guidance and encouragement she has provided throughtout my studies. I am especially grateful for the working environment she has fostered, that allowed me to freely explore seemingly random ideas without the worry of getting lost in the dark. It has been an invaluable learning experience. I would also like to thank all the people from the Surface Science Group with whom I had the pleasure to work with. Especially, Dr. Marie Aulická, for keeping my sanity in check; Dr. Filip Dvořák, for STM data that considerably improved my manuscript [1]; Mgr. Miroslav Kettner, for keeping the fluorine dream alive; Prof. Vladimír Matolín, for giving me the opportunity to do science on the international stage. **Děkuji!**

Many thanks belong to the CRS group at Brookhaven National Laboratory for their hospitality during my stay—Dr. José A. Rodriguez; Dr. Zongyuan Liu; Dr. Dario J. Stacchiola. I would like to especially thank Dr. Sanjaya D. Senanayake for fruitful collaboration that will hopefuly continue into the future. Many thanks also go to Prof. Ye Xu, and his group at LSU, for the countless discussions we had, which resulted in a work we can be proud of. **Thank you!**

I would like to thank the Surface Physics Group at University of Bremen who welcomed me with open arms—Prof. Jens Falta; Dr. Jan Ingo Flege. Special thanks go to Dr. Jan Höcker, who rekindled my passion for science and accompanied me on one of the best experiments I ever did. I am also grateful for the hospitality of the Peter Grünberg Institute—Prof. Claus M. Schneider, Dr. Stefan Cramm, Ms. Johanna Hackl; and Slavomír Nemšák, who has carried the figurative torch of my alma mater to faraway lands. **Vielen Dank!**

I would also like to thank Prof. Kenya Shimada, Dr. Hideaki Iwasawa and Dr. Eike F. Schwier from HiSOR for showing me that people still care about good science, even when it no longer seem that the honorable pursuit of knowledge is the driving force. ありがとうございます。

I would like to thank the Materials, Environment and Energy Group at University of Trieste—Prof. Paolo Fornasiero, Dr. Tiziano Montini, Dr. Matteo Monai—for introducing me to the world of real chemistry. **Molte grazie!**

Last but not least, I would like to thank my family for their unequivocal support. They carry most of the burden that comes with following the narcissistic dream that is a career in science. 家族は、僕の生き甲斐。サーラちゃんとハナちゃんとズザナちゃんは愛してる。精一杯で支える！

Complete list of publications of Tomáš Duchoň

1. **Duchoň T.**, Hackl J., Höcker J., Veltruská K., Matolín V., Falta J., Cramm S., Nemšák S., Schneider C. M., Flege J. I., Senanayake S. D. (2017): *Exploiting micro-scale structural and chemical observations in real time for understanding chemical conversion: LEEM/PEEM studies over CeO_x–Cu(111).* In: Ultramicroscopy [article in press]. DOI: 10.1016/j.ultramic.2017.05.003. Published online: May 10, 2017.

2. **Duchoň T.**, Aulická M., Schwier E. F., Iwasawa H., Zhao C., Xu Y., Veltruská K., Shimada K., Matolín V. (2017): *Covalent versus localized nature of 4f electrons in ceria: resonant angle-resolved photoemission spectroscopy and density functional theory.* In: Physical Review B 95, 165124.

3. Lykhach Y., Figueroba A., Skála T., **Duchoň T.**, Tsud N., Aulická M., Neitzel A., Veltruská K., Prince K. C., Matolín V., Neyman K. M., Libuda J. (2017): *Redox-mediated conversion of atomically dispersed platinum to subnanometer particles.* In: Journal of Materials Chemistry A 5, 9250–9261.

4. Luo J., Monai M., Wang C., Lee J. D., **Duchoň T.**, Dvořák F., Matolín V., Murray C. B., Fornasiero P., Gorte R. J. (2017): *Unraveling the surface state and composition of highly selective nanocrystalline Ni–Cu alloy catalysts for hydrodeoxygenation of HMF.* In: Catalysis Science & Technology 7, 1735–1743.

5. Monai M., Montini T., Melchionna M., **Duchoň T.**, Kúš P., Chen C., Tsud N., Nasi L., Prince K. C., Veltruská K., Matolín V. , Khader M. M., Gorte R. J., Fornasiero P. (2017): *The effect of sulfur dioxide on the activity of hierarchical Pd-based catalysts in methane combustion.* In: Applied Catalysis B: Environmental 202, 72–83.

6. Kettner M., Ševčíková K., **Duchoň T.**, Kúš P., Rafaj Z., Nehasil V. (2016): *Morphology and CO oxidation reactions on anion doped CeO_XF_Y/Rh(111) and CeO_X/Rh(111) inverse catalysts.* In: Journal of Physical Chemistry C 120, 26782–26792.

7. Liu Z., **Duchoň T.**, Wang H., Grinter D. C., Waluyo I., Zhou J., Liu Q., Jeong B., Crumlin E. J., Matolín V., Stacchiola D. J., Rodriguez J. A., Senanayake S. D. (2016): *Ambient pressure XPS and IRRAS investigation of ethanol steam reforming on Ni–CeO_2(111) catalysts: an in situ study of C–C and O–H bond scission.* In: Physical Chemistry Chemical Physics 18, 16621–16628.

8. Höcker J., **Duchoň T.**, Veltruská K., Matolín V., Falta J., Senanayake S. D., Flege J. I. (2016): *Controlling heteroepitaxy by oxygen chemical potential: exclusive growth of (100) oriented ceria nanostructures on Cu(111).* In: Journal of Physical Chemistry C 120, 4895-4901.

9. Monai M., Montini T., Melchionna M., **Duchoň T.**, Kúš P., Tsud N., Prince K. C., Matolín V., Gorte R. J., Fornasiero P. (2016): *Phosphorus poisoning during wet oxidation of methane over Pd@CeO_2/graphite model catalysts.* In:

Applied Catalysis B: Environmental 197, 271–279.

10. Liu Z., **Duchoň T.**, Wang H., Peterson E. W., Zhou Y., Luo S., Zhou J., Matolín V., Stacchiola D. J., Rodriguez J. A., Senanayake S. D. (2015): *Mechanistic insights of ethanol steam reforming over Ni–CeO_x(111): the importance of hydroxyl groups for suppressing coke formation.* In: Journal of Physical Chemistry C 119, 18248–18256.

11. Carrasco J., López-Durán D., Liu Z., **Duchoň T.**, Evans J., Senanayake S. D., Crumlin E. J., Matolín V., Rodriguez J. A., Ganduglia-Pirovano M. V. (2015): *In situ and theoretical studies for the dissociation of water on an active Ni/CeO_2 vatalyst: importance of strong metal–support interactions for the cleavage of O–H bonds.* In: Angewandte Chemie International Edition 54, 3917–3921.

12. Aulická M., **Duchoň T.**, Dvořák F., Stetsovych V., Beran J., Veltruská K., Mysliveček J., Mašek K., Matolín V. (2015): *Faceting transition at the oxide–metal interface: (13 13 1) facets on Cu(110) induced by carpet-like ceria overlayer.* In: Journal of Physical Chemistry C 119, 1851–1858.

13. Růžička J., Caha O., Holý V., Steiner H., Volobuiev V., Ney A., Bauer G., **Duchoň T.**, Veltruská K., Khalakhan I., Matolín V., Schwier E. F., Iwasawa H., Shimada K., Springholz G. (2015): *Structural and electronic properties of manganese-doped Bi_2Te_3 epitaxial layers.* In: New Journal of Physics 17, 013028.

14. **Duchoň T.**, Dvořák F., Aulická M., Stetsovych V., Vorokhta M., Mazur D., Veltruská K., Skála T., Mysliveček J., Matolínová I., Matolín V. (2014): *Comment on "Ordered phases of reduced ceria as epitaxial films on Cu(111)".* In: Journal of Physical Chemistry C 118, 5058–5059.

15. **Duchoň T.**, Dvořák F., Aulická M., Stetsovych V., Vorokhta M., Mazur D., Veltruská K., Skála T., Mysliveček J., Matolínová I., Matolín V. (2014): *Ordered phases of reduced ceria as epitaxial films on Cu(111).* In: Journal of Physical Chemistry C 118 J. Phys. Chem. C 118, 357–365.

16. Stetsovych V., Pagliuca F., Dvořák F., **Duchoň T.**, Vorokhta M., Aulická M., Lachnitt J., Schernich S., Matolínová I., Veltruská K., Skála T., Mazur D., Mysliveček J., Libuda J., Matolín V. (2013): *Epitaxial cubic Ce_2O_3 films via Ce–CeO_2 interfacial reaction.* In: Journal of Physical Chemistry Letters 4, 866–871.

Contents

1. Introduction

Catalysis is an effective tool allowing us to cope with the ever increasing production demand dictated by rising population. Its significance is perhaps best illustrated by the importance of the Haber-Bosch process, without which the population boom of the 20$^{\text{th}}$ century would turn into a worldwide famine. The same bleak picture would be painted by the absence of public and personal transportation that made the increased population somehow sustainable — there the connection with catalysis lies in a complete dependence of the automotive industry on fluid catalytic cracking for fuel production and on three-way (formerly two-way) catalysis for detoxication of exhaust fumes. In the 21$^{\text{st}}$ century catalysis is poised to power the fuel cell technology, even on the micro level with on-chip fuel cells, and thrives in multitude of other industrial branches. However, the illustrious role of catalysis is tainted by its consumption of materials that are found in the Earth's crust only in limited amounts. This makes, for example, precious metals materials of extreme strategic importance, especially considering localization of their distribution throughout the world. The pursuit of efficiency in catalysis is thus not only motivated by noble reasons of self-preservation and sustainability, but initiated by a lowly political currents, too.

1.1 Heterogeneous catalysis

Catalysts are materials that change rates of chemical reactions without being expended in the process. A catalyst basically acts as an electronic perturbation that affects energy barriers between various transition states of a chemical reaction. The effect can be so large that it alters the path of the reaction. Understanding the interaction between reactants and the catalyst is therefore of utmost importance for rational design of chemical conversion. Many of the crucial industrial catalytic reactions are heterogeneous, where the catalyst and reactants are in a different phase [2]. Typically, the catalyst is a solid and the reactants are either in a liquid or gas phase. The heterogeneous catalysis can be described in several steps. First, the reactants have to be transported towards active sites of the catalyst. The reactants either directly adsorb on the active sites or diffuse to the active sites across the surface of the catalyst. Second, the reactants are activated (i.e., dissociated) on the active sites. Finally, a reaction occurs and the products desorb from the catalyst. The reaction at the catalyst can occur either between two reactants adsorbed on the catalyst (Langmuir–Hinshelwood mechanism), or an adsorbed one and a gas phase one (Eley–Rideal mechanism). Alternatively, the activated reactants can be transported away and the reaction can occur on a different catalyst or purely in the gas phase. It is important to note that constituents of the catalyst's lattice can also directly participate in the reaction and leave the surface (Mars and Van Krevelen mechanism [3]), which is especially relevant for chemical conversion over oxide-based catalysts. The Mars and Van Krevelen mechanism is schematically illustrated on the case of CO oxidation over a model Cu-CeO_x catalyst in Figure 1.1.

The above-mentioned mechanisms highlight two important concepts in heterogeneous catalysis represented by the surface and the active sites. Because

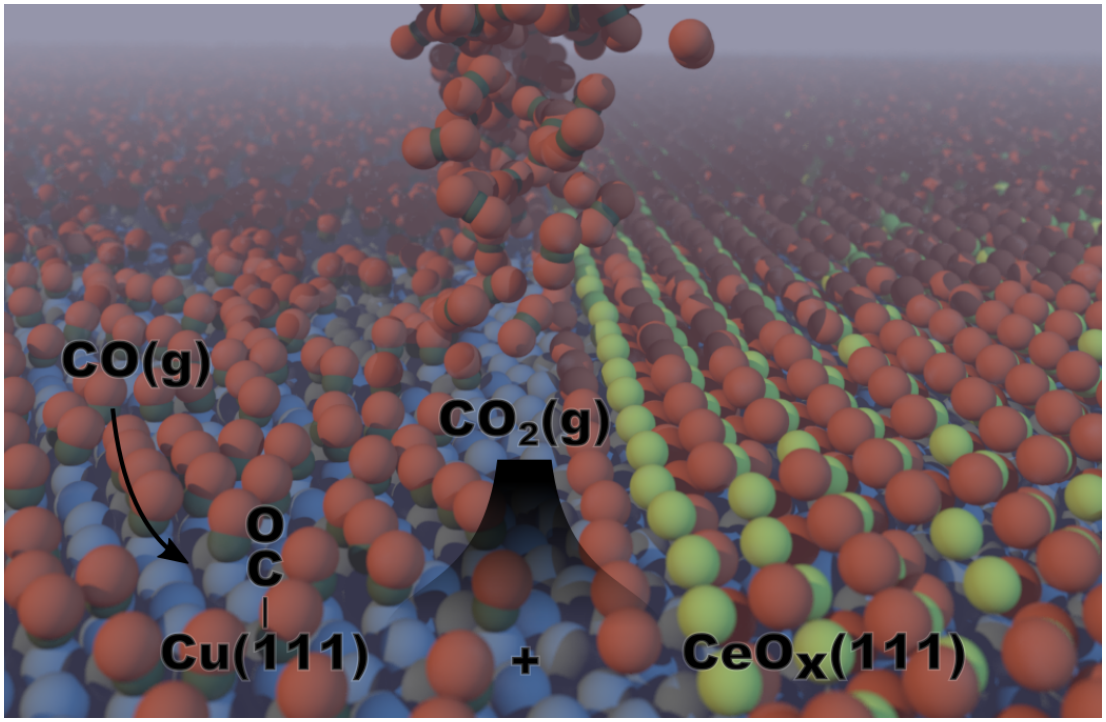

Figure 1.1: Catalytic oxidation of CO to CO_2 on an inverse CeO_x/Cu(111) catalyst. The oxygen for the reaction is supplied by the doped cerium oxide.

the processes constituting heterogeneous catalytic conversion take place at the surface of the catalyst, the surface-area-to-volume ratio largely determines cost efficiency of the materials making up the catalyst. In practice, this leads to size reduction (nanopowders) or core shell design, which can approach the ideal surface-area-to-volume ratio of a hollow sphere. However, the number of available surface sites does not correspond to the number of sites where rate-determining catalytic processes take place [4]. In fact, the active sites are usually the minority, often with orders of magnitude lower concentration — terrace steps, structural defects, doping agents, etc. A fundamental understanding of what makes specific sites catalytically active in a given reaction is the holy grail of rational design of future-proof catalytic materials.

1.2 Model approach to catalysis

The path towards consistent descriptors of active sites in heterogeneous catalysis is a difficult one. The problem lies in the incredible complexity of the industrially utilized catalysts. These are often powder-type materials that exhibit astonishing structural variety that prohibits any interpretation with respect to individual structural features. Furthermore, catalytic materials regularly feature complex phase diagrams, which makes underlying principles determining their activity much more intricate due to possible phase transitions accompanied by changes of local coordination, long-range ordering and surface termination. In order to make any fundamental insights obtainable singular structural features have to be isolated in such a manner that they can be probed by existing experimental techniques. This is the goal of the field of model heterogeneous catalysis [5].

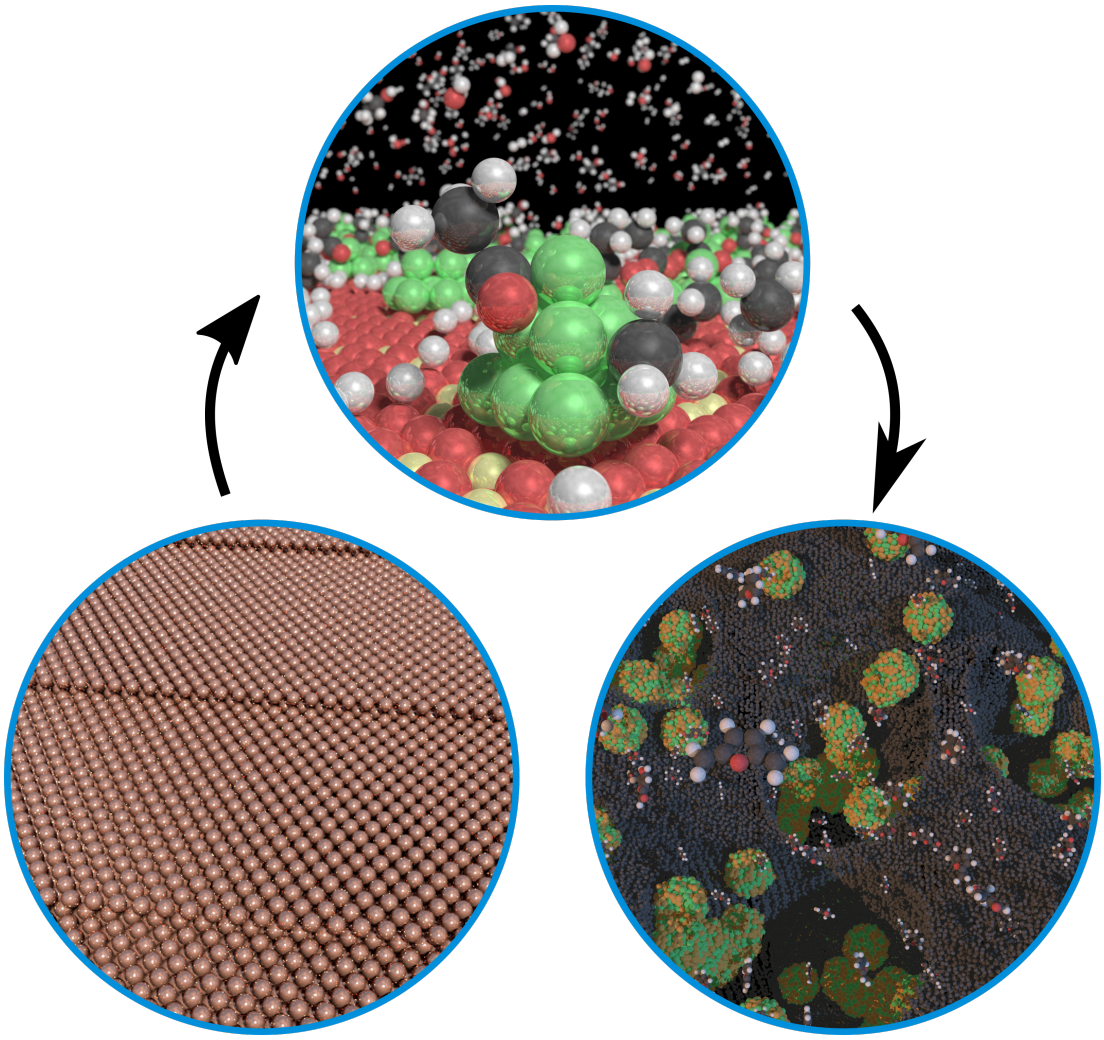

Figure 1.2: Schematic illustration of the bottom-up approach to heterogeneous catalysis, starting from single crystal studies and building up to complex nanopowders.

Model catalysis represents a bottom-up approach to understanding heterogeneous catalysis, where one starts from as simple a system as possible and gradually builds up towards more complex systems (see Figure 1.2). Model catalysts are often prepared in the form of epitaxial films grown on single crystal surfaces, with the first goal being thorough investigation of low-index surface terminations of the materials constituting the catalyst. The complexity of the system is than scaled up by introducing perturbations, such as defect sites, doping agents, extended interfaces, and so on. Finally, the knowledge obtained on the singular surface terminations is put together and used to model a catalyst comprised of a combination thereof. While this is obviously only an approximation of the real catalyst, the predictive capability of the model system approach has proven to be valuable.

One of the biggest benefits of the model system approach is that it enables the use of robust probing techniques of surface science. These provide access to the atomic and electronic structure, magnetic properties, bonding character, chemical interaction, and many other properties of interest. Most of the techniques also operate under ultra-high vacuum (UHV) conditions, which are in line with the high demands of the model system approach regarding purity of the materials and suppression of contamination. However, the UHV conditions also impose serious limitation on scalability of the studied chemical interactions. No industrial reaction operates under UHV conditions and the energetics of chemical reactions exhibit a non-trivial dependence on pressure of the reactants, as does the phase diagram of catalytic materials. Still, the model system approach represents a unique playground for investigation of the fundamental properties of catalytic materials.

1.3 Reducible oxides

Reducible oxides represent an important class of catalytic materials that forms the foundation of various indispensable industrial processes closely related to sustainable energy. The unique properties of reducible oxides are widely utilized in energy storage and conversion, hydrogen economy being the most prominent example. Other notable applications include catalytic conversion of pollutants, such as automobile exhaust gases, and biomedical industry [6, 7]. Reducible oxides typically function as an oxygen sink / source through a reduction–oxidation (redox) cycle between several stable stoichiometries. The ability to supply or absorb oxygen allows them to balance oxygen lean and oxygen rich phases of chemical conversion, greatly enhancing both stability and yield of reactions. The utility of reducible oxides is, however, not limited to a passive support role, as both cations and anions constituting the oxide can actively participate in various processes [8]. The active role is defined through the electron configuration of the valence shell of the respective ions. Here, the redox cycle generates a remarkably complex array of possibilities by allowing reducible oxides to dramatically alter the occupancy of the valence shell. This is especially relevant for reducible oxides that change the highest occupied subshell (s, p, d or f) of the cation during the redox cycle—d electrons for transition metal based oxides and f electrons for rare-earth oxides. The unique properties and wide application potential have made reducible oxides subject of a large body of scientific work, covering both

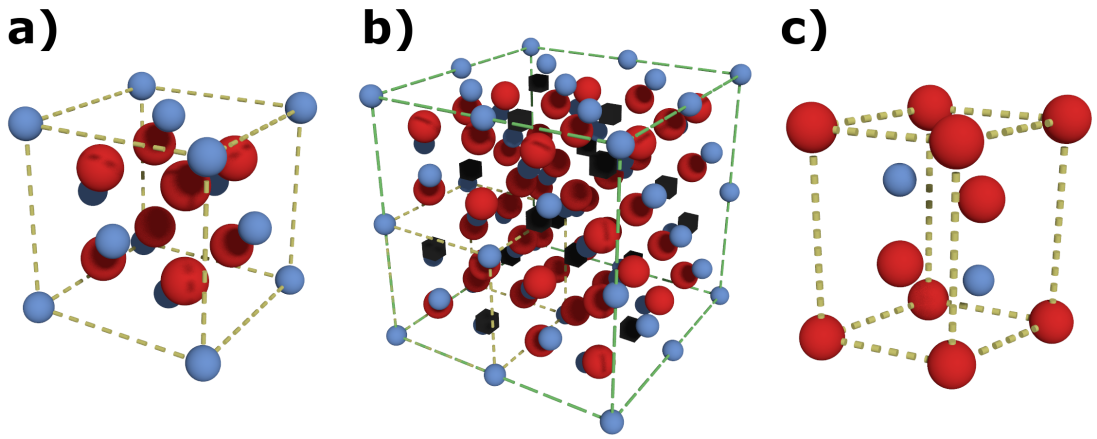

Figure 1.3: Models of stoichiometric phases of cerium oxide: a) CeO_2 (Fm-3m, $a = 5.41$ Å), b) c-Ce_2O_3 (Ia-3, $a = 10.98$ Å), and c) a-Ce_2O_3 (P-3m1, $a = 3.89$, $c = 6.06$ Å). Cerium ions are shown in blue and oxygen ions in red. The unit cell is highlighted by a dashed line. In the case of c-Ce_2O_3 the unit cell of CeO_2 is also shown, along with oxygen vacancies (black cubes), to highlight the relation between the two.

basic research conducted on model systems and applied research on industrial materials [6, 7].

1.4 Cerium oxide

Cerium oxide is a reducible rare-earth oxide that has become a mainstay in catalytic applications where oxygen storage and dissociation of water are essential—i.e., in steam reforming reactions. The redox properties of cerium oxide are facilitated by a low energy barrier for oxygen vacancy formation, high oxygen vacancy mobility, and exothermic reoxidation (cerium metal is pyrophoric). The redox cycle is established between two stable stoichiometries, CeO_2 and Ce_2O_3, that manifest themself in a nominal cation oxidation state of Ce^{4+} and Ce^{3+}. Understanding cerium oxide is thus closely related to understanding structural and electronic changes occurring between the two configurations.

CeO_2 crystallizes in a fluorite structure (Fm-3m) with a bulk lattice parameter of 5.41 Å and cubically (8-fold) coordinated cations (see Figure 1.3(a)). It exposes three low-index surfaces — (111) > (110) > (100), ranked in the order of stability (see Figure 1.4). Reflecting the stability, the (111) surface has been the subject of the largest amount of studies [10]. However, there has recently been a surge of interest in the other two surfaces given their prevalence in nanostructured cerium oxide materials [11, 12]. The (100) surface is especially interesting due to polarity of the bulk termination that gives rise to various surface reconstructions, that have not been deciphered as of yet (see Figure 1.5). The structures of the other two surfaces are well-established.

Oxygen vacancies in cerium oxide are generally more stable at the surface than in the bulk [13]. This is effectuated by oxygen vacancy induced strain that is more easily dissipated at the surface. The strain is closely related to the most significant feature of the cerium oxide redox cycle. Following from

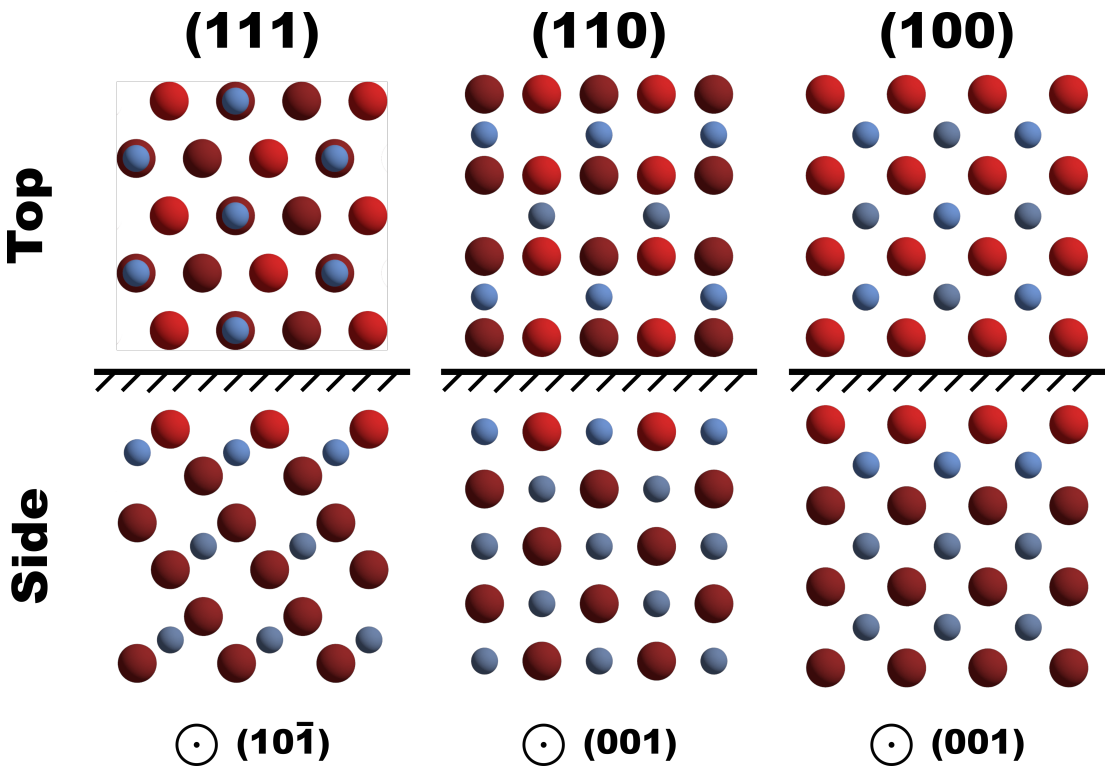

Figure 1.4: Models of low-index surface terminations of CeO_2. Cerium ions are shown in blue and oxygen ions in red.

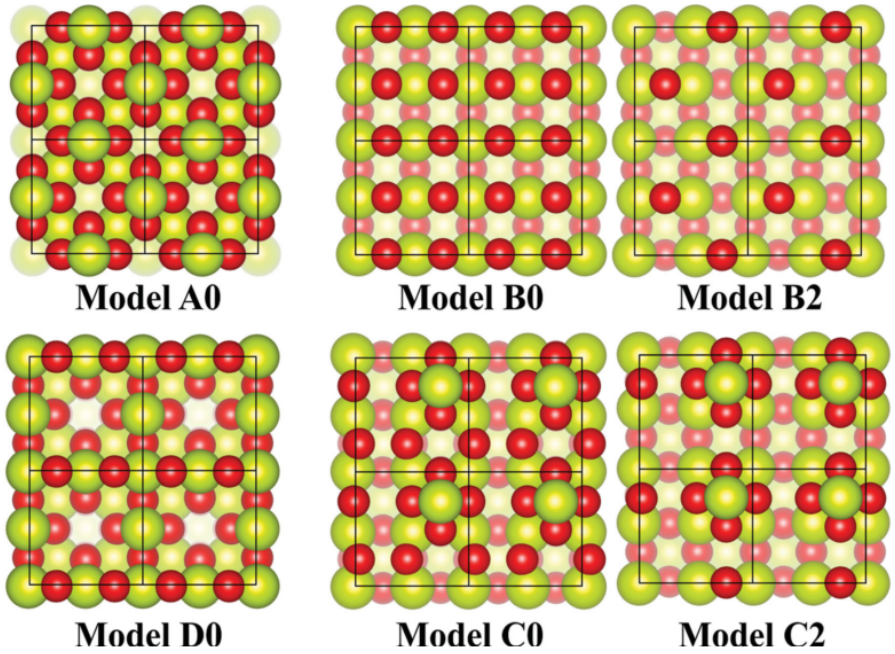

Figure 1.5: Various models of polarity compensated stoichiometric (A0–D0) and substoichiometric (B2, C2) (100) surface of cerium oxide. Cerium ions are shown in yellow and oxygen ions in red. The black solid lines indicate (2×2) unit cells. [9]

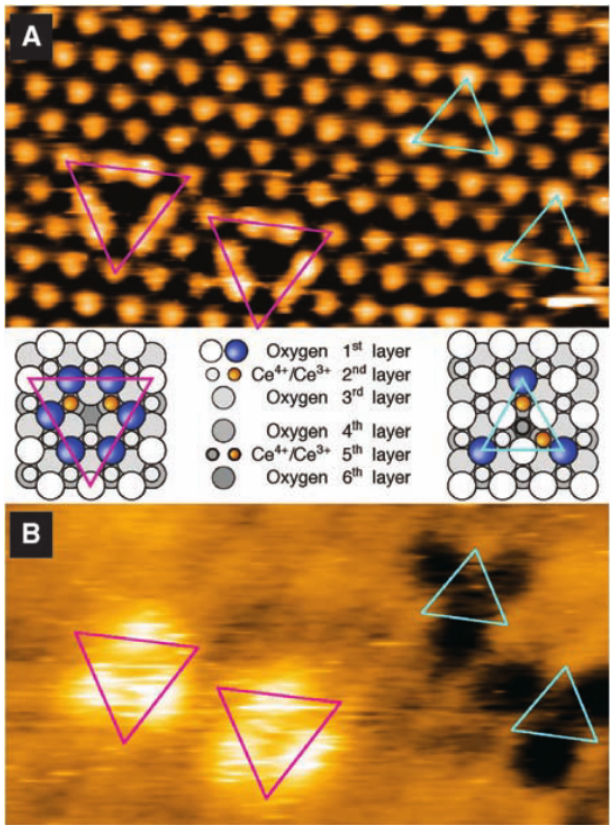

Figure 1.6: High resolution filled-state (a) and empty-state (b) STM images of defects on the $CeO_x(111)$ surface along with models for f electron localization proposed by Esch et al. [15]

the nominal ionic configuration of oxygen and cerium, a formation of an oxygen vacancy in CeO_2 leaves behind two electrons that were filling the oxygen *2p* shell. Quantum chemical calculations show that the two excess electrons localize in f shells of surrounding cerium ions [13]. One has to appreciate that the occupation of the highly-localized f orbital is a considerable electronic perturbation. In regards to the above-mentioned strain, the f electron increases the ionic radius of the cerium ion it localizes at. The corresponding changes in bond lengths than lead to local lattice expansion that is the source of the strain. This has been the established interpretation of both a reduction induced lattice expansion and surface localization of oxygen vacancies in cerium oxide [6]. However, the interpretation might be overly simplistic. If one bases the explanation purely on ionic radius changes, the ionic radius increase of the cerium ion is overshadowed by the missing oxygen ion, whose ionic radius is even larger [14]. This leads one to conclude that a repulsion of the positive defects (the oxygen vacancies) is the deciding factor [14]. Still, the position of the localized f electrons with respect to the position of the oxygen vacancy is essential for understanding the accompanying structural relaxation.

A seminal work on this topic has been published by Esch et al. [15]. They report on a high-resolution scanning tunneling microscopy (STM) study of defects on the (111) surface of cerium oxide. The contrast of the observed defects is interpreted in conjunction with density functional theory (DFT) calculations, revealing that f electrons tend to localized at the nearest neighbor cerium ions

with respect to the oxygen vacancy position (see Figure 1.6). This experimental observation is consistent with a large body of quantum theoretical calculations that predict the same behavior [16]. However, there are two perplexing inconsistencies in the data. First, the defects observed by Esch et al. tend to cluster at elevated temperature, and, second, the defects are located in the surface layer. Oxygen vacancies are actually known to repel each other in the bulk of cerium oxide [17] and to prefer sub-surface layer of the (111) surface [18]. Indeed, the defects observed by Esch et al. have been shown to match the behavior of fluorine impurities [19], invalidating the electron localization picture in cerium oxide that has been propagating through the literature for the past decade. While it may seem a pointless exercise to reiterate the mistake in here, it actually serves as a very good illustration of the importance of the oxygen vacancy induced strain. Specifically, the supercells used in the calculations that predict localization of electrons at the nearest neighbor cerium ions were too small to account for the structural distortion. Calculations with larger supercells consequently revealed the problem, showing that the f electrons prefer to localize at next-nearest neighbor cerium ions [18, 19].

Here, it should be noted that the description of cerium oxide through DFT is complicated by the occupied atom-like localized f orbitals in reduced cerium oxide. The reason for this lies in the self-interaction error (SIE) intrinsic to local-density Approximation (LDA) and generalized gradient approximation (GGA) approaches to DFT. The problem arises due to incomplete cancellation of the self-interaction Coulomb term for electrons localized near nuclei, which is caused by the approximate nature of the correction of exchange interaction in both LDA and GDA. As a result the electrons tend to be overdelocalized (see Figure 1.7). In the case of excess electrons left behind after creation of an oxygen vacancy in CeO_2, the electrons would not populate the 4f orbitals with integer occupation numbers and instead, due to SIE, spread out over many cerium ions leading to a fractional occupation of the *4f* orbitals [13]. A commonly used approach to remedy the problem is DFT+U, named so as it adds a correction term called Hubbard-U term to the used functionals. Generally, the Hubbard model leverages the tight-binding approximation from solid state physics, where electrons are viewed as occupying the standard orbitals of ions and conduction is viewed as *hopping* (*tunneling*) of these electrons between the ions. Practically, there is a competition between the *hopping* and on-site Coulomb repulsion between electrons in the same orbital. The dominance of these terms reflects the transition between metal and insulator in the Hubbard model. DFT+U thus presents an extension to DFT that considers the on-site interaction from the Hubbard model in the form of the U-term, which describes the behaviour of a system of electrons based on their localization as an additional correcting interaction. Here, an important issue arises — the U-term is principally material dependent and the correct value is generally not known. While there are various ways how to approach this problem, two essential aspects should be highlighted. First, due to the nature of the U-term it is not possible to distinguish a situation where two electrons are localized on two ions from a situation where both of these electrons are delocalized over the same ions. Second, localization introduced through the U-term is arbitrary in the sense that it is done in order to arrive at a solution that satisfies our expectation. These issues are carried over to the more advanced hybrid density functionals, where the degree of

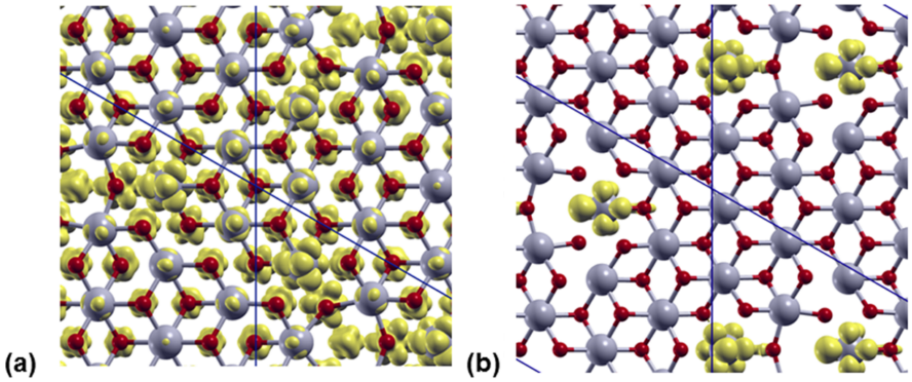

Figure 1.7: Spin density (yellow) around an oxygen vacancy calculated using LDA (a) and hybrid density functional (b). The self-interaction leads to delocalization of f electrons in the case of LDA, while the hybrid density functional calculation results in two localized f electrons. [13]

Fock exchanges is the new parameter. While the expectations are usually based on experimental observation, there are indications that f electrons can also exist in cerium oxide in a delocalized form [20]. Still, being mindful of the above-mentioned problems, DFT is a powerful tool for investigation of properties of cerium oxide.

Returning to the oxygen vacancies at the surface of cerium oxide, the work carried out so far on the (111) surface established the following: a) oxygen vacancies are preferentially located in the sub-surface layer, b) oxygen vacancies repel each other and consequently do not tend to cluster, and c) electrons generated by oxygen vacancy formation favor localization at next-nearest neighbor cerium ions. The other two low-index surfaces, (110) and (100), accommodate oxygen vacancies in the surface layer. The anisotropic structure of the (110) surface (see Figure 1.4 leads to a large relaxation of the oxygen ion neighboring the oxygen vacancy and localization of the f electrons on a nearest neighbor and next-nearest neighbor cerium ions [21]. Oxygen vacancies on the (100) surface have the lowest formation energy [22, 23] and allow for compensation of the dipole moment of the bulk termination, giving rise to structural reorganization that is not yet well understood [9].

Given the above mentioned tendencies of oxygen vacancies, especially the repulsion, it is very likely that high concentration of these will lead to a preferential ordering. This is reflected in the complex phase diagram of cerium oxide [24] and confirmed by bulk diffraction studies [17]. Interestingly, the oxygen lean part of the phase diagram is occupied by two stable structures, a hexagonal h-Ce_2O_3 (P-32/m1) and a cubic c-Ce_2O_3 (Ia-3) (see Figures 1.3(b) and (c)) [25]. While the hexagonal phase is expected to be the thermodynamically stable one as it is the phase that is present in high-temperature treated cerium oxide materials [26], the cubic phase is seen as the ideal representation of the reduction of CeO_2 without structural modification of the cerium ion sublattice. However, experimental data on either phase is lacking as they have not been successfully stabilized in the form of long-range ordered surfaces that would allow for precise atomic and electronic structure investigations. Particularly, the changes in bonding character in the transition from CeO_2 to Ce_2O_3 are poorly understood.

The most successful approach to study properties of cerium oxide in relation to its catalytic applications has been the utilization of epitaxial films. Growing thin epitaxial films of cerium oxide allows to obtain well ordered surfaces and mitigates charging problems, due to cerium oxide being in insulator, of various electron based techniques. Epitaxial films of cerium oxide exposing the (111) surface have been successfully grown on many metal single crystals, such as Ru(0001) [27], Ni(111) [27], Rh(111) [28], Pt(111) [29], Pd(111) [30], and Cu(111) [31]. The other two low-index surfaces are limited to singular studies of the (100) terminated films grown on $SrTiO_3$(100) [32]. In this thesis, cerium oxide films grown on Cu(111) will be utilized as a model of the (111) surface. Cerium oxide grows epitaxially on Cu(111) with a nearly perfect lattice coincidence of ≈ 1.5. However, the lattice parameter of the film is governed more by size effects than the lattice coincidence due to a very weak coupling with the metal substrate [33]. The growth process is diffusion limited, with the growth temperature determining ordering of the film [34]. The temperature dependence can be exploited in preparation of films with controllable terrace size (step density) [34]. Importantly, the films can be prepared continuous, mitigating influence of the substrate [31]. Finally, it should be mentioned that the actual interface between Cu(111) and cerium oxide is still under debate. Specifically, a possible presence of CuO_x at the interface has been hinted on [35], which would invalidate theoretical models predicting charge transfer at the interface [36].

1.5 Scope of the thesis

The thesis focuses on furthering the fundamental understanding of structural and electronic properties of cerium oxide in relation to the $CeO_2 \leftrightarrow Ce_2O_3$ redox pair.

The overarching goal is to understand electronic structure modifications arising through defect formation in cerium oxide and the associated filling/emptying of the *4f* shell. Towards that goal a development of robust scalable framework of cerium oxide model systems is undertaken, whose purpose is to allow flexible control over local co-ordination of cerium ions in cerium oxide.

2. Experimental

This section introduces experimental methods utilized throughout the thesis along with practicalities of data processing. A focus is put on photoemission spectroscopy as the method that has been taken advantage of the most.

2.1 Photoemission spectroscopy

Photoemission spectroscopy is a mature analytical method whose history spans two Nobel Prizes (Albert Einstein, 1921; Kai Siegbahn, 1981). The development of photoemission spectroscopy is closely tied to the revolution in physics at the beginning of the twentieth century which led to transition from classical physics to quantum physics. The method is based on interaction of photons with matter that results in emission of an electron, a process known as photoemission. The emitted electron, called a photoelectron, caries a lot of information that can be accessed in various ways. At the most basic level, photoemission can be expressed in the form of Fermi's golden rule:

$$w_{fi} = \frac{2\pi}{\hbar} | < \mathbf{\Psi_f} | H^{int} | \Psi_i > |^2 \rho, \tag{2.1}$$

where w_{fi} is the transition probability from the initial state $|\Psi_i>$ to the set of final states $<\mathbf{\Psi_f}|$, $\hbar$ is reduced Planck constant, H^{int} is the perturbation due incident photons, and ρ is the density of final states.

This elegant expression illustrates many of the intricacies of photoemission. However, the apparent simplicity disappears as soon as one recognizes that the wavefunctions in the equation are many-electron wavefunctions of a semi-infinite crystal, with the final state wavefunctions including a component of a plane wave in the vacuum region with a finite amplitude in the crystal. Fortunately, several approximations can be made that greatly simplify the expression and allow to illustrate practical aspects of photoemission spectroscopy. Let's first concern ourselves only with a transition to a specific final state due to interaction with monochromatic photons. The expression reduces to:

$$w_{fi} = \frac{2\pi}{\hbar} | < \Psi_f | H^{int} | \Psi_i > |^2 \delta(E_f - E_i - h\nu), \tag{2.2}$$

where $E_f - E_i$ is the energy difference between states $<\Psi_f|$ and $|\Psi_i>$, and $h\nu$ is the energy of the photons. Now, we will account for the effect of the incident photons by treating the external electromagnetic field classically and utilizing Coulomb gauge ($\mathbf{\Phi} = 0$, $\vec{\nabla} \cdot \vec{A} = 0$). A non-relativistic system obeys the "free" Schrödinger equation:

$$H_0 \Psi_0 = (\frac{p^2}{2m} + V(r))\Psi_0 = E\Psi_0, \tag{2.3}$$

where $\vec{p}$ is the momentum operator, m is the electron rest mass, $V(r)$ is the scalar potential, and E is the energy of the state Ψ_0. We include the interaction with the external electromagnetic field by adding the vector potential to the momentum in H_0:

$$H_0 = (\frac{1}{2m}(\vec{p} + \frac{e}{c}\vec{A})^2 + V(r)), \tag{2.4}$$

where c is the speed of light, and $\vec{A}$ is the vector potential of the external electromagnetic field. The square bracket in the expression is expanded as follows:

$$(\vec{p} + \frac{e}{c}\vec{A})^2 = p^2 + \frac{e}{c}\vec{A}\cdot\vec{p} + \frac{e}{c}\vec{p}\cdot\vec{A} + \frac{e^2}{c^2}|\vec{A}|^2. \tag{2.5}$$

The perturbation due to the incident photons can now be written to the first order in $\vec{A}$ as:

$$H^{int} = \frac{e}{2mc}\vec{A}\cdot\vec{p}. \tag{2.6}$$

The third term in the equation 2.5 disappears due to the Coulomb gauge. Next, we take $\vec{A}$ in the form of a plane wave:

$$\vec{A}(\omega, t) = \vec{\sigma}e^{i(\omega t - \vec{q}\cdot\vec{r})}, \tag{2.7}$$

where ω is the frequency of the photons, t is the time variable, $\vec{\sigma}$ is the polarization of the photons, $\vec{q}$ is the momentum of the photons, and $\vec{r}$ is the coordinate. Finally, we assume that $\vec{A}$ is constant over the lengthscale of atoms (i.e., $\lambda >> r_0$), the so called dipole approximation, which makes $e^{i(\omega t - \vec{q}\cdot\vec{r})} \sim 1$. Combining equations 2.6, 2.7, and 2.2, we arrive at the matrix elements in the dipole approximation:

$$< \Psi_f|H^{int}|\Psi_i >= \frac{e}{2mc}\int \Psi_f^+(\vec{\sigma}\cdot\vec{p})\Psi_i dV. \tag{2.8}$$

It should be noted that while the dipole approximation is generally valid for light sources utilized in photoemission spectroscopy ($>$ 5 eV), we are ignoring both surface emission ($\nabla\cdot\vec{A} = 0$ is not valid at the surface) and quadrupolar matrix elements, which can both play significant role. Nevertheless, equation 2.8 still allows us to explain important concepts in photoemission and make decent predictions. The first of theses is the fact, that the parity of the functions integrated on the right side of equation 2.8 imposes symmetry rules for forbidden transitions. Specifically, if $\Psi_f^+(\vec{\sigma}\cdot\vec{p})\Psi_i$ is odd the integral is zero and consequently w_{fi} (see equation 2.2) is zero. This means that polarization of the incident photons determines states that are accessible in the experiment. We will make one more approximation in order to better illustrate how this works. We will assume that the effective potential changes discontinuously after emission of an electron from an atom. This so called sudden approximation is valid for photoelectrons that are fast enough ($\approx$ 100 eV) to leave the solid before the rest of the electrons relax due to the core hole that is left over. This allows us to separate the many-electron wavefunctions in the following way:

$$\Psi_f = A\Phi_f^k\Psi_f^{N-1}; \Psi_i = A\Phi_i^k\Psi_i^{N-1}, \tag{2.9}$$

where A is the antisymmetrizing operator (in order to fulfill the Pauli exclusion principle), Φ_f^k and Φ_i^k is the wavefunction of the electron that interacts with the incoming photon in the final and initial state, respectively, and Ψ_f^{N-1} and Ψ_i^{N-1}

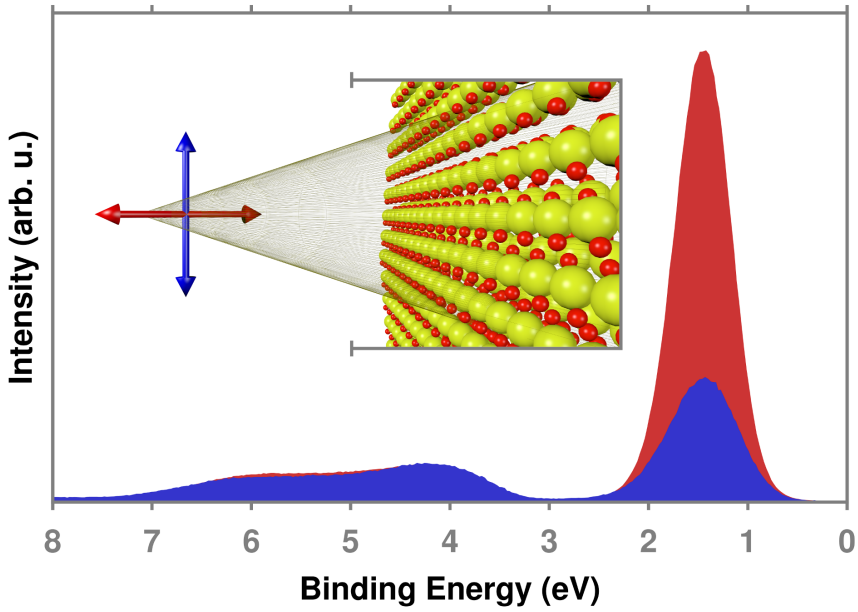

Figure 2.1: The effect of matrix elements illustrated on the valence band spectra of cerium oxide measured with a p and s polarized light.

is the N-1 electron wavefunction of the rest of the system in the final and initial state, respectively. Equation 2.8 now simplifies to:

$$< \Psi_f|H^{int}|\Psi_i >=< \Phi_f^k|H^{int}|\Phi_i^k >< \Psi_m^{N-1}|\Psi_i^{N-1} >= M_{fi}^k c_{mi}, \tag{2.10}$$

It is now obvious that if we know both Φ_f^k and $\vec{\sigma}$ the selection rules specify the parity of accessible Φ_i^k states (see Figure 2.1). In photoemission spectroscopy we can usually approximate Φ_f^k as a free electron, which is satisfied for photoelectrons that transition to states far away from Fermi energy of materials with spherical Fermi surface (i.e., metals). However, the theoretical framework developed above can be also used to describe X-ray absorption spectroscopy (XAS), where this condition is not satisfied and the selection rules have to account for the parity of Φ_f^k states in close proximity to the Fermi energy. Both processes carry important information about the initial state, but here we concern ourselves in greater detail only with photoemission. We now substitute equation 2.10 into 2.2 and sum over final and initial states in order to arrive at a quantity proportionate to photoelectron current of a specific kinetic energy:

$$I(E_{kin}) \sim \sum_{f,i} |M_{fi}^k|^2 \sum_m |c_{mi}|^2 \delta(E_{kin} + E_m^{N-1} - E_i^N - h\nu). \tag{2.11}$$

It is easy to see that for the special case of $\Psi_i^{N-1} = \Psi_m^{N-1}$ in a diagonal c_{mi} the expression on the right side of 2.11 leads to $E_{kin} - h\nu = \epsilon_k$, where ϵ_k is the orbital energy of the Φ_i^k state. This is the basis of elemental sensitivity provided by photoemission spectroscopy, because each element has a specific set of initial states that are reflected in the kinetic energy of photoelectrons through equation 2.11. c_{mi} is, however, rarely diagonal. The N-1 electrons left in the system respond to the core hole, which makes arriving at ϵ_k highly nontrivial,

although it does not alter the rough fingerprint of elements. Interestingly, the response carries information about electronic configuration of the matter, allowing to differentiate chemical state of the element emitting the photoelectron (i.e., the response will be different for a metal or an oxide).

In a crystalline solid the photoelectron also conveys information about the actual band structure (momentum of the electron in the solid). The information is accessible by measuring both the kinetic energy and angular distribution of photoelectrons. Utilizing energy and momentum conservation laws we can write:

$$E_f^k - E_i^k = h\nu; \vec{k_f} - \vec{k_i} = \vec{k_{h\nu}} + \vec{G}, \tag{2.12}$$

where $\vec{k_f}$ and $\vec{k_i}$ is the momentum of the electron in the solid in the final and initial state, $\vec{k_{h\nu}}$ is momentum of the absorbed photon and $\vec{G}$ is the vector of the reciprocal lattice. $\vec{k_{h\nu}}$ is typically negligible (in the energy range where it is not, the momentum of the electrons is so big that band dispersion is actually obscured by averaging over the whole Brillouin zone at room temperature [37]) and $\vec{G}$ is zero in the reduced Brillouin Zone. If we know the final states (either from theory or utilizing free electron approximation) we can reconstruct $\vec{k_i}$. It should be noted that the measured momentum of the photoelectron outside of the solid does not directly correspond to $\vec{k_f}$. While the parallel component of the momentum is identical due to symmetry ($\vec{k_f^{\parallel}} = \vec{K^{\parallel}}$), the perpendicular component of the momentum is modulated by inner potential V_0 (which corresponds to the bottom of the valence band referenced to the vacuum level) and has to be reconstructed from the angular distribution in the following manner (for the free electron approximation):

$$\vec{k_f^{\perp}} = \frac{1}{\hbar}\sqrt{2m(E_{kin}\cos^2\Theta + V_0)}, \tag{2.13}$$

where Θ is the polar angle of the emission with respect to the surface normal. It should be noted that V_0 is generally not know. The strategies to find the value include a) varying the value in order to arrive at an agreement with theoretical calculations, b) using the zero of muffin-tin potential, and c) exploiting symmetry of dispersion in the direction perpendicular to the surface.

The theoretical framework developed in here illustrates the type of information that can be obtained from photoemission spectroscopy. Still, the intricacies of the equations we have arrived at often lead experimentalists to avoid their use in favor of a more empirical approach that is closely connected with the instrumentation. Before we move in the same direction, we briefly look at a slightly more complicated photoemission process that will be utilized in the thesis, a process known as resonant photoemission. Resonant photoemission combines direct photoemission with an Auger decay process to form two channels that lead to identical final state. The Auger decay process can be divided into three steps. First, an inner-shell hole is formed (e.g., by photoemission). Second, the hole is filled by an electron from a higher lying level. Finally, the energy difference between the inner shell and the level from whence the filling electron comes is transferred to another electron, which can escape the solid if the energy is high enough. This can be viewed as an indirect photoemission process. Combining the photoemission and Auger decay processes leads to a new interaction Hamiltonian:

$$H^{int}_{reso} = H^{int} + H^{AI} \sum_n \frac{|\Psi_n >< \Psi_n|}{h\nu + E_i - E_n + i\Gamma_n/2} H^{int}, \tag{2.14}$$

where H^{AI} accounts for the energy transfer through the de-excitation (typically coulombic interaction), Ψ_n is the wavefunction of the intermediate state, E_n is the energy of the intermediate state, and the term $i\Gamma_n/2$ represents lifetime of the intermediate state. The important message of equation 2.14 is the fact that the two processes are put together at the level of the interaction Hamiltonian, which leads to interference when the two final states are not distinguishable. This can be utilized in artificially enhancing the number of photoelectrons emitted from low density states.

Now we step a little bit back and look at the photoemission process through the eyes of an experimentalist. What we want to do is understand equation 2.11 in relation to the experimental setup. Traditionally, the approach to photoemission developed above is known as one-step model of photoemission. We can greatly simplify the process by dividing it into three parts, the so called three-step model of photoemission, in the following manner:

$$I \approx W \cdot S \cdot T, \tag{2.15}$$

where I is the intensity of photocurrent, W is the term describing excitation of an electron in the solid due to incident photons, T is the term describing propagation of the excited electron through the solid, and S is the term describing transmission of the excited electron across the solid / vacuum interface. While the separation into the three processes is a severe approximation, it allows to represent the photoemission process essentially just by three numbers — a photoionization cross-section ($\sim W$), an effective free path ($\sim S$), and a work function ($\sim T$). This is indeed practical, as the values can be tabulated as a function of energy and material. Knowing the values and being able to measure kinetic energy of photoelectrons, one can plot a graph relating number of electrons with a specific orbital energy (photoelectron spectrum) in the solid through a simplified version of the delta function on the right side of equation 2.11:

$$-\epsilon_k = h\nu - E_{kin} - E_r - \Phi_A, \tag{2.16}$$

where E_r is the term accounting for non-zero off-diagonal entries in c_{mi}, and Φ_A is the work function of an analyzer used for the detection of photoelectrons. Φ_A can be used instead of the work function of the material emitting the photoelectrons when the analyzer is conductively connected to the sample. The photoelectrons are then either slowed down or accelerated by the difference in the work function of the analyzer and the sample, further simplifying the interpretation as the work function in equation 2.16 can be calibrated.

Before discussing the information that can be obtained from photoelectron spectra through equations 2.15 and 2.16, let's briefly discuss the energy dependence of the terms W and S in equation 2.15. The energy dependence actually defines several characteristics of the method, which can be roughly separated into three regimes based on the primary photon source — ultraviolet ($\sim$ 100 eV; laser, UV lamp, synchrotron), X-ray ($\sim$ 1000 eV; X-ray source, synchrotron) and hard X-ray ($>$ 2000 eV; X-ray source, synchrotron). First, the photoionization

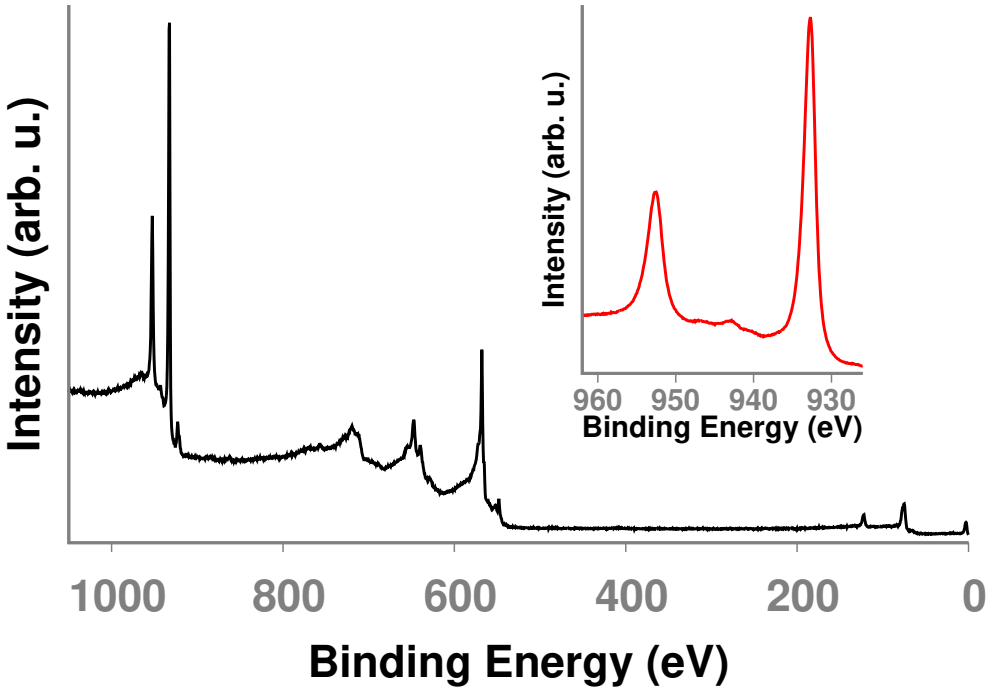

Figure 2.2: Photoelectron spectrum of a copper single crystal acquired with Al K_α X-rays (1486.6 eV). Inset: detail of the Cu *2p* core level.

cross-section generally decreases with increasing photon energy above the photoionization threshold [38], with one, in the case of free atoms, or several, in the case of solids, minima close to the photoionization threshold [39]. This makes ultraviolet photons ideal for studying the valence band, while higher energy photons are more suited for core level investigations. The minima present can also be exploited in tuning sensitivity to specific levels.

The effective free path also depends on energy. To be a bit more illustrative, let's take the case of an amorphous solid, where the effective free path can be very well approximated by inelastic mean free path. This means that, to the first order, we disregard photoelectrons that undergo inelastic collisions, because they no longer carry the information expressed by equation 2.16 in a straightforward manner. The inelastic mean free path increases with energy monotonically from a minimum at around 50–100 eV [40]. The increase on both sides of the minimum is related to the number of open channels for inelastic scattering at the given timescale. Variation in the energy of the primary photon source can thus be utilized to tune surface sensitivity, typically in the approximate range of 1 to 10 nm.

It should be noted that, in the case of crystalline solids, angular dependence of the above-mentioned parameters can't be ignored. Spatial orientation of atomic orbitals have to be taken into account in the photoionization cross-section [41] and elastic scattering on an ordered lattice has to be included in the effective free path [42]. Both effects can strongly modulate the intensity as defined by equation 2.15.

We will now discuss how to extract information contained in photoelectron spectra. An exemplary photoelectron spectrum is shown in Figure 2.2. There are

various spectral features that can be present in a photoelectron spectrum. First and foremost, the elastic photoelectrons and Auger electrons corresponding to the left and right term of equation 2.14, respectively. Second, satellites and ghost lines originating from imperfect monochromaticity of the excitation source and impurity generated photons. And, finally, features corresponding to characteristic losses, such as plasmons, intra-band transitions, and shake-up and shake-off excitations. All the features carry information, but we are generally interested in the elastic photoelectrons the most. Essentially, what we want to do is extract the area of features corresponding to these photoelectrons and make use of equation 2.11 or 2.15 in determining their state in the solid. These features can be generally described by a convolution of a Gaussian and Lorentzian function, which corresponds to a Voigt function:

$$\int_{-\infty}^{\infty} G(x';g)L(x-x';l)dx'. \tag{2.17}$$

The Gaussian function accounts for instrumental resolution and temperature dependent Doppler broadening, while the Lorentzian function accounts for lifetime broadening (the uncertainty relation for energy). Because it is impractical to use numerical convolution algorithms for the analysis, we instead turn to an analytical approximation of the Voigt function as defined in [43]:

$$V(X,Y) = \sum_{i=1}^{4} \frac{C_i(Y-A_i) + D_i(X-B_i)}{(Y-A_i)^2 + (X-B_i)^2}; X = \frac{\epsilon}{\sigma\sqrt{2}}; Y = \frac{\gamma_L}{\sigma 2\sqrt{2}}, \tag{2.18}$$

where $A_i \rightarrow D_i$ are a set of 16 constants, ϵ is the variable of the lineshape $I(\epsilon)$, σ is the standard deviation, and γ_L is the full width at half maximum (FWHM) of the Lorentzian function. FWHM of the Gaussian function in this definition is $\gamma_G = 2\sigma\sqrt{2ln2}$. The benefit of this analytical approximation is the ease with which the first and second derivative can be calculated. Combinations of functions $V(X,Y)$ and their derivatives with a curve fitting algorithm, such as Levenberg–Marquardt, allows us to precisely determine an area under a curve represented by the photoelectron spectrum. However, not all of the area belongs to the elastic photoelectrons. Specifically, we can notice an appreciable background in Figure 2.2. In accounting for the background we will highlight several bad practices that are sadly prevalent in the field of photoemission spectroscopy.

The background corresponds to non-characteristic energy-loss processes. We can mathematically decouple these processes into two parts. The first part is connected to the electric field of the core-hole created in the photoemission process and the second part is connected to the electric field of the photoelectron propagating towards the surface and into the vacuum region. These separated energy-loss processes are often called intrinsic and extrinsic, respectively. While the decoupling certainly is only an approximation, it allows us to describe the background in a simple manner. First, the intrinsic part accounts for the step-like character of the photoelectron background. The step-like character originates from the fact that the intrinsic background is proportional to the amount of elastic photoelectrons (i.e., it increases with every allowed photoionization process). The intrinsic background has been first described by Shirley and now bears his name

[44]. In a slightly more modern notation, we can write the intrinsic background function as follows:

$$I_{S,i}(E) = k \int_E^\infty (I_p(E') - I_{S,i-1}(E'))dE', \tag{2.19}$$

where k is the material constant, and $I_p(E')$ is the elastic photoelectron signal. The formula is iterative with the initial approximation $I_{S,0}$ being a constant function. There are several important aspects related to application of this formula that reveal problems with its implementation in broadly utilized software for analysis of photoelectron spectra. Typically, the Shirley background as defined by equation 2.19 is subtracted from measured spectra with the integral being approximated by sums over points of the spectra in the measured range. There are three major inconsistencies in this procedure. First, if the measured spectrum contains several contributions (i.e., different chemical states) k is arbitrarily averaged over the values that correspond to the individual contributions. Second, the summation introduces arbitrary lower and upper limit (i.e. the measured range of the spectrum), which is subjectively chosen by the experimentalist. Third, arguably the most important problem is the fact, that the measured spectrum does not directly correspond to the elastic photoelectron signal at a given energy. It is obvious that the measured spectrum contains inelastically scattered photoelectrons by definition.

All the above-mentioned problems can be easily resolved by including the Shirley background in the fitting process. Specifically, one has to calculate the intrinsic background not from the measured spectra, but directly from the functions describing the elastic photoelectrons. This allows one to both introduce specific k for a given spectral feature and get rid of the arbitrary lower and upper limits by integrating analytical functions, such as $V(X, Y)$, from $-\infty$ to ∞.

Now, the Shirley background is often the only background used during analysis of photoelectron spectra. However, as was described above, it covers only the intrinsic part of the background. The extrinsic part is by definition related to path integrals of the escaping photoelectrons. This makes it a bit more complicated, but it also means that it actually caries information about depth distribution in the solid. The theoretical description of the extrinsic background has been developed by Tougaard [45], but its application is limited by the need for experimental data measured over wide regions, which imposes impractical time requirements on the measurements. However, the Tougaard formula can be analytically approximated in the region near the spectral features of interest by the so called slope background [46]:

$$I_T(E) = k_{slope} \int_E^\infty I_p(E')(E_A - E)dE_A, \tag{2.20}$$

where k_{slope} is the scattering factor, and $(E_A - E)$ is the energy loss (where E_A is the kinetic energy of the elastic photoelectrons). The analytic formula allows to use the same approach as with the Shirley background, calculating the slope background directly from functions describing the elastic photoelectrons.

Despite the simplicity of this approach to both the Shirley and Tougaard backgrounds it is not implemented in any available analytical software. For the purpose of this thesis, the method has been implemented in Fityk 1.3.1 [47],

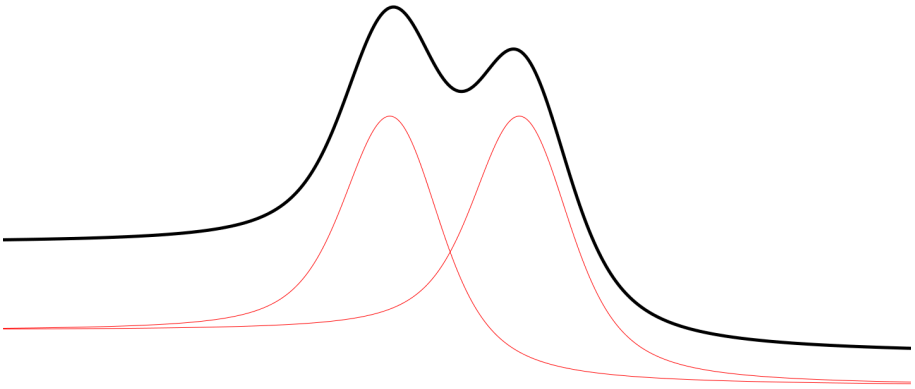

Figure 2.3: Implementation of Voigt functions that includes both intrinsic and extrinsic photoelectron background. The explicit accounting for the background in the fitting process removes arbitrary bounds for background subtraction.

which also allows to utilize advanced curve fitting algorithms, such as genetic algorithms and Nelder–Mead algorithm. The relevant part of the code is included as an attachment to the thesis (see Attachment 1.). An example of the fitting functions is shown in Figure 2.3.

Finally, while the description provided in this section encompasses the theory and methodology relevant to the utilization of photoemission in this thesis, it is by no means exhaustive. Other advanced methods based on photoemission are illustrated in Figure 2.4.

2.2 Low-Energy Electron Diffraction

Low-energy electron diffraction (LEED) is a surface analysis technique that provides information about the symmetry, morphology and, indirectly, electronic structure of a crystalline solid. The LEED experiment consists of electrons of defined energy impinging on a surface of a solid, where they are scattered, and the interference pattern of elastically scattered electrons (the inelastically scattered electrons form a background) is measured. The interference pattern can be described as a sum of the scattered electron wavefunctions:

$$\Psi(\vec{K},\vec{k_i}) = \sum_{\vec{n}} f(\vec{n},\vec{K},\vec{k_i}) e^{i\vec{K}\vec{r}(\vec{n})}, \tag{2.21}$$

where $\vec{K} = \vec{k_i} - \vec{k_f}$ is the scattering vector, $\vec{k_i}$ is the wave vector of the primary electron, $\vec{k_f}$ is the wave vector of the scattered electron, $f(\vec{n},\vec{K},\vec{k_i})$ is the structure factor, and $\vec{r}(\vec{n})$ is the position of the scatterers that the sum is carried over. The diffraction intensity can than be defined as:

$$I(\vec{K},\vec{k_i}) = |\Psi(\vec{K},\vec{k_i})|^2 = \sum_{\vec{n},\vec{m}} f(\vec{n},\vec{K},\vec{k_i}) f^*(\vec{m},\vec{K},\vec{k_i}) e^{i\vec{K}(\vec{r}(\vec{n})-\vec{r}(\vec{m}))}. \tag{2.22}$$

The exponential function in equation 2.22 reflects the von Laue condition for constructive interference with $\vec{r}(\vec{n}) - \vec{r}(\vec{m}) = \vec{G}$ being a vector of the reciprocal lattice. This essentially means that the exponential function defines position of

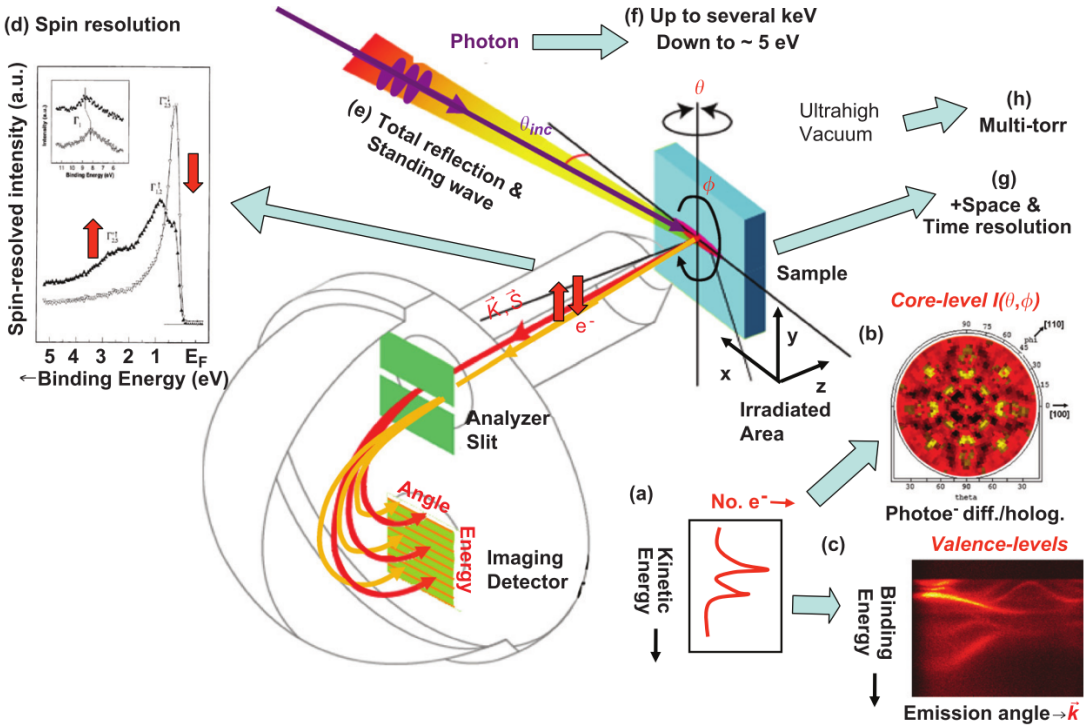

Figure 2.4: Scheme of a typical photoemission experiment [48]. Various types of measurements include: (a) energy spectrum of photoelectrons — chemical information, (b) photoelectron diffraction — atomic structure, (c) photoelectron momentum — electronic band structure, (d) spin resolution — magnetic properties, (e) standing wave excitation — z resolution, (f) hard X-rays — bulk information, (g) time or lateral resolution — dynamic processes and microscopy, and (h) high pressure measurements — *in situ* chemical reactions.

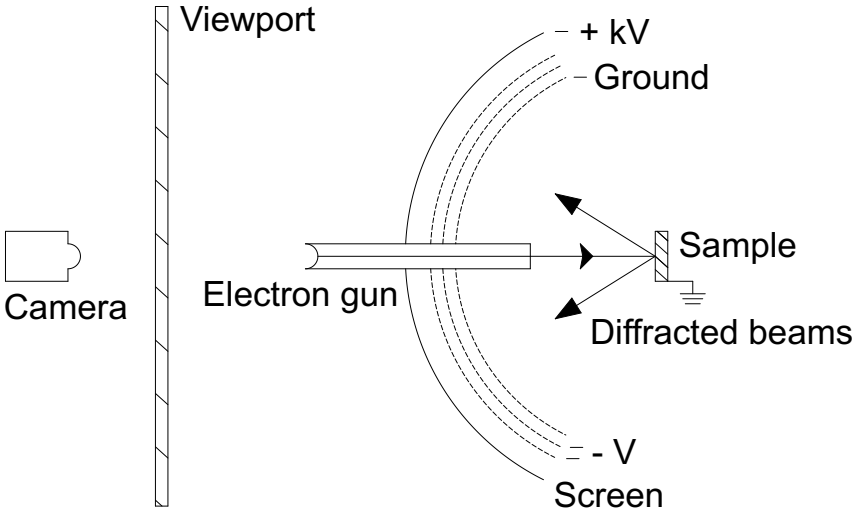

Figure 2.5: Scheme of a rear-view LEED experiment.

LEED spots, reproducing symmetry of the lattice of scatterers. Importantly, because of the low energy of the primary electrons utilized in LEED ($\sim$ 100 eV), the electrons are scattered elastically only within a few atomic layers from the surface. The periodicity of the lattice of scatterers is therefore well defined only in direction parallel to the surface, which relaxes selection rules for $\vec{K_{\perp}}$. Consequently, the information provided by the position of LEED spots is two-dimensional. The third dimension is contained in the intensity of the spots defined by the structure factor, where the penetration depth and multiple scattering play a significant role.

The position of LEED spots is the most common source of information in LEED, reflecting the symmetry of the surface. In this thesis the information is accessed by fitting LEED spots measured through a rear-view LEED configuration (see Figure 2.5) to two-dimensional Gaussian functions, while correcting for geometric aberrations of the measuring setup through calibration on a known sample, a Cu(111) single crystal. The symmetry is then transferred to real space by performing Fourier transformation, essentially shifting from the wave vector to wavelength representation.

However, while intensity analysis is not utilized in the thesis, its connection with the next section entails a brief description of how to approach the structure factor. First, a scattering of an electron by a single atom is calculated, solving the Schrödinger equation with an atomic potential. Here, a spherical approximation to the atomic potential is often employed. This is valid for electrons in the typical energy range of LEED ($\sim$ 100 eV) that are predominantly scattered by the spherical inner electron shells and the atomic nucleus. However, if the energy of the primary electrons is only several electron volts, the symmetry of the valence orbitals have to be accounted for. The single scattering process is where the electronic structure of the solid affects the LEED spot intensity.

Now, the multiple scattering has to be included in the calculation. This is

done in two steps. First, multiple scattering within an atomic layer is calculated by arranging the atomic potentials in a two-dimensional plane. Again, spherical approximation for the potentials is often used, with a constant value in the space between space-filling spheres at the atomic positions, the so called muffin-tin approximation. The constant value corresponds to the inner potential V_0, an energy that is added to the electron when it enters the solid. Second, multiple scattering between the atomic layers is calculated by stacking these up to arrive at the full surface diffraction. Finally, the inelastic scattering processes, which are dominated by plasmon excitation at the typical LEED energies, are accounted for by an imaginary part of the inner potential. The imaginary part of the inner potential leads to an imaginary part of the wave vector and consequently attenuates the waves propagating in the solid. It should be noted that this approach is closely connected with the photoemission process described in the previous section. Specifically, the photoemission final state function can be thought of as an inverse LEED wave function in the following sense. If we reverse the direction of the incoming monochromatic beam of electrons that is scattered from atomic sites of the solid in LEED we obtain a monochromatic wave of electrons originating at the atomic sites of the solid. Such a wave is analogous to the photoemission final state propagating through the solid, which is often utilized in connecting the two theoretical frameworks.

2.3 Low-Energy Electron Microscopy

Low-energy electron microscopy (LEEM) is a method that directly builds on the principles underlying LEED, extending these into lateral resolution. While LEED principally averages over the whole area illuminated by primary electrons, LEEM is able to resolve origin of the elastically scattered electrons within a few nanometers. In order to achieve this a complex optics are required, making LEEM instruments difficult to manufacture. Because electron optics are much easier to construct for high energy electrons, the electrons are accelerated to several kiloelectronvolts when they pass through the optics. The system is schematically depicted in Figure 2.6. A coherent beam of low-energy monochromatic electrons generated by a field emission electron gun is accelerated towards illumination optics and passes through a beam splitter. The beam is then slowed down to desired energy (typically several electronvolts) with respect to the sample potential. The reflected beam is deflected toward the imaging optics by the same beam splitter and finally arrives at a multi-channel detector.

The complex optics allow for a variety of measuring modes. The most common is bright field imaging, where reflectivity of a surface is measured for a specific energy of primary electrons by passing only the (00) specular reflection through the imaging column. This is effected by the use of an aperture. The bright field imaging provides contrast through the structure factor discussed in the previous section. Because the contrast emerges from backscattered electrons of a coherent beam the apparatus essentially acts as an electron interferometer in the direction of the electron beam, offering orders of magnitude better height resolution compared to the lateral one. Reflections other than the (00) can be singled out in the imaging column, leading to a straightforward structural contrast in the so called dark field imaging mode. Similarly, an aperture can be placed in the

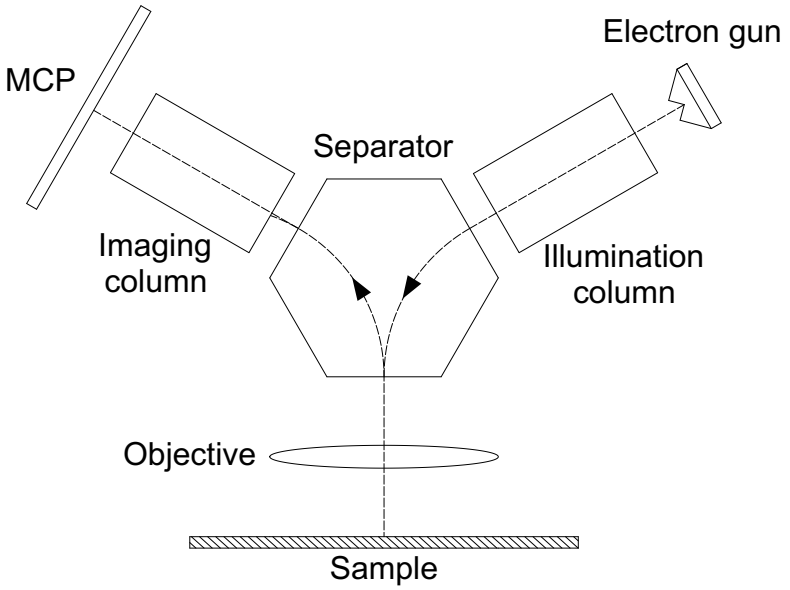

Figure 2.6: Scheme of a typical LEEM experiment.

illumination column, shrinking the illuminated area of the surface and allowing for LEED measurements from areas down to a few hundred nanometers.

The most interesting information is contained in the dependence of reflectivity on the primary electron energy. While the elastic electrons carry the most easily accessible structural and morphological information, inelastic scattering provides access to electronic structure and chemical contrast by means of intensity–voltage (I–V) curves at the same length-scale. The position of maxima on the I–V curves reflects structural ordering of the material, but the intensity of the maxima is related to energy dependent reflectivity of the solid manifested through unoccupied band structure [49]. Coupling I–V LEEM with theoretical calculations that can access what is essentially the photoemission final state, such as Bloch-waves-based calculations of Korringa-Kohn-Rostoker (KKR) formalism, offers a unique opportunity to gauge electronic structure of materials at nanoscale.

Finally, an invaluable benefit of the LEEM is the inherent time resolution of all of its imaging regimes, which enables investigation of dynamical surface processes. The open configuration (see Figure 2.6) also leaves the sample accessible to various experimental techniques. This allows, for example, *in situ* observation of growth processes and chemical reactions. One of the most important modifications enabled by the open configuration is photoemission electron microscopy (PEEM).

PEEM is a modification of LEEM that uses photons as the primary source, exploiting photoemission process for easily accessible chemical contrast while sacrificing lateral resolution (typically an order of magnitude) [50]. The access to the powerful methodology of the field of photoelectron spectroscopy at nanoscale makes PEEM the ideal tool for investigation of electronic structure, magnetic ordering, electron localization, bonding character and chemical interaction of complex materials. Particularly synchrotron-based light sources providing tunable polarized photons enable the use of advanced photoemission techniques [50],

such as resonant photoelectron spectroscopy (RPES), XAS and X-ray magnetic circular dichroism (XMCD), while retaining the benefits of the high lateral and time resolution.

2.4 Experimental apparatuses

The studies reported in the thesis were conducted with UHV apparatuses (base pressure better than $10^{-}8$ Pa). The following is the list of the apparatuses along with references to detailed description (further relevant information is reported together with the results in the next section):

Charles University, Czech Republic
Custom — XPS/UPS–XPD/ARUPS [51]
Custom — XPS/STM/TPD/LEED [52]

Elettra, Italy
Custom — SRPES/NEXAFS [53, 54]

Hiroshima Synchrotron Radiation Center, Japan
Custom — ARPES BL-1 [55, 56]

University of Bremen, Germany
Commercial — Elmitec LEEM-III [57]

BESSY II, Germany
Commercial — FE-LEEM P90 [58, 59]

3. Results and discussion

The results of the thesis are presented in the form of five manuscripts that represent the culmination of the work carried out during my doctoral studies. The manuscripts are briefly introduced with a focus on their contribution to the overarching goal of the thesis and their relevance to other scientific works.

3.1 Oxygen vacancy co-ordination in model systems of cerium oxide

Chemistry of reducible oxides is governed by their oxidation / reduction potential. This makes control over the stoichiometry of reducible oxides the key to unraveling the role they play in chemical reactions. A large body of scientific work has been devoted to exploring various experimental approaches that can facilitate a precise control of oxygen content in reducible oxides. These include chemical pathways utilizing reducing and oxidizing agents, thermal treatment, exposure to ionizing radiation, etc. [34, 60]. However, the stoichiometry alone does not completely determine the change in properties introduced by oxygen vacancies in reducible oxides. Specifically, the co-ordination of oxygen vacancies — e.g., clustering or long-range ordering — significantly affects the reducible oxide, both structurally and electronically. In the case of cerium oxide most of the attention is drawn towards localization of f electrons on cerium atoms as a consequence of oxygen vacancy formation, which changes their formal oxidation state from Ce^{4+} to Ce^{3+}. The position of oxygen vacancies in relation to each other is closely connected to the position of cerium atoms on which the f electron localize. The complex set of parameters imposes rules on oxygen vacancy ordering in cerium oxide, both in the bulk [17] and on the surface [18]. However, most of the methods utilized for the control of stoichiometry do not allow to properly explore this phase space.

Herein, a Ce–ceria interfacial interaction is employed for the purpose [61]. First, a stoichiometric $CeO_2(111)$ buffer is prepared utilizing standard procedures. Second, a metallic cerium overlayer is deposited onto the buffer. The system is then annealed to allow diffusion of oxygen to the overlayer, which results in formation of a gradient of oxygen vacancies towards the surface. Importantly, the metal overlayer adapts the structure of the buffer during its oxidation. The process is shown in Figure 3.1 from the point of view of STM. The amount of oxygen vacancies can be precisely controlled by adjusting the thickness of the metal overlayer, allowing exploration of the whole range of stoichiometries between $CeO_2(111)$ and $Ce_2O_3(111)$. The precision of the utilized approach enabled observation of several structures of ordered oxygen vacancies. Starting from $CeO_2(111)$-(1×1), a $Ce_7O_{12}(111)$-$(\sqrt{7} \times \sqrt{7})$R19.1°, $Ce_3O_5(111)$-(3×3), and $Ce_2O_3(111)$-(4×4).

An important finding is that cerium oxide layers reduced by the interfacial reaction with metallic cerium represent a realization of the ideal scenario of reduction and reoxidation of cerium oxide by removing / adding oxygen from / to the fluorite CeO_2 lattice without modifying the structure of the cerium sublattice. This is effectuated by a vastly different mobility of anions and cations in the lattice. While oxygen mobility is activated already at 300 °C, cerium atoms

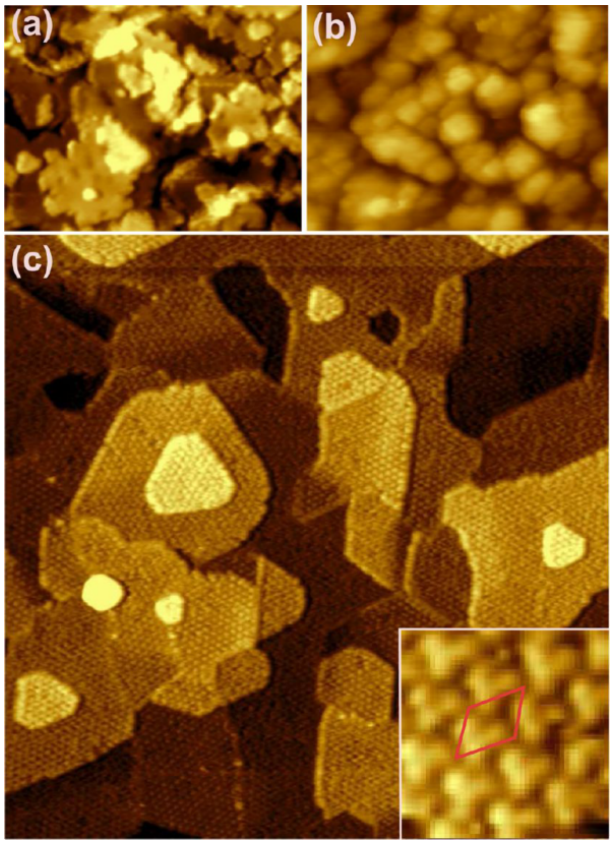

Figure 3.1: Scanning tunneling miroscopy images of the reaction between Ce and CeO_2 buffer layer: (a) ordered CeO_2 buffer, (b) disordered surface upon Ce deposition, (c) ordered layer upon annealing in vacuum at 900 K. Inset: high-resolution image and surface unit cell (red rhombus) of the reacted layer. Images a–c are to scale. Image width (a,b) 60 nm, (c) 120 nm, (inset) 6×6 nm^2. [61]

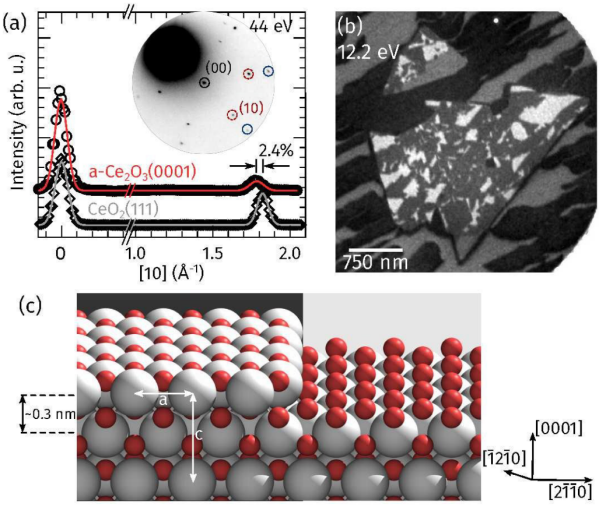

Figure 3.2: (a) μLEED pattern exhibited by the large cerium oxide particle depicted in (b) and line profile along the (10) direction. (b) LEEM image of two cerium oxide particles after reduction. (c) Model of the bulk terminated a-Ce_2O_3(0001) surface including a step about $c/2$ high, leading to two different oxygen-terminated surfaces. [63]

are immobile even at 600 °C [62]. It is noteworthy that the observed ordering of oxygen vacancies in the transition from CeO_2(111) to Ce_2O_3(111) does not necessarily represent the thermodynamic equilibrium. Indeed, experiments that reduce the surface by annealing above 700 °C do not observe conservation of the fluorite lattice up to Ce_2O_3 and instead report transformation to the hexagonal form of cerium oxide (see Figure 3.2) [63, 64]. Nevertheless, the low temperature transition is more relevant to chemical reactions where cerium oxide is utilized. Oxygen exchange decoupled from cation mobility can thus be exploited in advanced model catalytic studies of reducible oxides, where not only stoichiometry but also spatial ordering of oxygen vacancies can be determined.

Ordered phases of reduced ceria as epitaxial films on Cu(111)

Tomáš Duchoň, Filip Dvořák, Marie Aulická, Vitalii Stetsovych, Mykhailo Vorokhta, Daniel Mazur, Kateřina Veltruská, Tomáš Skála, Josef Mysliveček, Iva Matolínová, and Vladimír Matolín

Faculty of Mathematics and Physics, Department of Surface and Plasma Science, Charles University, V Holešovičkách 2, 18000 Prague 8, Czech Republic

We demonstrate the ability to precisely and reproducibly control the stoichiometry of ceria thin films on Cu(111) using the technique of reducing ceria layers in reaction with metallic Ce complemented by oxidation through O_2 exposition. With the whole range of stoichiometries from CeO_2 to Ce_2O_3 being experimentally accessible, we show that the transition between the limiting cases is realized by equilibration of mobile oxygen vacancies near the surface of the film, with the fluorite lattice of cerium atoms remaining without change during the process. We identify two stable surface reconstructions representing distinct oxygen vacancy ordering during the transition. A $(\sqrt{7} \times \sqrt{7})R19.1°$ reconstruction representing a bulk termination of the ι-Ce_7O_{12} and a (3×3) reconstruction of the surface without a direct relation to known bulk phases of reduced ceria. The interface reaction between Ce and ceria presents an unprecedented tool for oxygen vacancy engineering in ceria, allowing to investigate the influence of oxygen vacancy concentration and coordination on catalytic properties of ceria based model catalysts with great precision.

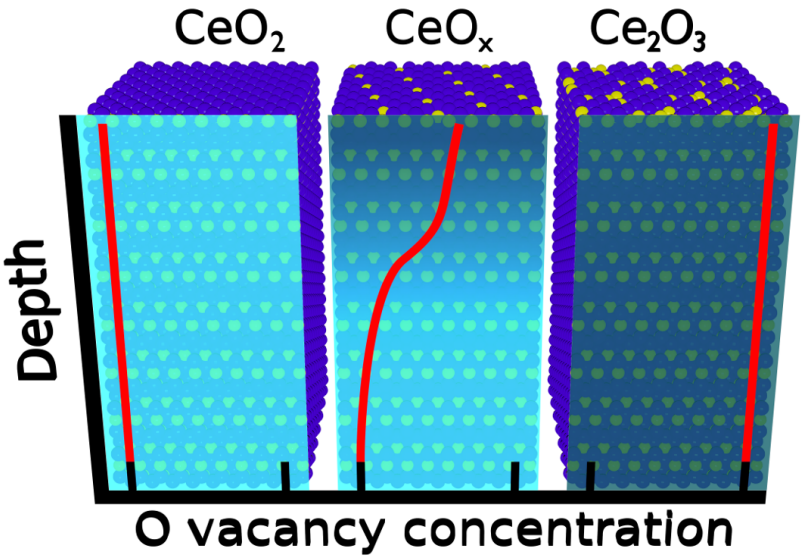

■ Introduction

Reducible oxides play an important role in heterogeneous catalysis [7, 65–70]. Due to their ability to store or release oxygen reducible oxides usually act as an oxygen supply or a reducing agent during catalytic reactions [16, 71]. Reactions over reducible oxides are typically accompanied by changes in the oxide stoichiometry that are often realized on complex phase diagrams [72–79] and may influence the catalytic activity through changes in local coordination, surface termination and long range ordering in the oxide [80–83]. Model studies isolating the changes of the oxide stoichiometry are of utmost importance for understanding the role of stoichiometry in the reaction mechanisms over reducible oxides and for improving and developing new catalysts.

Reactivity of cerium oxide (ceria)-based catalysts is greatly influenced by the presence of oxygen vacancies in ceria [15, 84]. The ability to adjust the concentration and the distribution of oxygen vacancies allows for the control over the reactivity and the selectivity of ceria-based catalysts [60, 85]. For this reason, having experimental access to ordered phases of cerium oxide with different concentration and coordination of oxygen vacancies greatly enhances the possibilities of model catalytic studies. Several phases of ordered reduced ceria have been prepared in the past in the form of powder or single crystal samples [17, 86, 87], but only recently ordered reduced phases of ceria have been realized in the form of thin films on single crystalline supports. Thin film of ι-Ce_7O_{12} phase on hex-$Pr_2O_3(0001)/Si(111)$ substrate was obtained by Wilkens et al. via heating of CeO_2 layer in vacuum [88]. Thin film of c-Ce_2O_3 phase on Cu(111) was obtained by our group via an alternative method of reducing the CeO_2 layer in an interface reaction with metallic Ce [61]. Thin film of c-Ce_2O_3 phase has been reported also in the latest study on hex-$Pr_2O_3(0001)/Si(111)$ [89].

Here we present a detailed investigation of the properties of the ceria layers on Cu(111) reduced by the interface reaction with Ce. Using a stepwise titration of ceria layers with Ce in the interface reaction we continuously change the stoichiometry of the ceria layers on Cu(111) from CeO_2 [34] to Ce_2O_3 [61]. We characterize the concentration and the depth profile of the oxygen vacancies in the reduced ceria layers by X-ray photoelectron spectroscopy (XPS) and resonance photoelectron spectroscopy, the surface reconstruction of the layers by low energy electron diffraction, the morphology of the layers by scanning tunneling microscopy and the surface composition of the layers by ion scattering spectroscopy (ISS). We are identifying two surface reconstructions of ordered reduced ceria on Cu(111) — the $(\sqrt{7} \times \sqrt{7})R19.1°$ reconstruction corresponding to bulk ι-Ce_7O_{12} [88] and the (3×3) reconstruction corresponding to bulk $CeO_{1.67}$. We show that the process of reduction of ceria via the interface reaction with metallic Ce is fully reversible upon oxidation by O_2. This allows us to interpret the properties of the reduced ceria films in our experiment in terms of creation, annihilation and equilibration of oxygen vacancies in the fluorite lattice of cubic ceria. Reduction of ceria thin films by metallic Ce complemented by oxidation by O_2 allow a precise experimental control over both the concentration and the coordination of oxygen vacancies in thin ceria films. The coordination of oxygen vacancies represents a new degree of freedom that can be controlled and exploited for example in advanced model catalytic studies over ceria.

■ Methods

Experiments were carried out in three ultra-high vacuum systems with a base pressure of 1×10^{-8} Pa. All systems are equipped with the necessary sample cleaning and in situ preparation facilities, low electron energy diffraction optics, laboratory X-ray sources and X-ray photoelectron spectroscopy analyzers. One of the apparatuses is located at the Materials Science Beamline in Trieste representing a tunable X-ray source for resonance photoelectron spectroscopy. Another apparatus is equipped with scanning tunneling microscopy, and the third one with ion scattering spectroscopy. Prior to the sample preparation, the Cu(111) single crystal substrate (MaTecK) was cleaned by several cycles of Ar^+ sputtering and annealing in vacuum and the Ce evaporator was thoroughly degassed. As a starting point for the experiments layers of CeO_2(111) on Cu(111) with a typical thickness of 3 nm were prepared by evaporating Ce (Goodfellow, 99.9%) from a tantalum or molybdenum crucible heated by electron bombardment in a background atmosphere of 5×10^{-5} Pa of O_2 (Linde, 5.0) and at substrate temperature of 250 °C [34]. Reduction of the prepared CeO_2(111) buffers was achieved through deposition of metallic cerium without oxygen background and subsequent annealing at 600 °C for 30 min in vacuum. Oxidation of the layers was performed by exposure to controlled doses of O_2 at room temperature and subsequent annealing at 600 °C for 30 min in vacuum. The reduction and oxidation steps were eventually repeated or alternated to obtain the desired ordering and stoichiometry of the layers. Typically, the reduction step involves a deposition of 0.5 nm of Ce, the oxidation step a dose of O_2 as small as 1 L.

The thickness of the prepared ceria films was determined from the attenuation of Cu $2p_{3/2}$ signal of the substrate measured by XPS. The attenuation length for CeO_2 and Ce_2O_3 was calculated using the TPP-2M formula [40]. The reference for ceria coverage in this contribution is 1 monolayer (ML), a stack of O–Ce–O layers corresponding to the vertical stacking of O and Ce in (111) direction in fluorite-like phases of ceria. 1 ML is 3.1 Å thick and contains 7.9×10^{14} cm^{-2} Ce atoms. Identification of the particular ordered reduced phases of ceria in different apparatuses was achieved based on the combination of the characteristic LEED diffraction patterns and XPS spectra of Ce 3d and O 1s. XPS spectra of Ce 3d, Cu $2p_{3/2}$ and O 1s core levels were recorded using the excitation energy of $h\nu$=1486.6 eV (Al K_α). The characteristic properties of the reduced ceria layers presented in this article were repeatedly observed in about 30 experiments.

The main information obtained from the photoelectron spectroscopy measurements is the degree of reduction of the ceria layers. Creation of one oxygen vacancy in CeO_x is accompanied by localization of two excess electrons on two lattice Ce ions changing their charge state from Ce^{4+} to Ce^{3+} [16]. We determine the concentration of Ce^{3+} and Ce^{4+} in XPS from the areas Ce^{3+}_{area} and Ce^{4+}_{area} of Ce^{3+} and Ce^{4+} features in the Ce 3d spectra, respectively, identified and fitted according to Skala et al. [90] [90] The accuracy of this method in the determination of the Ce^{3+} and Ce^{4+} concentrations is ±2%, and the method is able to detect changes of the Ce^{3+} and Ce^{4+} concentrations between two samples as small as ±0.5% [91]. We describe the degree of reduction by a ratio $Ce^{3+}_{area}/(Ce^{3+}_{area} + Ce^{4+}_{area})$, or by x in the notation CeO_x. The degree of reduction

obtained from XPS represents a weighted average over the information depth of XPS measurements. For XPS of Ce 3d, Al K_α and the detection of photoelectrons along the sample normal the information depth is about 3 nm or 10 ML. To obtain more surface sensitive information we additionally perform XPS measurements 70° off the sample normal decreasing the information depth, theoretically, by $\cos 70°$, i.e. a factor of three [92].

For the highest surface sensitivity we performed RPES measurements of the valence band of the ceria samples using the synchrotron radiation [93]. For determining the degree of reduction from RPES we use the resonance enhancement $D(Ce^{4+})$ and $D(Ce^{3+})$ of Ce^{4+} and Ce^{3+} features in the RPES spectra (Ref. 93, cf. Fig. 4) assuming a direct proportionality of $D(Ce^{4+})$ and $D(Ce^{3+})$ to the concentration of Ce^{4+} and Ce^{3+} ions [12]. The used photon energies were 115 eV for off resonance, 124.8 eV for Ce^{4+} resonance, and 121.4 eV for Ce^{3+} resonance measurements.

The surface composition of the samples was determined with ISS [61]. He^+ ions with the energy of 2 keV and the impact angle of 45° were used for the measurements. The LEED, XPS, RPES, and ISS measurements were carried out at room temperature upon a flash heating of the sample to 500 °C to minimize the effects of eventual unintended adsorption, namely OH groups. Heating of the samples was not available for STM measurements. STM images were obtained at room temperature by tunneling of electrons into empty states of the sample using chemically etched and vacuum-annealed tungsten tips.

■ Results

Our experiments demonstrate that controlling the amount of Ce deposit in the interfacial reaction of metallic Ce with a ceria film allows preparation of reduced CeO_x films in the range of $1.5 \leq x \leq 2$. The change of the stoichiometry determined from XPS measurements is continuous, however, we are able to identify four characteristic surface reconstructions in our layers. The electron diffractograms of these reconstructions are shown in Fig. 3.2. Starting from the (1×1) reconstruction of the $CeO_2(111)$ surface (Fig. 3.2(a), Ref. 34) the increasing degree of reduction of the ceria layer is accompanied by the change of the LEED pattern to $(\sqrt{7} \times \sqrt{7})R19.1°$ (Fig. 3.2(b)), (3×3) (Fig. 3.2(c)) and finally to (4×4) reconstruction of c-$Ce_2O_3(111)$ (Fig. 3.2(d), Ref. 61). The samples showing a single set of LEED spots as in Fig. 3.2 are carefully prepared to certain narrow ranges of the CeO_x stoichiometry. We consider the properties of such samples as characteristic of the evolution of the reduction of CeO_x thin films on Cu by Ce and only refer to the samples showing the single set of LEED spots in this work (Figs. 3.2-3.7, Table 3.3). For stoichiometries outside the narrow characteristic ranges the samples show typically a combination of two sets of LEED spots from Fig. 3.2 indicating a coexistence of the reconstructions on the surface.

The stoichiometry of the films prepared by interfacial reaction has been followed by XPS, with the degree of reduction of the samples characterized through fitting of the measured Ce 3d spectra [90]. The Ce 3d and O 1s spectra measured on the samples exhibiting LEED patterns as in Fig. 3.2 are shown in Fig. 3.4, lower part ('Ce deposition'). The ratios $Ce^{3+}/(Ce^{3+} + Ce^{4+})$ determined from

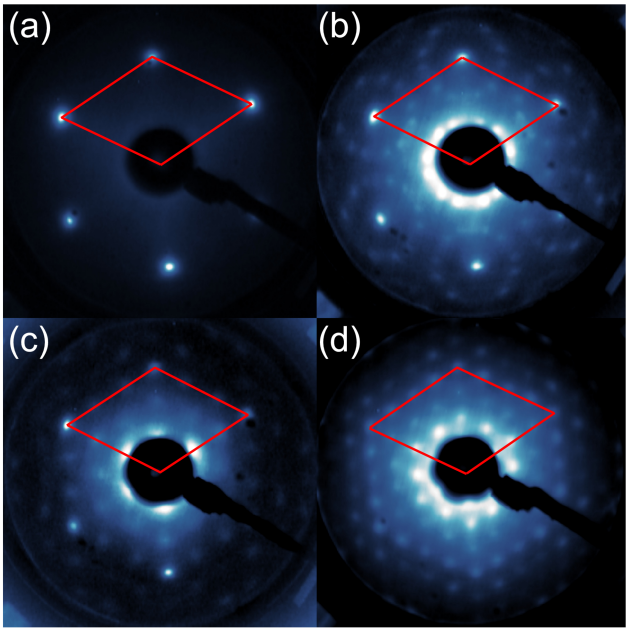

Figure 3.3: LEED images of ordered phases of reduced ceria on Cu(111) obtained by interface reaction of the CeO_2(111) buffer layer with Ce deposit. Degree of reduction increases from (a) to (d). (a) (1×1) spots of CeO_2(111) buffer layer, (b) $(\sqrt{7} \times \sqrt{7})$R19.1° reconstruction, (c) (3×3) reconstruction, (d) (4×4) reconstruction of c-Ce_2O_3. Electron energy 58 eV. The (1×1) unit cell of CeO_2(111) is outlined red.

the curves in Fig. 3.4 are plotted in Fig. 3.5. The starting CeO_2 buffer exhibits only features of Ce^{4+}. The increase of the amount of metallic Ce in the interfacial reaction between Ce and CeO_2 leads to the increase in contribution of the Ce^{3+} features to the spectra [90]. By increasing the amount of metallic Ce the stoichiometry of the layers after reaction can be tuned from pure CeO_2 to pure Ce_2O_3. Apart from the changes in Ce 3d spectra this transition is accompanied by a shift of the O 1s line to higher binding energies [61, 94] as shown in Fig. 3.4.

Important insight into the oxidation-reduction properties of ordered layers of reduced ceria can be obtained by oxidation of the samples by O_2 after reaching the limiting stoichiometry of Ce_2O_3, LEED pattern (4×4). Oxidation by O_2 allows changing the stoichiometry of the reduced ceria layers from Ce_2O_3 back to CeO_2 with all the characteristic surface reconstructions of ordered reduced ceria identified by LEED (Fig. 3.2) observed during oxidation as well. The Ce 3d and O 1s spectra measured on the samples upon oxidation of the Ce_2O_3 layers are shown in Fig. 3.4, upper part ('O_2 exposure').

The XPS spectra for all samples were measured at two angles of photoelectron emission: 0° and 70° off sample normal (cf. Fig. 3.4). The difference between the two signals can be used as an indication of enhancement of concentration of the measured features near the surface of the layer. The results for all surface reconstructions are summarized in Fig. 3.5, where the difference between the degree of sample reduction measured for 0° emission and 70° emission is marked gray. While the samples with the limiting stoichiometry CeO_2 (1×1) and Ce_2O_3 (4×4) show small or no difference in the degree of reduction [61], the layers with intermediate stoichiometry $(\sqrt{7} \times \sqrt{7})$R19.1° and (3×3) show an enhancement of

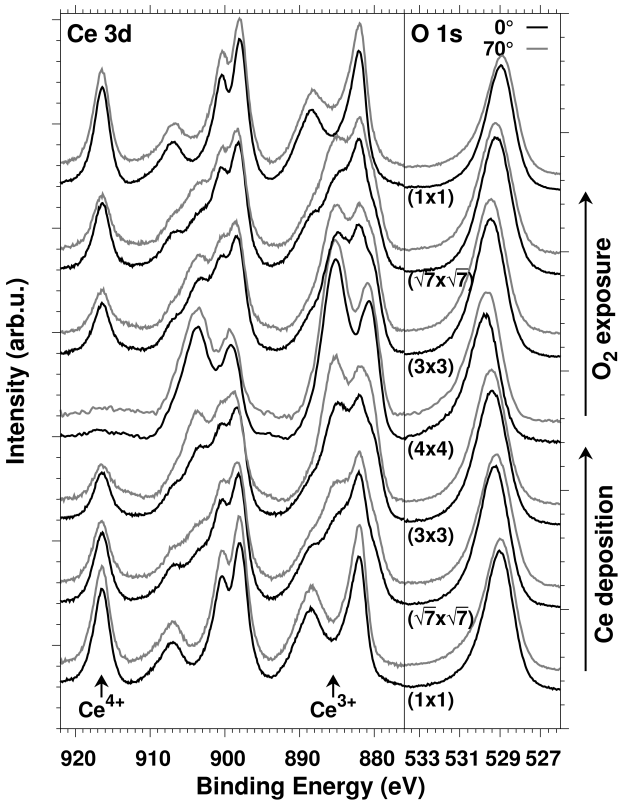

Figure 3.4: XPS spectra belonging to the ordered phases of reduced ceria on Cu(111). Left panel: Ce 3d, right panel: O 1s. Samples measured at 0° (black curves) and 70° off-normal emission (gray curves). With each sample the corresponding LEED pattern is indicated. (1×1) is the starting CeO_2 layer. Bottom $(\sqrt{7} \times \sqrt{7})$R19.1°, (3×3), and (4×4) samples obtained by reduction of $CeO_2(111)$ layers via interface reaction with Ce. Top (3×3), $(\sqrt{7} \times \sqrt{7})$R19.1°, and (1×1) samples obtained by oxidation of the (4×4)c-$Ce_2O_3(111)$ layers with O_2. The areas of the presented spectra have been normalized to 1 after subtraction of Shirley background and the curves have been offset for clarity. For better orientation, the positions of visually the most prominent peaks in $Ce^{4+}$and Ce^{3+}spectra are marked by arrows.

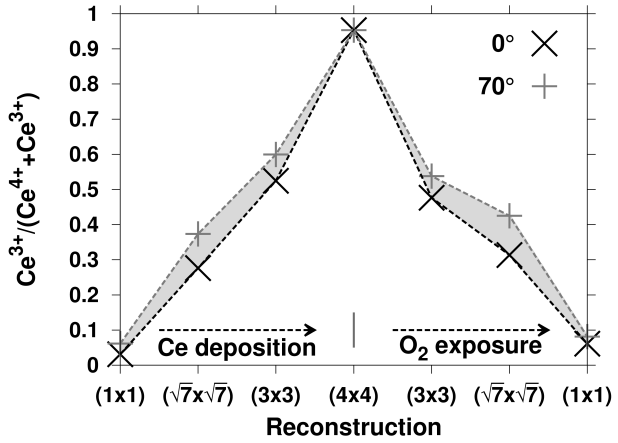

Figure 3.5: Degree of reduction of the ordered phases of reduced ceria on Cu(111) obtained by fitting of the XPS spectra from Fig. 3.4. Vertical axis: degree of reduction, horizontal axis: surface structure. Surface structures obtained by reduction of CeO_2(111) layers via interface reaction with Ce (left), or by oxidation of c-Ce_2O_3(111) layers with O_2 (right). The difference between the degree of reduction measured with normal emission (black crosses) and with 70° off-normal emission (gray crosses) indicating the accumulation of oxygen vacancies near the surface of $(\sqrt{7} \times \sqrt{7})$R19.1° and (3×3) surface structures is enhanced by light gray. The dashed lines are guides to the eyes.

the Ce^{3+} signal, and, consequently, oxygen vacancy concentration near the surface of the layer. This gradient of the vacancy concentration with depth below the surface is observed in all samples with intermediate stoichiometry. The oxygen vacancies accumulate near the surface of the layers regardless of the particular preparation method, both after reduction with Ce and after oxidation with O_2.

While the LEED images define the observed surface reconstructions without ambiguity, the degree of reduction observed in the XPS spectra for ceria layers with intermediate stoichiometry strongly depends on the thickness of the ceria layers. The reason for the dependence of the XPS spectra on the thickness of the layer is the averaging over different but finite thickness of the layer in the presence of the gradient of the vacancy concentration together with eventual modifications of the Ce^{3+} concentration near the interface with the metal substrate [95]. For comparability of the XPS spectra, the samples presented in Fig. 3.4 have been selected to have a thickness of about 4 nm after preparation. Ceria layers work as a supply or a sink of oxygen during reduction by Ce or oxidation by O_2, respectively, so the amount of Ce and the doses of O_2 needed to reach the desired stoichiometry of the layer depend sensitively on the thickness of the layers, too. Particularly, the samples in Fig. 3.4 were prepared with reaction parameters summarized in Table 3.3. For the layers prepared by interface reaction between CeO_2 buffer and Ce, thickness of the starting CeO_2 buffer and the thickness of the resulting layer after reaction are listed. For the layers prepared by oxidation of Ce_2O_3 layers, the thickness of the starting Ce_2O_3 layer and the exposure of O_2 are listed. Given the small difference between the XPS attenuation lengths for CeO_2 and Ce_2O_3 [40] the amount of Ce in the interfacial reaction calculates straightforwardly from the difference between the initial and the final thickness

reconstruction	reduction by Ce		oxidation by O_2	
	thickness of the CeO_2 buffer	thickness of the reacted layer	thickness of the Ce_2O_3 layer	O_2 dose
(1×1)	3.0 nm	-	4.2 nm	10 000 L
$(\sqrt{7} \times \sqrt{7})$R19.1°	3.5 nm	4.0 nm	4.5 nm	20 L
(3×3)	3.0 nm	3.7 nm	4.4 nm	1 L
(4×4)	3.0 nm	4.2 nm	-	-

Table 3.1: Parameters of the preparation of the samples from Figs. 3.4 and 3.5.

of the layer, and, upon oxidation, the thickness of the layers does not significantly change. For thicknesses of the layers other than ≈4 nm, the amount of Ce and/or doses of O_2 for obtaining a desired reconstruction must be determined in a dedicated experiment.

The resonance photoelectron spectroscopy of the valence band is a more surface sensitive probe of the stoichiometry than the XPS because kinetic energies of the analyzed photoelectrons are lower than for XPS of Ce 3d (115 eV and 600 eV, respectively) [92]. The RPES signal is thus more closely related to the surface reconstructions observed in LEED. RPES spectra of the valence band for the samples with the LEED patterns and the XPS spectra corresponding to the Figs. 3.2 and 3.4, respectively, are shown in Fig. 3.6. The limiting cases of CeO_2 and Ce_2O_3 show only resonance enhancement D(Ce^{4+}) and D(Ce^{3+}), respectively, as is the case published in Ref. 61. The intermediate samples show a mixture of both contributions, with D(Ce^{3+}) being slightly higher on the (3×3) reconstructed sample. The degree of reduction D(Ce^{3+})/(D(Ce^{3+})+D(Ce^{4+})) equals to 0.65 and 0.71 for $(\sqrt{7} \times \sqrt{7})$R19.1° and (3×3) reconstructed samples yielding closely spaced stoichiometries of $CeO_{1.67}$ and $CeO_{1.65}$ for the near surface regions of $(\sqrt{7} \times \sqrt{7})$R19.1° and (3×3) reconstructed samples. The reduction of the samples is accompanied by a shift to higher binding energies of the Ce 4f and O 2p valence region features observed in RPES which is in accordance with the previously published data on oxidation of Ce [96].

The morphology of the reduced ceria films has been determined by STM. Ceria layers reduced by interface reaction with metallic Ce show a very good ordering due to the interface reaction [61]. CeO_2 buffer layer shows a typical average terrace width of 10 nm (Fig. 3.7(a)) corresponding to the growth temperature 250 °C [34]. After the reaction with Ce and annealing at 600 °C the resulting c-Ce_2O_3 film exhibits an increased average terrace width of 30 nm (Fig. 3.7(c)). Ordered film with average terrace width of 30 nm is observed also for ceria layers with $(\sqrt{7} \times \sqrt{7})$R19.1° reconstruction (Fig. 3.7(b)) as well as for the layers with the (3×3) reconstruction (not shown). Subsequent oxidation of the ceria films by oxygen does not greatly change the film morphology. On the c-Ce_2O_3 samples exposed to 10 000 L O_2 (Fig. 3.7(d)) the average terrace width remains without change. Occasionally deep troughs in the oxidized layers are observed. We interpret the throughs as cracks resulting from stress release in the layer during oxidation when the lattice parameter of the ceria is increasing [61].

The cracks in the ceria layers after oxidation may strongly affect the chemical reactivity of the ceria layers in model catalytic studies by exposing the very active ceria-copper interface to the reactants [97]. To assess the availability of the ceria-copper interface in our samples from Table 3.3 we determine the amount

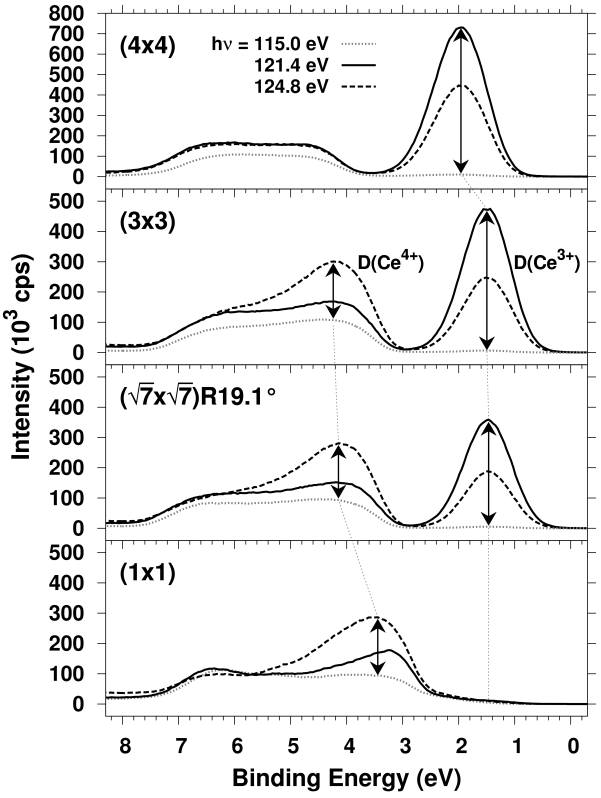

Figure 3.6: RPES spectra of the valence band of the ordered phases of reduced ceria on Cu(111). With each sample the corresponding LEED pattern is indicated. The spectra are measured off-resonance (photon energy 115 eV, dotted lines), in the Ce^{4+} resonance (124.8 eV, dashed lines) and in the Ce^{3+} resonance (121.4 eV, full lines). The resonance enhancements D(Ce^{3+}) and D(Ce^{4+}) are indicated by arrows.

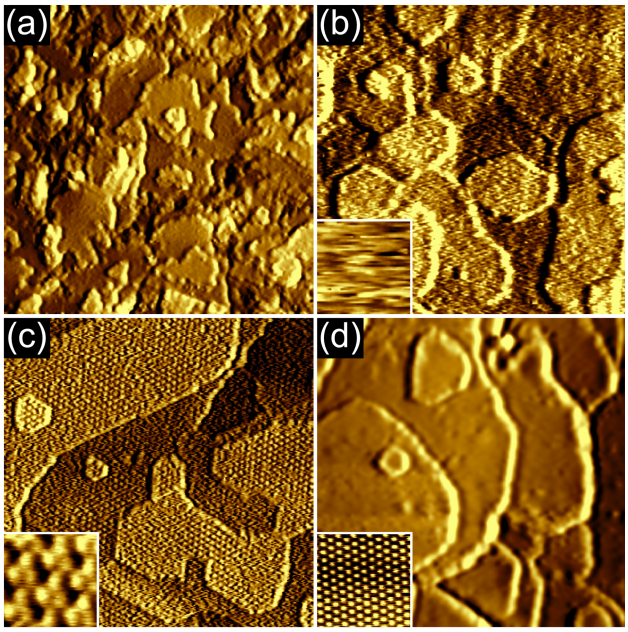

Figure 3.7: STM micrographs illustrating the morphology of cerium oxide films during reduction and reoxidation. (a) As-prepared fully oxidized buffer layer of CeO_2. (b) Ceria layer with $(\sqrt{7} \times \sqrt{7})$R19.1° surface reconstruction prepared via interface reaction of metallic Ce with CeO_2 buffer layer. Inset: The instability of the tunneling contact inherent to the $(\sqrt{7} \times \sqrt{7})$R19.1° surface reconstruction causes the streaky appearance of the layer. The morphology and the instability of the tunneling contact of the layers with (3×3) surface reconstruction is the same as in (b). (c) c-Ce_2O_3 layer prepared via interface reaction of metallic Ce with CeO_2 buffer layer. Inset: high resolution image of the (4×4) surface reconstruction of c-Ce_2O_3. (d) CeO_2 film obtained by oxidation of c-Ce_2O_3 layer. Inset: high resolution image of the (1×1) reconstruction of CeO_2. Size of images is 75×75 nm^2, size of insets 4×4 nm^2.

of the exposed Cu by ISS. The starting CeO_2 buffer prepared at 250 °C with the thickness of approximately 3 nm yields a Cu signal at the detection limit of the ISS of $\leq 0.2\%$ ML Cu (1 ML Cu represents $1.8{\times}10^{15}$ cm^{-2} Cu atoms). On the layers with the thickness of approximately 4 nm and the $(\sqrt{7} \times \sqrt{7})$R19.1°, (3×3), and (4×4) reconstructions prepared by deposition of Ce and the interfacial reaction on the CeO_2 buffer the Cu signal is not measurable by ISS. On the contrary, the layers with (3×3), $(\sqrt{7} \times \sqrt{7})$R19.1°, and (1×1) reconstructions prepared by oxidation of the layers with the (4×4) reconstruction yield Cu signals between 0 and 2% ML Cu. Thus, the layers of ordered reduced ceria obtained in our experiment by interface reaction between Ce and the CeO_2 buffer are continuous and free of Cu. However, the oxidation of the continuous layer of reduced ceria on Cu may eventually expose the ceria-copper interface which must be accounted for when evaluating the chemical reactivity of such layers.

The STM images in Fig. 3.7 are presented as illuminated from the right to enhance the surface texture on the terraces related to the respective surface reconstruction. This texture is most pronounced for the (4×4) reconstructed samples of Ce_2O_3 (Fig. 3.7(c) and the inset of Fig. 3.7(c)). After oxidation of the Ce_2O_3 layer the texture vanishes and the surface converts to the (1×1) reconstruction

(Fig. 3.7(d) and the inset of Fig. 3.7(d)). For samples with the $(\sqrt{7}\times\sqrt{7})$R19.1° surface reconstruction the STM images show streaks indicative of instability of the surface in the tunneling contact. The surface texture cannot be resolved in STM (Fig. 3.7(b) and the inset of Fig. 3.7(b)). The same instability is observed on the samples with the (3×3) surface reconstruction. The instability in STM is a property of the $(\sqrt{7}\times\sqrt{7})$R19.1° and (3×3) surface reconstructions independent of the imaging condition of the STM tip. On the samples where $(\sqrt{7}\times\sqrt{7})$R19.1° and/or (3×3) surface reconstructions coexist with the (4×4) reconstruction, the areas with (4×4) reconstruction appear stable and well resolved next to the instable areas with $(\sqrt{7}\times\sqrt{7})$R19.1° and/or (3×3) reconstructions in the same STM image.

■ Discussion

Reduction of ceria films by the interface reaction with Ce eventually complemented by oxidation with O_2 allows us to prepare ceria thin films on Cu(111) in the whole range of stoichiometries between CeO_2 and Ce_2O_3. The films exhibit four distinct surface reconstructions, (1×1) (CeO_2), $(\sqrt{7}\times\sqrt{7})$R19.1°, (3×3), and (4×4) (Ce_2O_3) as identified by LEED. The discussion of our experiment is devoted to the following aspects: i) We give arguments that all the observed surface reconstructions are based on ordering of oxygen vacancies in cubic fluorite-like ceria, ii) we estimate the stoichiometry and propose a model of the (3×3) surface reconstruction, iii) we estimate and rationalize the depth profile of the vacancy concentration in the $(\sqrt{7}\times\sqrt{7})$R19.1° and (3×3) reconstructed layers, and iv) we propose a mechanism leading to the nucleation of the cubic ceria phase during reduction of ceria layers via the interface reaction with Ce. In our arguments we recall the experimental observation of Perkins et al.[62] concerning the bulk mobility of O and Ce atoms in fluorite-like ceria: At temperatures around 600 °C corresponding to the annealing temperature in our experiment, Ce atoms are virtually immobile in the ceria bulk, while O atoms are already highly mobile, their bulk mobility being released at temperatures as low as 300 °C [62]. In terms of this observation, we are viewing all changes in the ordered reduced ceria layers in our experiment as creation, annihilation, and equilibration of oxygen vacancies in a relatively rigid frame of cubic ceria.

i) There is a strong experimental evidence of ordering of oxygen vacancies in bulk reduced ceria (Ref. 26 and references therein), and several phases of bulk reduced ceria with stoichiometries approximately between $CeO_{1.81}$ and $CeO_{1.66}$ have been identified in neutron diffraction experiments [17, 86]. These phases are obtained by removing oxygen atoms from fluorite lattice of CeO_2 and ordering of the resulting oxygen vacancies to superstructures with distinct spatial correlations [17]. Recently, two of these bulk structures have been employed successfully in explaining the reconstructions observed in LEED on thin films of reduced ceria. The $(\sqrt{7}\times\sqrt{7})$R19.1° LEED pattern on a layer of CeO_x was associated with a bulk termination of ι-Ce_7O_{12} phase [86, 88]. The (4×4) LEED pattern on a layer of Ce_2O_3 was associated with a bulk termination of c-$Ce_2O_{3+\delta}$ phase [17, 61] that was realized for δ=0 as a thin film of c-Ce_2O_3 on Cu(111). Both $(\sqrt{7}\times\sqrt{7})$R19.1° and (4×4) reconstructions are realized in the present experiments as well. Further, the present experiments reveal a (3×3) surface reconstruction for ceria layers that

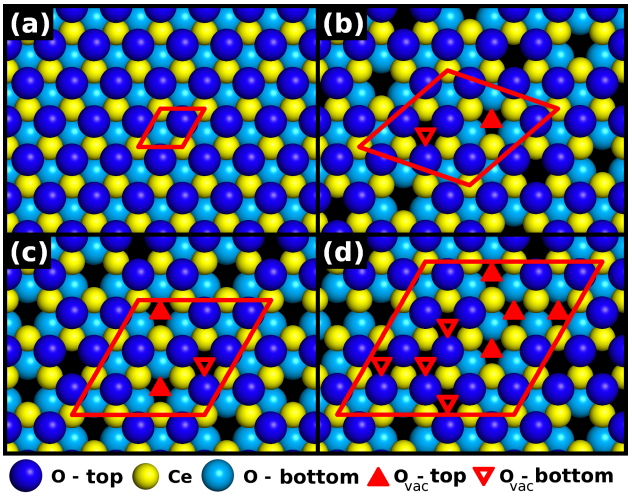

Figure 3.8: Schematic top view of the ordered phases of reduced ceria on Cu(111). Images represent one monolayer from the related bulk structure. (a) $CeO_2(111)$ corresponding to the LEED pattern (1×1) on Fig. 3.2(a), bulk structure ICSD #169029, (b) ι-$Ce_7O_{12}(111)$ corresponding to the LEED pattern $(\sqrt{7}\times\sqrt{7})$R19.1° on Fig. 3.2(b), bulk structure PCD #1805255, (c) $CeO_{1.67}$ corresponding to the LEED pattern (3×3) on Fig. 3.2(c), proposal of the present work, (d) c-$Ce_2O_3(111)$ corresponding to the LEED pattern (4×4) on Fig. 3.2(d), bulk structure ICSD #96202. Surface unit cells are highlighted by red line, top and bottom O vacancies are highlighted by full and empty red triangles, respectively.

are according to XPS and RPES more reduced than $(\sqrt{7}\times\sqrt{7})$R19.1° terminated layers, but less reduced than (4×4) terminated layers (cf. Figs. 1–3). We propose that the (3×3) terminated phase can be derived from bulk ordering of oxygen vacancies in cubic ceria as well. The main argument for our proposal is the observation that the (3×3) terminated phase can be obtained by oxidation of the cubic $Ce_2O_3(4 \times 4)$ phase at temperatures when the Ce atoms are virtually immobile (cf. Figs 3.4 and 3.5, and Perkins et al. [62]).

ii) With this evidence for the cubic structure of the (3×3) surface reconstruction we can propose the microscopic model of this reconstruction in analogy with the models of $(\sqrt{7} \times \sqrt{7})$R19.1° and (4×4) reconstructions. All models for the surface reconstructions observed in our experiments are displayed in Fig. 3.8. The models are presented as top views of one monolayer of ceria oriented in (111) direction of the fluorite lattice corresponding to a particular bulk model of the reduced ceria. When available, the bulk models are adopted from crystallographic databases, the Inorganic Crystal Structure Database (ICSD) and the Pearson's Crystal Data (PCD). Fig. 3.8(a) displays the reference (111) plane of CeO_2 (bulk model ICSD #169029). Fig. 3.8(b) displays the corresponding cut through bulk ι-Ce_7O_{12} phase (PCD #1805255) according to Wilkens et al. [88], and Fig. 3.8(d) the cut through bulk c-Ce_2O_3 phase (ICSD #96202) according to Stetsovych et al. [61] In the figures, the surface unit cell corresponding to the LEED patterns of (1×1) (Fig. 3.8(a)), $(\sqrt{7} \times \sqrt{7})$R19.1° (Fig. 3.8(b)), and (4×4) (Fig. 3.8(d)) is outlined red and the positions of the oxygen vacancies in the upper and lower O layers in the ceria monolayer by full and empty red triangles respectively.

For the model of the (3×3) reconstruction we have to estimate the number and the positions of the oxygen vacancies in the (3×3) surface unit cell relative to $CeO_2(111)$. According to the XPS measurements (Fig. 3.5), the stoichiometry of the (3×3) surface reconstruction is intermediate between the $(\sqrt{7}\times\sqrt{7})$R19.1° (ι-Ce_7O_{12} or $CeO_{1.71}$) and the (4×4) (c-Ce_2O_3 or $CeO_{1.5}$) reconstructions. According to RPES measurements (Fig. 3.6) the stoichiometry of the (3×3) reconstruction is close to the $(\sqrt{7}\times\sqrt{7})$R19.1° ($CeO_{1.71}$) reconstruction. Therefore, we propose that the (3×3) surface unit cell includes 3 oxygen vacancies corresponding to the model stoichiometry $CeO_{1.67}$. Regarding the positions of the oxygen vacancies in the model of the (3×3) reconstruction we recall the preferential orientations of vacancy pairs in ceria bulk observed and analyzed in neutron diffraction experiments [17]. Particularly, oxygen vacancies in the bulk tend to repel each other, and show a strong preference for certain spatial correlations. These rules for vacancy ordering determine the models of the $(\sqrt{7}\times\sqrt{7})$R19.1° surface reconstruction (Fig. 3.8(b)) and the (4×4) surface reconstruction (Fig. 3.8(d)). The (3×3) surface reconstruction cannot be identified as a simple cut through any of the established models of bulk reduced ceria, however, the oxygen vacancies can be positioned in the preferred mutual positions as well. This is shown in our proposal for the model of the (3×3) reconstruction in Fig. 3.8(c). The spatial correlations of vacancies in the model of the (3×3) reconstruction are those appearing in the models of the $(\sqrt{7}\times\sqrt{7})$R19.1° and the (4×4) reconstructions, too.

We have to note that the models of the reduced ceria surfaces derived from the bulk phases of reduced ceria have to be considered only as suggestions plausibly explaining the superstructures observed in LEED and subject to further refinement by microscopic, diffraction, and ab-initio techniques. The rules governing the ordering of the oxygen vacancies on the surfaces of reduced ceria seem to be still more complex. Indeed, oxygen vacancies observed on the reduced ceria surfaces by microscopic techniques adopt spatial correlations that are not realized in bulk. Esch et al. [15] observe and rationalize based on ab-initio calculations a stabilization of surface vacancy chains by a subsurface vacancy corresponding to a (0,0,1) vacancy pair in the notation of Kümmerle and Heger. Torbrüge et al. [98] observe and Murgida et al. [99] rationalize based on ab-initio calculations a stabilization of subsurface vacancies as (0,2,2) vacancy pairs. Both (0,0,1) and (0,2,2) vacancy pairs are not realized in bulk samples [17].

Unfortunately, microscopic evidence for the vacancy distribution on $(\sqrt{7}\times\sqrt{7})$R19.1° and (3×3) terminated samples could not be obtained in this work due to an inherent instability of the STM images of the $(\sqrt{7}\times\sqrt{7})$R19.1° (Fig. 3.7(b)) and (3×3) reconstructions in our experimental setup. Since in comparable STM experiments the surface vacancies on ceria seem to be immobile [15, 100] we assign the instability of the STM images to water molecules accumulating on the $(\sqrt{7}\times\sqrt{7})$R19.1° and (3×3) surfaces in our STM during the prolonged measuring sessions without the possibility of flash heating of the samples.

iii) The models of the $(\sqrt{7}\times\sqrt{7})$R19.1° and (3×3) surface reconstructions of the reduced ceria layers in our experiment predict the stoichiometry of the corresponding reduced bulk phases $CeO_{1.71}$ and $CeO_{1.67}$, respectively. For the comparison with the experiment we have to realize the different information depth of the employed experimental methods for determining the stoichiometry. The

reconstruction (Fig. 3.2)	x in CeO_x			
	XPS 0° (Fig. 3.4)	XPS 70° (Fig. 3.4)	RPES (Fig. 3.6)	model (Fig. 3.8)
$(\sqrt{7} \times \sqrt{7})$R19.1°	1.86	1.82	1.67	1.71 [88]
(3×3)	1.78	1.70	1.65	1.67

Table 3.2: Stoichiometries determined from experiments with different information depth.

overview of the stoichiometry of the layers with the $(\sqrt{7} \times \sqrt{7})$R19.1° and (3×3) surface reconstructions (Fig. 3.2) measured by XPS at normal emission (Figs. 3.4, 3.5), XPS at 70° off normal emission (Figs. 3.4, 3.5), and RPES (Fig 3.6) in comparison with the predicted stoichiometry (Fig. 6) is presented in Table 3.2. We observe that the predicted and the measured values of the stoichiometry of the layers correspond reasonably well only for the most surface sensitive measurement by RPES. Measurements by XPS show stoichiometries that are less reduced than expected. The experimentally determined degree of reduction decreases with the increasing information depth of the employed experimental method. This suggests that the reduced ceria phases Ce_7O_{12} and $CeO_{1.67}$ are floating on a more oxidized ceria.

We propose that the enhancement of the concentration of the oxygen vacancies near the surface of the reduced ceria films represents a general effect resulting from equilibrium distribution of the oxygen vacancies in thin CeO_x films. The equilibrium is indicated by the independence on the preparation history of the samples (Fig. 3.5). The enhanced concentration of surface vacancies is observed for the samples prepared both by reduction of CeO_2 by Ce and by oxidation of Ce_2O_3 by O_2. The equilibration is mediated by a high mobility of oxygen atoms and oxygen vacancies in the CeO_x thin films at temperatures well below the annealing temperature of 600 °C used during the sample preparation in the present study [62]. Oxygen vacancies near the surface are thermodynamically favorable as predicted by theoretical calculations [13, 23]. Oxygen vacancies may also respond sensitively to the strain in the ceria film. Oxygen vacancies expand the lattice parameter of the reduced ceria due to a larger diameter of the associated Ce^{3+} cations compared to the Ce^{4+} cations in the oxidized ceria [26, 61]. The presence of the ceria–Cu(111) interface in the metal supported thin ceria film on the other hand induces a contraction of the lattice parameter of ceria [36, 101]. The interplay between these two effects ultimately results in a force driving the oxygen vacancies away from the ceria–Cu(111) interface and towards the surface of the film. The enhancement of the oxygen vacancy concentration near the surface of ceria was predicted and observed also in ceria nanoparticles [102, 103].

The change of the vacancy concentration with the distance from the surface of the reduced ceria is most likely continuous, but we can estimate a characteristic length scale over which the change of the vacancy concentration is taking place using a simple two level model of Ref. 104. This model assumes a homogeneous layer of reduced ceria (in our case with the stoichiometry $CeO_{1.71}$ or $CeO_{1.67}$) floating on the homogeneous CeO_2. The thickness of the reduced ceria layer can then be determined from XPS measurements at normal emission using the following equation [104]: $I_s(\mathrm{Ce}^{4+}_{composite}) - I_s(\mathrm{Ce}^{4+}_{overlayer}) = I_s(\mathrm{Ce}^{4+}_{buffer}) \exp\left(-\frac{d}{\lambda}\right)$, where $I_s(\mathrm{Ce}^{4+}_{composite})$ is the Ce^{4+} signal measured on the reduced layers, $I_s(\mathrm{Ce}^{4+}_{overlayer})$

is the simulated Ce^{4+} signal corresponding to the $CeO_{1.71}$ or $CeO_{1.67}$ overlayer computed from the measured Ce^{3+} signal and the expected stoichiometry of the overlayer, $I_s(Ce^{4+}_{buffer})$ is the Ce^{4+} signal from the CeO_2 buffer layer (in case of the films prepared by oxidation the signal from fully oxidized film is used instead), d is the thickness of the $CeO_{1.71}$ or $CeO_{1.67}$ overlayers and λ is the inelastic mean free path in the reduced layers. The results of this simple estimation show that the samples with the $(\sqrt{7} \times \sqrt{7})$R19.1° reconstruction consist of 2–3 ML of $CeO_{1.71}$ supported by CeO_2 and the samples with the (3×3) reconstruction consist of 3–4 ML of $CeO_{1.67}$ supported by CeO_2.

iv) The observation of the cubic structure of the ceria layers in our experiment in the whole range of stoichiometries between CeO_2 and Ce_2O_3 is allowed by the special property of the alternative method of reduction of ceria by the reaction with metallic Ce to yield the cubic structure even for the limiting reduction to Ce_2O_3 where hexagonal Ce_2O_3 is the lowest energy configuration [25, 96, 105]. We propose a model for the stabilization of the cubic reduced ceria in the interface reaction. The illustration of this model is in Fig. 3.9. A starting point is the deposition of Ce metal on the cubic ceria buffer. The cubic ceria buffer is available in all our experiments, cf. Figs 3.4, 3.5 and Table 3.3. After heating to 600 °C, oxygen from the ceria buffer diffuses into the Ce overlayer and oxidizes it (Fig. 3.9(a)). The oxidized Ce in the overlayer adopts the cubic structure of the buffer that acts as a nucleation template. In this way, the system also avoids an energy increase associated with an eventual nucleation of an interface between the cubic and the hexagonal ceria (Fig. 3.9(b)). Finally, upon oxidation of the Ce overlayer that establishes the cubic structure in the film the oxygen vacancies adopt an equilibrium distribution with a maximum of concentration near the surface of the film (Fig. 3.9(c)). The gradient of distribution of oxygen vacancies is not observed for the samples with the limiting stoichiometry—CeO_2 and Ce_2O_3 (Fig. 3.5)—because in these samples the vacancies occupy no (in CeO_2) or all (in Ce_2O_3) available positions. During transitions between CeO_2 and Ce_2O_3 the ordered thin film of reduced ceria must adapt to the accompanying changes of the ceria lattice constant. [61] On Cu(111), this adaptation is facilitated by the incommensurate character of growth of ceria on Cu(111) and by the ability of ceria films to glide on Cu(111) substrate [33].

■ Conclusion

We have performed a detailed study of the properties of thin films of reduced ceria on Cu(111) prepared by the interfacial reaction between a ceria thin film and a Ce metal deposit. Thin films of reduced ceria are continuous and completely cover the Cu substrate. Controlling the amount of Ce in the interfacial reaction, we can prepare thin films of reduced ceria with stoichiometry changing continuously between CeO_2 and Ce_2O_3. The change in the stoichiometry is accompanied by changes in the surface reconstruction of the films. Starting from the (1×1) reconstruction of CeO_2 and increasing the degree of reduction we observe $(\sqrt{7} \times \sqrt{7})$R19.1° and (3×3) reconstructions of CeO_x, and, finally, the (4×4) reconstruction of cubic Ce_2O_3. In the films with stoichiometry between CeO_2 and Ce_2O_3 the oxygen vacancies accumulate near the surface of the films.

We observe that the process of reduction of thin ceria films by the interfacial

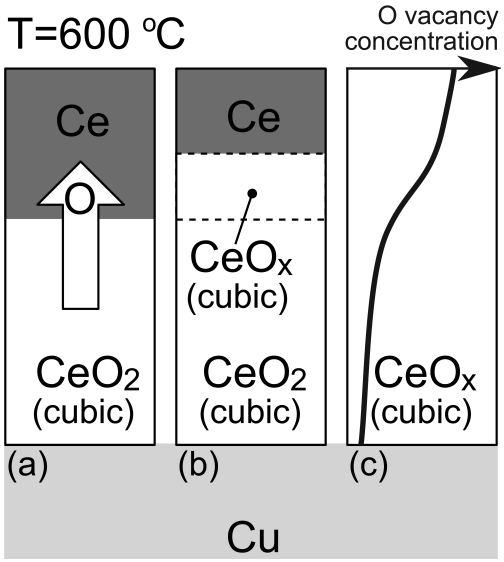

Figure 3.9: Schematic drawing of the interface reaction upon deposition of metallic Ce (dark gray) on ceria buffer layer (white) on the Cu(111) substrate (light gray) and heating the system to 600 °C. (a) O diffuses from the ceria buffer to oxidize the Ce deposit. (b) Oxidized Ce in the deposit adopts the cubic structure of the buffer. (c) O vacancies in the resulting layer equilibrate establishing a concentration gradient with maximum of O vacancies near the surface.

reaction with Ce is fully reversible upon oxidation with O_2. This reversibility covers all properties of the reduced ceria thin films including the surface reconstructions and the depth profile of oxygen vacancies. This allows us to discuss the properties of the ceria layers in terms of equilibration of mobile oxygen vacancies in a relatively rigid cubic lattice of cerium atoms. The cubic structure of the reduced ceria layers is established during the interface reaction with Ce. Oxygen vacancies are driven away from the Cu(111)–ceria interface in order to relieve the stress associated with the expansion of the lattice constant during the reduction of ceria. The $(\sqrt{7}\times\sqrt{7})$R19.1° and (3×3) reconstructions are identified as surface terminations of ordered bulk phases of reduced ceria, the ι-Ce_7O_{12} or $CeO_{1.71}$ phase for the $(\sqrt{7}\times\sqrt{7})$R19.1° reconstruction, and the $CeO_{1.67}$ phase for the (3×3) reconstruction. These bulk reduced phases representing distinct regular arrangements of oxygen vacancies in cubic ceria are established in the three topmost monolayers of the reduced ceria films.

Practically, ceria layers reduced by the interface reaction with metallic Ce represent a realization of the ideal scenario of reduction and reoxidation of ceria by removing/adding O from/to the fluorite CeO_2 lattice without largely modifying the structure of the Ce sublattice [16]. This, accompanied by the preference of oxygen vacancies to arrange in regular structures makes the ceria layers reduced by interface reaction with metallic Ce a unique experimental playground for studying the influence of the oxygen vacancy concentration and coordination on the chemical properties of ceria.

■ Acknowledgments

This work was supported by the Czech Science Foundation (GAČR P204-11-1183, GAČR 13-10396S) and by the Ministry of Education of the Czech Republic (LG12003, LH11017). T.D., F.D., M.A., and V.S. acknowledge the support of the Grant Agency of the Charles University (GAUK 794313, GAUK 610112, GAUK 320313, GAUK 339311). We would also like to thank Radomír Kužel for the discussion of ICSD and PCD data.

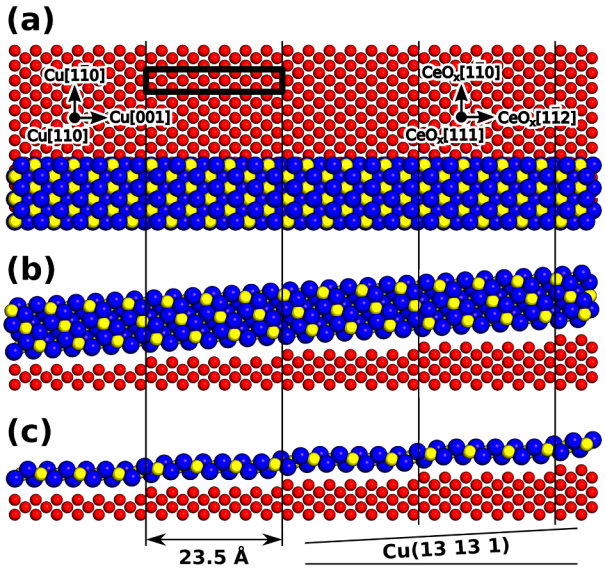

Figure 3.10: (a) Microscopic model of CeO_x/Cu(13 13 1). The copper atoms are shown in red, cerium atoms in yellow and oxygen atoms in blue. The cerium oxide overlayer induces reconstruction of Cu(110) substrate, and grows over it in a carpet-like fashion, copying the substrate at 1 ML thickness (c) and lying unperturbed over it at 2 ML and thicker (b).

3.2 The effect of substrate in oxygen vacancy ordering

Substrate is an important part of all heteroepitaxially grown thin films and poses an important question in model catalysis: How does the substrate affect properties of model systems? And, consequently, from what thickness do thin films exhibit bulk-like properties? While it is impossible to provide a general answer to these questions, there are several indicators that can be discussed. The most obvious effect of the substrate is a strain introduced in the grown film due to lattice mismatch. This is commonly reflected by a divergence of the lattice parameter of the film from the bulk material. However, it is often difficult to establish whether the divergence arises due to the interface with substrate or just due to reduced dimensionality of the material. Thin films of cerium oxide terminated by the (111) surface generally exhibit contracted lattice parameter and do not reach the bulk value even at the thickness of 2 nm [101]. Interestingly, the contraction actually increases the lattice mismatch with the substrate. This indicates that the substrate is probably not determining the lattice parameter. Precise measurements of strain distribution in thin cerium oxide islands on Cu(111) also showed that the shape and thickness of the islands are governing the strain [33]. Cerium oxide has also been shown to grow in a carpet-like fashion on several substrates and even inducing reconstruction of the substrate (see Figure 3.10), indicating that intralayer interaction in cerium oxide is much stronger than the cerium oxide–substrate interaction [106]. It should be noted that the above-mentioned observations were made on metal substrates and can't be carried over to other substrates, such as oxides.

It is therefore reasonable to expect cerium oxide films to behave in the same manner with respect to oxygen vacancy ordering irrespective of the metal substrate used for the growth. In order to make sure this is the case, the experiment from the previous section has been repeated with Ru(0001), a substrate that is commonly used for the growth of cerium oxide films. Indeed, the exact same trends are observed for the CeO_2 to Ce_2O_3 transition, validating generalization of the conclusions made in the previous section.

Comment on "Ordered phases of reduced ceria as epitaxial films on Cu(111)"

Tomáš Duchoň, Filip Dvořák, Marie Aulická, Vitalii Stetsovych, Mykhailo Vorokhta, Daniel Mazur, Kateřina Veltruská, Tomáš Skála, Josef Mysliveček, Iva Matolínová, and Vladimír Matolín

Faculty of Mathematics and Physics, Department of Surface and Plasma Science, Charles University, V Holešovičkách 2, 18000 Prague 8, Czech Republic

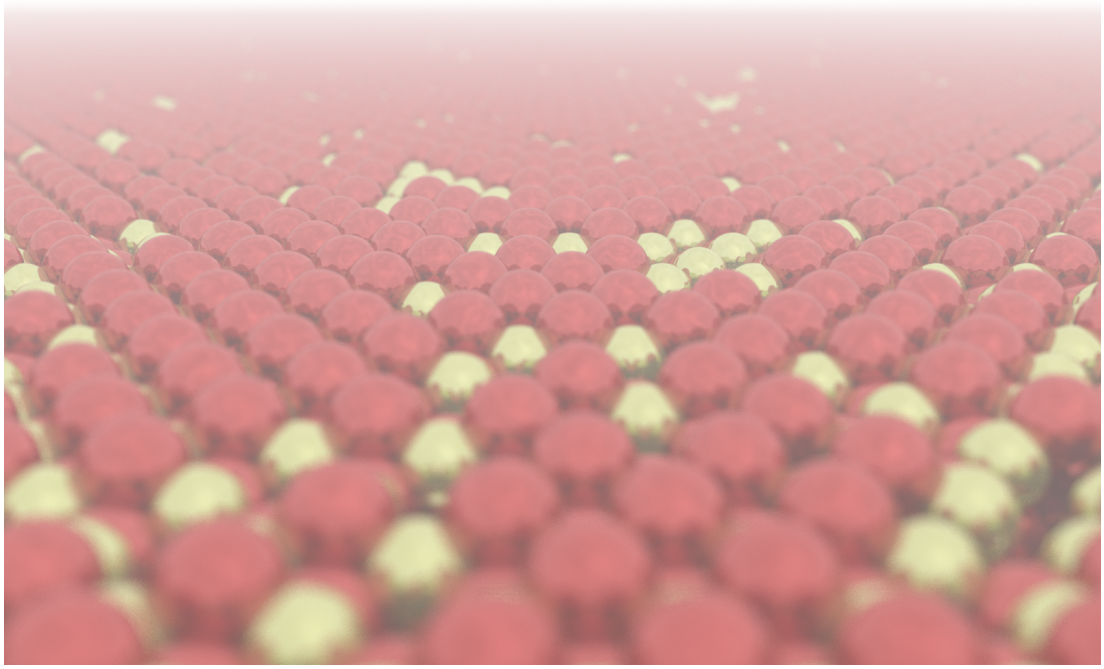

reconstruction	thickness of the CeO_2 buffer	thickness of the reacted layer
(1×1)	2.8 nm	-
$(\sqrt{7} \times \sqrt{7})$R19.1°	2.8 nm	3.2 nm
(3×3)	2.8 nm	3.5 nm
(4×4)	2.8 nm	4.1 nm

Table 3.3: Parameters of the preparation of the samples.

In our recent contribution [1] we have described a method for obtaining ordered layers of reduced ceria by interfacial reaction between a metallic Ce deposit and a CeO_2 buffer layer supported on Cu(111). In this Comment, we demonstrate the applicability of this method on ceria layers supported on Ru(0001). Ru(0001) is a widely used support for model ceria catalysts with a large body of studied heterogeneous surface chemical reactions [27, 107, 108]. Ordered layers of reduced ceria now offer the possibility to control both the concentration and the coordination of oxygen vacancies in ceria and to investigate the surface chemistry of well-defined sub-stoichiometric ceria.

With the clean Ru(0001) substrate we exactly reproduce the experimental procedures of Ref (1) and prepare ordered layers of reduced ceria with thickness of 3 to 4 nm. The thickness of the layers is determined from the attenuation of Ru $3d_{5/2}$ in XPS. Photoelectron spectra (XPS) and electron diffraction (LEED) of the layers are displayed in Figures 1 and 2, respectively. The growth parameters, the degree of reduction and the estimate of the in-plane lattice constant of the layers are summarized in Tables 1 and 2.

Ceria layers exhibit the same characteristic behaviour as the layers on Cu(111) [1]. Particulary, the stoichiometry of the layers can be tuned from CeO_2 to Ce_2O_3 by varying the amount of metallic Ce in the interfacial reaction. During the transition from CeO_2 to Ce_2O_3 we observe the same surface reconstructions corresponding to ordered phases of reduced ceria. (1×1) reconstruction corresponds to $CeO_2(111)$, $(\sqrt{7} \times \sqrt{7})$R19.1° to ι-Ce_7O_{12}, (3×3) to $CeO_{1.67}$, and (4×4) to Ce_2O_3 [1]. On the starting CeO_2 buffer with (1×1) reconstruction a weak rotational domain characteristic for growth of CeO_2 on Ru(0001) is apparent [107, 108]. As with Cu(111) substrate, the degree of reduction of the ceria layers is larger when measured with higher surface sensitivity (60° vs. 0° off sample normal, Table 2). As the degree of reduction increases, we observe the accompanying relaxation and the effective increase of the in-plane lattice constant of the ceria layers (Table 2) [61].

Our results show that reduction of ceria layers in the interfacial reaction with metallic Ce is applicable on Ru(0001), and, presumably, on other metal substrates with the same results as on the Cu(111) substrate. The general conclusion of Ref (1) that the properties of the thin films of reduced ceria are determined by equilibration of mobile oxygen vacancies in a relatively rigid lattice of cubic ceria seems to be independent of the choice of the metal substrate.

■ Acknowledgments

This work was supported by the Czech Science Foundation (GAČR P204-11-1183, GAČR 13-10396S) and by the Ministry of Education of the Czech Republic (LG12003, LH11017). T.D., F.D., M.A., and V.S. acknowledge the support of the

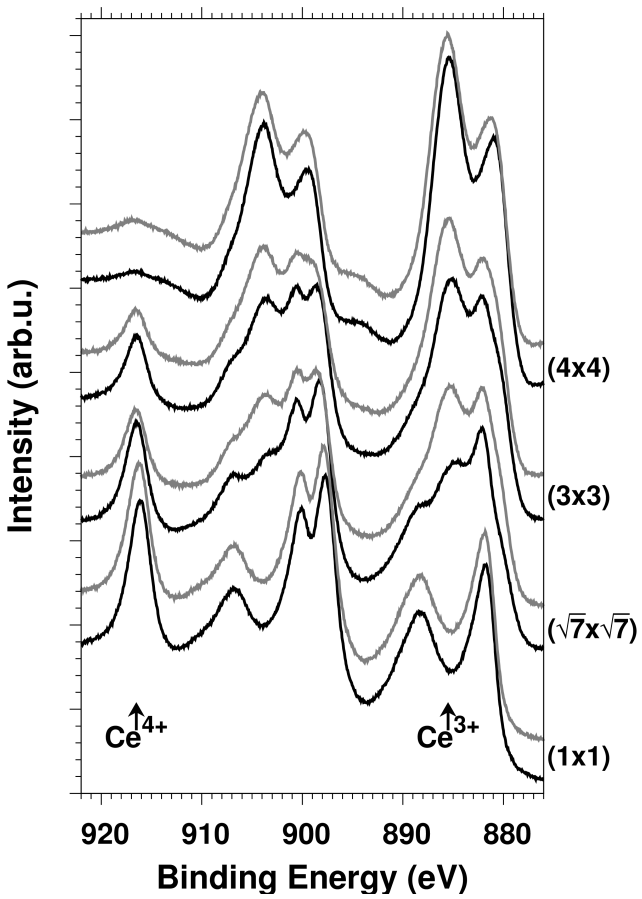

Figure 3.11: XPS spectra of the ordered phases of ceria on Ru(0001). Spectra were measured at 0° (black curves) and 60° off-normal emission (gray curves). The areas of the presented spectra have been normalized to 1 and the curves have been offset for clarity. For better orientation, the positions of visually the most prominent peaks in Ce^{4+} and Ce^{3+} spectra are marked by arrows.

reconstruction	x in CeO_x		in-plane lattice constant
	XPS 0°	XPS 60°	
(1×1)	1.99	1.99	3.80±0.05 Å
$(\sqrt{7} \times \sqrt{7})$R19.1°	1.83	1.76	3.83±0.05 Å
(3×3)	1.72	1.66	3.87±0.05 Å
(4×4)	1.51	1.50	3.90±0.05 Å

Table 3.4: Stochiometries and in-plane lattice constants of the samples.

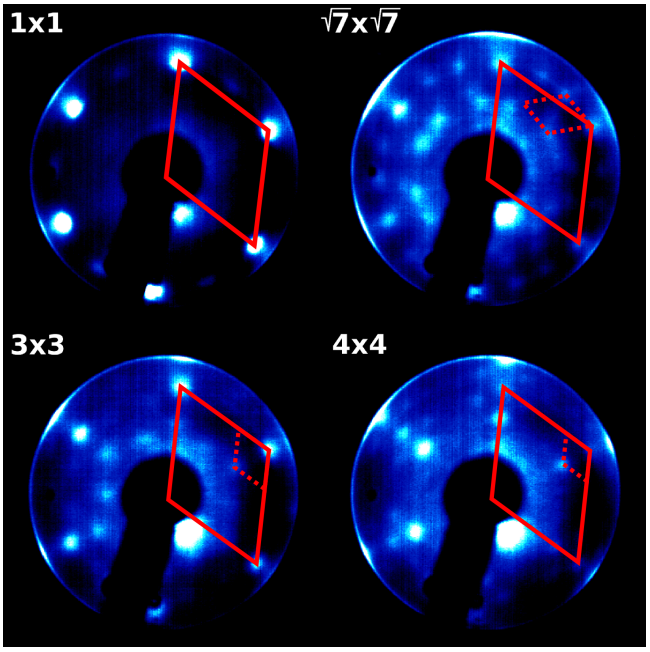

Figure 3.12: LEED patterns of the ordered phases of ceria on Ru(0001) measured at primary electron energy of 40 eV. The surface unit cells of CeO_2 (solid line) and the respective reconstructions of reduced ceria (dashed line) are outlined in red.

Grant Agency of the Charles University (GAUK 794313, GAUK 610112, GAUK 320313, GAUK 339311).

3.3 Model systems for structure–activity relationship studies

Structure–activity relationship is one of the most important concepts in heterogeneous catalysis. Specific structural features, such as steps or facets, often exhibit orders of magnitude higher activity in chemical conversion [109, 110]. Proper understanding of their role is thus crucial for rational design of catalysts. The dominant structural element of a catalyst is its surface. Consequently, activity variation between stable low-index surface terminations is the main factor in determining activity of a nanostructured catalyst. In the case of cerium oxide, (111), (110) and (100) surface terminations exposed by nanooctahedrons, nanorods and nanocubes are the focus of structure–activity investigations (see Figure 3.13) [111]. The amount of work devoted to the respective surfaces corresponds to their stability, with (111) being the most prevalent [10]. However, model systems of the low-index surfaces are always studied in isolation, making accurate comparison difficult.

Herein, a novel method for control of surface termination of oxides heteroepitaxially grown on metals is presented. Through adjustment of oxygen chemical potential at the surface a surprising variety in shape and crystalline orientation of cerium oxide particles on Cu(111) surface is revealed, allowing for exclusive synthesis of well-defined, micron-sized model systems with variable termination. The contribution provides new insights into fundamental mechanisms operative in rare-earth and binary oxide heteroepitaxy. Remarkably, cerium oxide particles exhibiting different surface terminations can be prepared next to each other, representing a first-of-a-kind playground for direct comparison of surface terminations under identical conditions.

Continuing from the previous work, the new method is utilized in a study of the effect of surface termination on oxygen vacancy ordering in cerium oxide, comparing CeO_2(111) and CeO_2(100). Cerium oxide is again shown to keep the fluorite lattice throughout the CeO_2 to Ce_2O_3 transition (keeping in mind that the annealing temperature is below 600 °C). Distinct reconstructions of the CeO_x(100) surface are observed — c(2 × 2), p(2 × 2) and c(4x4). The observations epitomize the flexibility of Ce-ceria interfacial interaction in revealing ordering of oxygen vacancies in cerium oxide. In conjunction with adjustment of oxygen chemical potential the Ce-ceria interfacial interaction facilitates unparalleled control over structure and stoichiometry of cerium oxide model systems, a control that can be easily carried over to other reducible oxides.

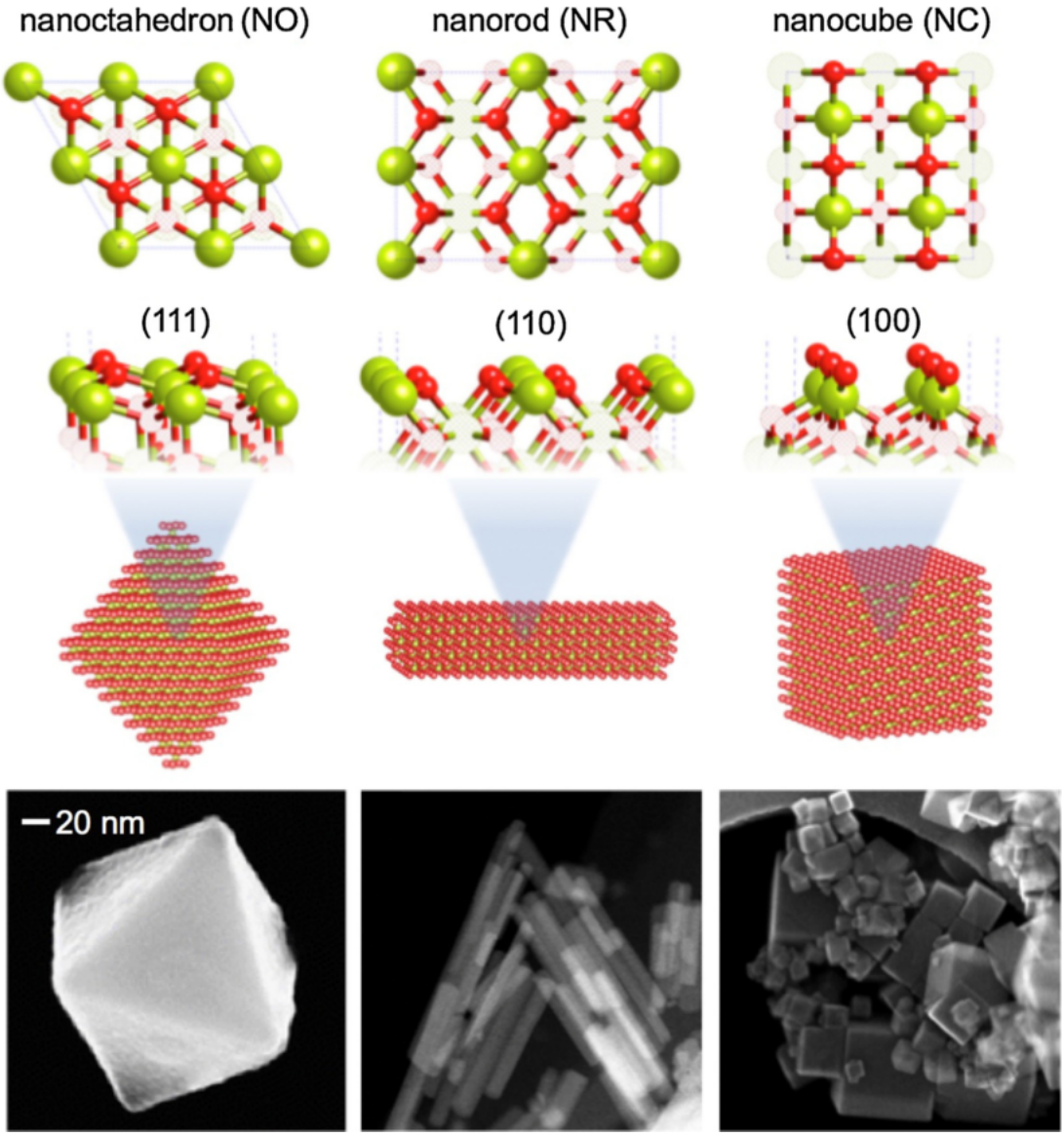

Figure 3.13: (a) Microscopic models and micrographs of cerium oxide nanooctahedra (left), nanorods (middle), and nanocubes (right). [111]

Controlling heteroepitaxy by oxygen chemical potential: exclusive growth of (100) oriented ceria nanostructures on Cu(111)

Jan Höcker[†], Tomáš Duchoň[‡*], Kateřina Veltruská[‡], Vladimír Matolín[‡], Jens Falta[†§], Sanjaya D. Senanayake[¶], and Jan Ingo Flege[†]*

[†]Instiitute of Solid State Physics, University of Bremen, Otto-Hahn-Allee 1, 28359 Bremen, Germany
[‡]Faculty of Mathematics and Physics, Department of Surface and Plasma Science, Charles University, V Holešovičkách 2, 18000 Prague 8, Czech Republic
[§]MAPEX Center for Materials and Processess, University of Bremen, 28359 Bremen, Germany
[¶]Chemistry Department, Brookhaven National Laboratory, Upton, New York 11973, United States

A novel and simple method is presented for the preparation of a well-defined $CeO_2(100)$ model system on Cu(111) based on the adjustment of the Ce/O ratio during growth. The method yields micrometer-sized, several nanometers high, single-phase $CeO_2(100)$ islands with controllable size and surface termination that can be benchmarked against (111) nanostructured islands prepared on the same Cu(111) surface. Furthermore, we demonstrate the ability to adjust the Ce to O stoichiometry from $CeO_2(100)$ (100% Ce^{4+}) to c-$Ce_2O_3(100)$ (100% Ce^{3+}), which can be readily recognized by characteristic surface reconstructions observed by low-energy electron diffraction. The discovery of the highly stable $CeO_x(100)$ phase on a hexagonally close packed metal surface represents an unexpected growth mechanism of ceria on Cu(111), and it provides an opportunity to prepare more elaborate models, benchmark surface chemical reactivity and thus gain valuable insights into the redox chemistry of ceria in catalytic processes.

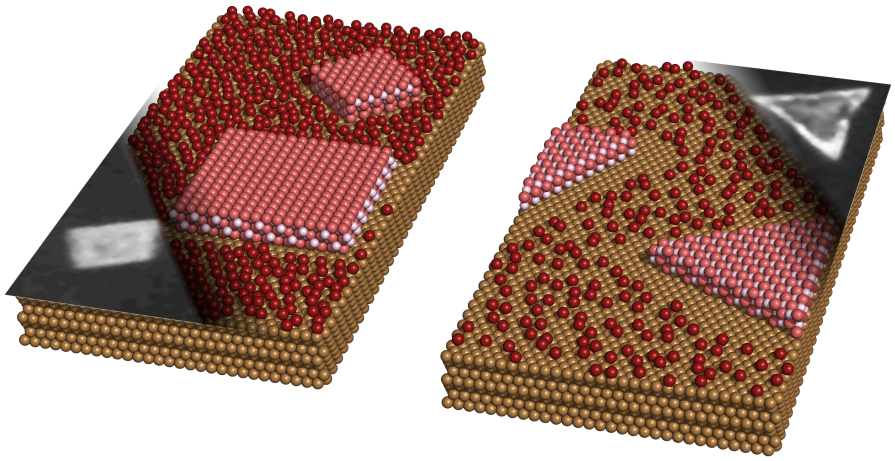

1

[1]J.H. and T.D. contributed equally to this work.

■ Introduction

Cerium oxides are a heavily utilized and studied prototype oxide associated with demanding catalytic conversion. Ceria-based heterogeneous catalysts take advantage of a plethora of unique properties including versatile redox properties (Ce^{4+} - Ce^{3+}), oxygen storage, and reducibility. In addition, reactions can be steered by architectured and morphologically constrained supports of ceria, such as nanocubes, nanorods, and nanopolyhedra [112]. These nanostructured catalysts provide much sought after improvements in selectivity, reactivity, and other catalytically relevant parameters through surface terminations and metal-support interactions [113, 114]. Polycrystalline nanostructured catalysts of ceria that expose a variety of low index planes have been prepared through wet chemistry and tested for catalytic activity. Specifically, the (100) surface exposed in nanocubes has been recently shown, in contrast to the (111) surface, to exhibit a high activity in CO oxidation [11] and an enhanced activity for the dehydrogenation of methoxy species [12]. However, with Cu loading the ceria cubes (over rods and spheres) perform poorly for the water-gas-shift reaction in terms of activity and stability [115]. The rationale behind these results is still unclear as the atomic structure and active state of the polar (100) surface of ceria is not yet well understood [9, 116]. From an experimental point of view, polycrystalline materials are challenging to investigate compared to well-defined planar models, which are ideally suited to isolate the surface configurations and provide information about the elementary heterogeneous (gas-solid) reaction steps. Taking into account that ceria is mostly utilized in oxide supported metal catalysts [26], model systems in the form of thin epitaxial films on metal substrates are preferable, as these can provide information about the active properties of the oxide or metal and also the oxide–metal interface [117]. However, experimental strategies for the preparation of epitaxial, thermodynamically seemingly unfavorable $CeO_x(100)$ model systems are scarce and typically require complex preparation methods in separate chambers (i.e. pulse laser deposition) with concomitant exposure to ambient conditions prior to characterization or subsequent surface chemistry studies [10]. As a result, a large body of work has been devoted to the $CeO_x(111)$ surface [118, 119], which is easier to prepare on numerous metal surfaces in UHV compatible environments [120].

Whereas the preparation of (111) oriented cerium oxide is quite standard, the rich possibilities offered by oxide heteroepitaxy should also provide for means to manipulate the mechanisms governing the growth of binary and more complex oxides, eventually resulting in the realization of novel systems [121]. Particularly the oxygen chemical potential — an easily experimentally changeable thermodynamic variable — is rarely taken into consideration, but might have significant impact not only on the oxide composition and its surface reconstructions, but also by affecting surface mass transport or by influencing structural templating. Furthermore, stability of various phases and surface terminations typically differs with respect to oxygen chemical potential. Theoretical calculations consistently predict the (100) surface of ceria to be the least stable of the low index terminations [22, 23, 122], also above 0 K and in oxygen-rich conditions [123, 124]. Prompted by the emergence of the (100) orientation of ceria alongside (111) as recently reported on hexagonal metal surfaces without a readily apparent epitax-

ial relationship [9, 116, 125], we have explored the dynamics of the growth of ceria on Cu(111) to understand the $CeO_2(100)$ formation. Taking advantage of our *in situ* capabilities we demonstrate that the orientation of ceria can be controlled by adjusting the Ce/O ratio during growth. Using this facile method the optimized preparation leads to the exclusive growth of micrometer sized and several nanometers high, single phase $CeO_2(100)$ islands on Cu(111), while completely suppressing the nucleation of $CeO_2(111)$ islands. We further show the possibility of controlling the stoichiometry, and consequently the surface termination, of the $CeO_x(100)$ islands in the range of $2.0 \geq x \geq 1.5$, with average oxidation states of fully Ce^{4+} to fully Ce^{3+}. The $CeO_x(100)$/Cu(111) represents a well-defined and scalable model system suitable for benchmarking both structural and chemical studies, opening a pathway for novel structure-reactivity relationship studies of ceria based catalysts. Generalizing, our results indicate that increasing the oxygen chemical potential at the surface directly affects the growth of oxide nanostructures on metals, which can be exploited in the preparation of novel well defined metal-oxide heterostructures.

■ Methods

Experiments were carried out in a commercial Elmitec LEEM-III, providing a base pressure of 1×10^{-10} Torr. The LEEM instrument is equipped with a 5 μm, 1 μm and a 250 nm illumination aperture for micro-illumination. The Cu(111) crystal was cleaned by several standard sputter and annealing cycles. Cerium was evaporated from an e-beam source in oxygen ambient at 450 °C. Intermittent evaporation was done in a 20 s deposition 40 s stopped deposition mode in 3×10^{-6} Torr O_2 background pressure and in 20 s deposition 20 s stopped deposition mode in 1×10^{-5} Torr oxygen. Ceria was reduced by continuous Ce deposition onto the substrate at 450°C.

■ Results and Discussion

Employing the *in situ* capabilities of the LEEM instrument we investigated the growth of $CeO_2(100)$ on Cu(111) and the impact of oxygen chemical potential. To elucidate the mechanism of growth we first investigated the exposure of O_2 on Cu(111), the first phase of the preparation, followed then by the exposure of Cerium metal onto the Cu surface in an O_2 ambient. We will show that a high oxygen partial pressure increases massively the mobility of copper and oxygen atoms on the surface at 450 °C. At these conditions we will then examine the growth of ceria on oxygen covered Cu(111), demonstrating the influence of the oxygen-to-metal ratio on the resulting heterostructure and morphology of the growing ceria nanoparticles. Finally, we will characterize the nanoparticles in depth by microscopy and local electron diffraction (μ-LEED) highlighting the dependence of surface structure on oxygen partial pressure. We will also investigate the reducibility and emergent stable substoichiometric structures of $CeO_x(100)$ during reduction.

Structure and morphology of Cu(111) at elevated O_2 pressures

The LEEM sequence shown in Fig. 3.14 depicts the oxidation of the Cu(111)

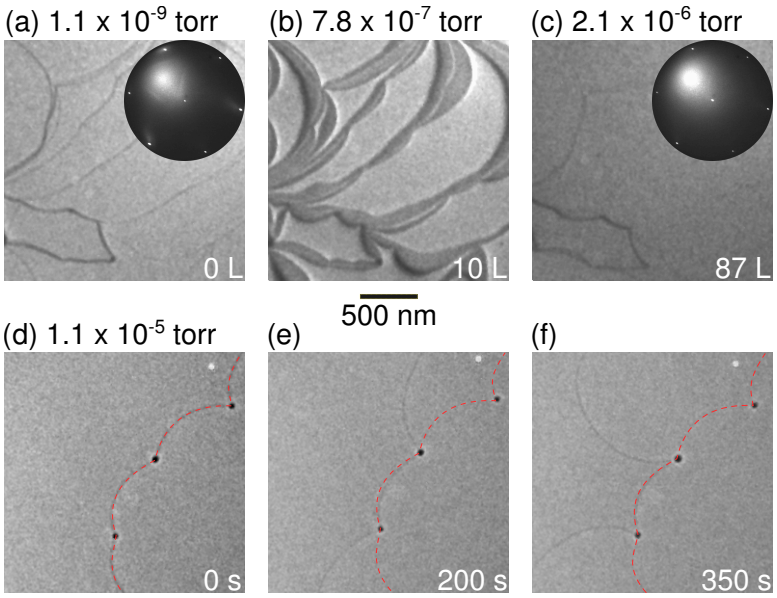

Figure 3.14: (a)-(c) LEEM time-lapse sequence of the oxidation of Cu(111) at 450 °C recorded at 2.4 eV. The lower contrast in the images is due to the lower reflectivity of the oxidized surface. Insets in (a) and (c) show corresponding LEED patterns obtained at 36 eV. The broad feature in the upper left region is due to inelastic electron scattering. (d)-(f) Movement of Cu(111) steps during further oxidation at 1.1×10^{-5} Torr and imaged at 1.8 eV. The same Cu step is highlighted by orange arrows.

surface at 450 °C. Starting from the step edges, the oxygen adsorbtion is visible after a dose of 3 L. Then, the oxygen spreads rapidly over the Cu(111) terraces, completely covering these after a dose of 87 L of O_2. There are several ordered structures of copper oxide reported in the literature [35, 125, 126], but surprisingly none are found after oxidation (cf. insets in Fig. 3.14a and Fig. 3.14c) at 450 °C. Only the intensity of the broad spot from the inelastic scattered electrons increases. Both facts indicate that the oxygen adsorbs onto Cu(111) in a disordered fashion, exhibiting high mobility at these conditions. We observe the crystallization of the known 44"- and 29"-structure and LEEM contrasts only at temperatures below 300 °C [119], whereas at 450 °C the LEED patterns indicate only a non-periodic arrangement of the Cu and O atoms at the surface. Further LEEM observations demonstrate a high degree of surface migration at elevated oxygen partial pressure. The LEEM sequence in Fig. 3.14d-f displays the movement of step edges on the surface at 450 °C and 1×10^{-5} Torr O_2 background pressure. In contrast, on the pristine Cu(111) surface or in O_2 pressures less than 1×10^{-6} Torr similar step movement is typically observed at temperatures significantly higher than 600 °C. Even though the reflectivity of the surface does not change anymore after the surface was completely covered by oxygen (cf. Fig. 3.14c) and thus indicating no further structural changes or oxidation, the increased oxygen partial pressure leads to an enhanced mobility of the atoms on the surface. Consequently, the ceria growth should be affected by the different conditions on the surface.

Growth of CeO_2/Cu(111)

Previous studies revealed that in conventionally used oxygen partial pressures of 5×10^{-7} Torr kinetic limitations strongly influence the morphology of the growing ceria island [34]. To study the dependence of oxygen partial pressure we have followed the growth process *in situ* by imaging the copper surface during Ce evaporation at a temperature of 450 °C enabling growth of ceria islands of a few hundred nanometers in size. LEEM images illustrating different stages of the growth in the conventionally used pressure regime of 5×10^{-7} Torr of O_2 at 450 °C are shown in Fig. 3.15a-c. Three distinct ceria phases are immediately recognizable by their shape after preparation (Fig. 3.15c) and can be identified individually using μ-LEED (see following section): triangularly shaped islands of $CeO_2(111)$ (bright at 5.2 eV), dendrite-like islands of $CeO_2(100)$ (dark at 5.2 eV), and needle-like ceria islands. Further observation showed that the needle-like islands act as a precursor for the growth of $CeO_2(111)$ islands. As such, the needles will be the subject of future studies.

The critical observation is that the $CeO_2(100)$ phase starts nucleating first (Fig. 3.15a) and is the only one present at the early stages of growth. This indicates that conditions at the onset of ceria nucleation favor the $CeO_2(100)$ phase. However, $CeO_2(111)$ phase is dominating at the later stages of growth (Fig. 3.15b-c). It has been previously suggested that the prerequisite for the nucleation of $CeO_2(100)$ on Cu(111) is a high degree of oxidation of the copper surface [125]. The need for oxygen at the interface is supported by a simple structural analysis showing that there are $\sim$ 14 O atoms per nm^2 in immediate contact with the substrate in the case of the $CeO_2(100)$ phase, in contrast to only $\sim$ 8 O atoms per nm^2 in the case of the $CeO_2(111)$ phase. While the exact atomistic details of ceria nucleation, and indeed of the nucleation of oxides in general, are not yet well understood, we postulate that the principal factor determining which ceria phase grows on the Cu(111) substrate is the ratio of adsorbed Ce and O atoms on the surface.

Before the Ce evaporation starts the Cu(111) surface is covered with adsorbed oxygen (cf. Fig. 3.14c), which is very mobile at the temperature used in this study as highlighted in the previous section. When Ce deposition commences, the formation of ceria islands decreases the amount of mobile, available oxygen at the surface. From our observation, it is clear that the oxygen partial pressure of 5×10^{-7} Torr is not enough to compensate for this "effective" loss of oxygen, and the equilibration of the Ce/O ratio on the surface results in conditions favoring the nucleation of $CeO_2(111)$. Therefore, the growth of $CeO_2(100)$ should require a high concentration of mobile oxygen at the surface at all times (see Fig. 3.16).

To test our hypothesis, we have adjusted the Ce/O ratio in favor of the oxygen by increase of O_2 pressure and intermittent Ce deposition. LEEM images illustrating this effect at O_2 partial pressures of 3×10^{-6} Torr and 1×10^{-5} Torr are shown in Fig. 3.15d-f and Fig. 3.15g-i, respectively. At 3×10^{-6} Torr O_2 partial pressure $CeO_2(100)$ oriented islands again nucleate immediately upon starting Ce deposition, but grow in a much more rectangular shape (see Fig. 3.16d-e). The nucleation of the $CeO_2(111)$ islands is further effectively delayed with respect to the growth at 5×10^{-7} Torr O_2 (cf. Fig. 3.16b-c and Fig. 3.16e-f). At 1×10^{-5} Torr O_2 partial pressure the nucleation of the $CeO_2(111)$ phase is completely suppressed (Fig. 3.15i). Furthermore, the increased oxygen pressure

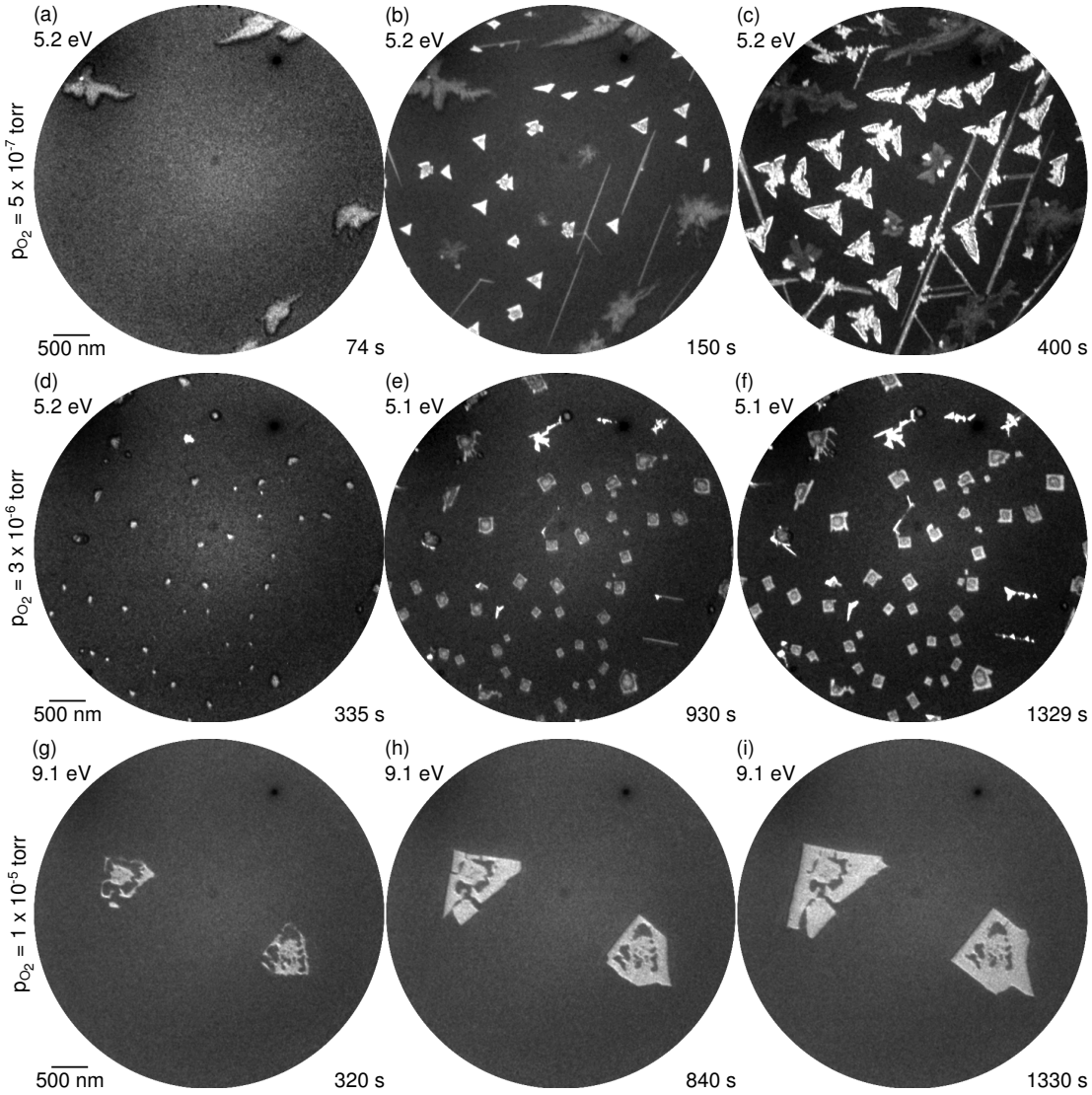

Figure 3.15: *In situ* ceria growth on Cu(111) at 450 °C in different oxygen background pressure and varied cerium flux: (a-c) 5×10^{-7} Torr and continuous cerium flux, (d-f) in 3×10^{-6} Torr with intermittent cerium flux, (g-k) in 1×10^{-5} Torr and also intermittent cerium flux. At low O_2 pressure (a-c), both $CeO_2(111)$ (bright) and $CeO_2(100)$ (dark) islands are observed; at high O_2 pressure, $CeO_2(100)$ islands grow exclusively.

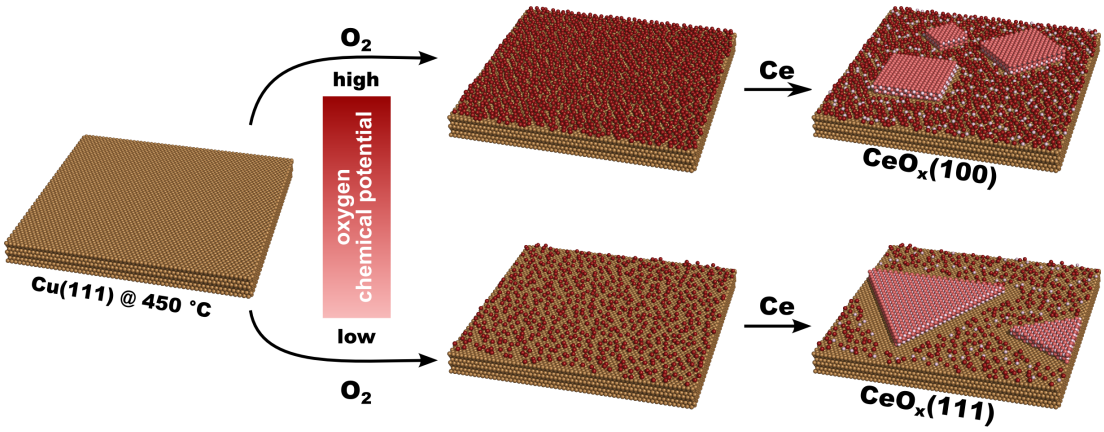

Figure 3.16: Schematic representation of the growth of ceria on Cu(111) depending on oxygen chemical potential.

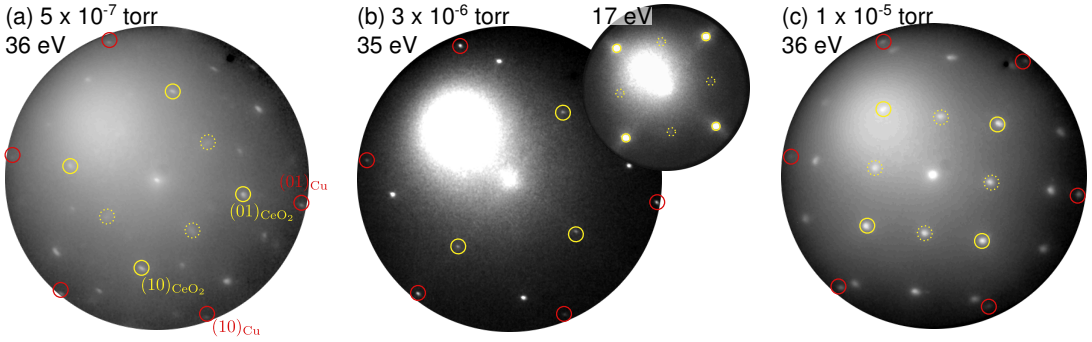

Figure 3.17: μ-LEED patterns recorded from $CeO_2(100)$ islands prepared in different conditions: (a) at 5×10^{-7} Torr oxygen partial pressure and continuous cerium flux, (b) at 3×10^{-6} Torr oxygen partial pressure and intermittent cerium flux, and (c) at 1×10^{-5} Torr oxygen partial pressure and intermittent cerium flux. Integer reflections from Cu(111) are highlighted by solid red circles; the integer and superstructure spots from $CeO_2(100)$ are indicated by solid and dashed yellow circles, respectively. All LEED patterns were recorded at elevated temperatures.

results in a much lower nucleation density of $CeO_2(100)$ islands. We attribute this effect on one hand to the lower defect density on the pristine Cu(111) surface (enabled by the high Cu and O mobility) and on the other hand to the increased mobility of Ce and O species, with the diffusion length being varied depending on the concentration of oxygen on the Cu(111) surface. It is conceivable that the nucleation mechanism places into contest the concurrent mobility and harvest of O between the CeO_2 island and the Cu(111) surface, essentially resulting in an oxygen rich or oxygen lean environment at the interface that leads to the growth of $CeO_2(100)$ or $CeO_2(111)$ phase, respectively.

Structural characterization of $CeO_2(100)$

Having established the preparation of $CeO_2(100)$ on Cu(111), we now proceed with the discussion of the structure—stoichiometry relationship of $CeO_2(100)$. Local electron diffraction (μ-LEED) patterns recorded from single $CeO_2(100)$ islands obtained with electron beam diameters of 250 nm or 1 μm are displayed

Pressure (10^{-6} Torr)	$a_{\parallel}^{(100)}$ (Å)	$a_{\parallel}^{(111)}$ (Å)
0.5	3.76	3.58
3	3.77	3.72
10	3.82	-

Table 3.5: In-plane lattice constants of the grown ceria islands (uncertainty ±0.05 Å). The surface lattice parameter is 3.83 Å for both CeO_2(111) and CeO_2(100).

in Figure 3.17. The (100) orientation of the ceria islands is easily identified in the LEED images by the square unit mesh. Moreover, the rectangular shaped islands grown at 3×10^{-6} Torr and 1×10^{-5} Torr are single crystalline whereas the more dendritic islands (cf. Fig. 3.16k) grown in 5×10^{-7} Torr are typically composed of several crystallites (see for example the two unit meshes rotated by 28° in Fig. 3.17a). Thus the higher Ce/O ratio enables not only a more regular morphology but also higher crystallinity. The in-plane lattice constants of the CeO_2(100) and the of the CeO_2(111) islands calculated using the Cu(111) reflections as reference are given in Tab. 3.5. In accordance with previous observations the CeO_2(111) lattice is compressed, whereas the CeO_2(100) islands grow at all used conditions without exhibiting any significant strain [101, 116].

Due to the alternation of positive Ce planes and negative O planes, the bulk termination of CeO_2(100) is a 'Tasker-type III' polar surface [127]. For the surface to be stable it has to compensate for the surface dipole moment. Accordingly, reconstruction of the surface may be expected, and we recognize two different surface reconstructions in the LEED patterns of the as-prepared islands depending on the oxygen partial pressure during growth. For the growth in the lower O_2 pressure regimes of 5×10^{-7} Torr and 3×10^{-6} Torr we observe a weak $c(2 \times 2)$ reconstruction (see Fig. 3.17a-b) whereas the islands grown in the high oxygen background of 1×10^{-5} Torr exhibit a $p(2 \times 2)$ reconstruction (see Fig. 3.17c). This difference in structure shows that the O_2 partial pressure is crucial for the emergence of the two CeO_2(100) reconstructions already observed in the literature [9, 116].

Reduction of CeO_2(100)

To study the structure-stoichiometry relationship in more detail, we have explored the $CeO_2 \leftrightarrow Ce_2O_3$ transition by employing Ce–ceria interfacial interaction [61]. Again, using the LEEM instrument, we have observed the structural transition in real-time by micro-illuminating individual CeO_2(100) islands (cf. Fig. 3.16i). During the initial Ce deposition, the spot intensities of the $p(2 \times 2)$ LEED pattern change, reflecting a modification of the atomic structure of the surface unit cell. After 12 min of Ce deposition all spots of the $p(2 \times 2)$ reconstruction have similar intensity. We propose a tentative interpretation based on the various structural models of the charge compensated (100) surface present in the literature [9, 116]. Specifically, it is possible to construct the $p(2 \times 2)$ reconstructed surface in either Ce or O terminated fashion [9], with distinct differences in the spot intensities. Assuming a more oxygen rich termination after preparation in 1×10^{-5} Torr O_2 partial pressure (Fig. 3.18a) the reducing conditions of Ce deposition lead to a low oxygen chemical potential. We therefore correlate the

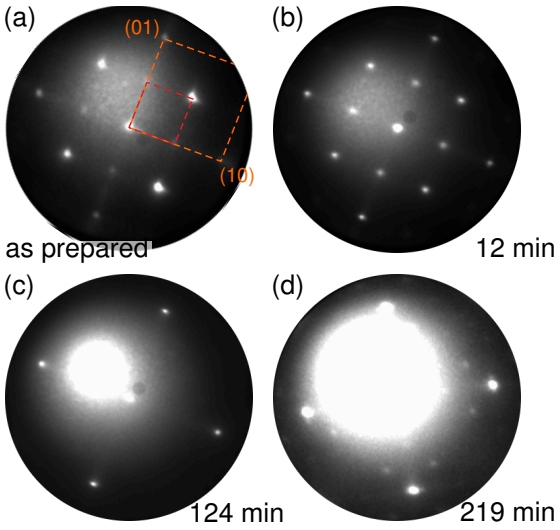

Figure 3.18: (a)-(d) LEED time-lapse sequence recorded at 17 eV electron energy of the reduction of the $CeO_2(100)$ islands by Ce deposition observed by μ-LEED of a single ceria (100) island. The orange dashed square and red dashed square in (a) highlight the $CeO_2(100)$ unit mesh and the $p(2 \times 2)$ reconstruction, respectively. The Cu(111) reflections are not visible because the Ewald's sphere is too small at 17 eV.

diffraction pattern shown in Fig. 3.18b with the Ce-terminated $p(2 \times 2)$ model, which has been calculated to be the most stable surface in vacuum [9].

With continued reduction, the $p(2 \times 2)$ superstructure spots vanish, leaving behind the (1×1) diffraction pattern (Fig. 3.18c). Finally the LEED patterns reveals a $c(4 \times 4)$ reconstruction (Fig. 3.18f) associated with the c-Ce_2O_3 (bixbyite) structure. Fig. 3.19a-b show LEED patterns of the $c(4 \times 4)$ reconstruction at 17 eV and 22 eV, respectively. Based on the model of the bulk terminated c-Ce_2O_3 structure shown in Fig. 3.19c, a $c(4 \times 4)$ superstructure is expected with respect to the $CeO_2(100)$ surface unit cell. Intriguingly, along the [1 1] direction in the LEED patterns in Fig. 3.19a-b only every fourth spot is observable (missing spots are indicated by blue dots in Fig. 3.19a). From the symmetry of the bulk terminated c-Ce_2O_3 unit cell we expect only every second spot to be

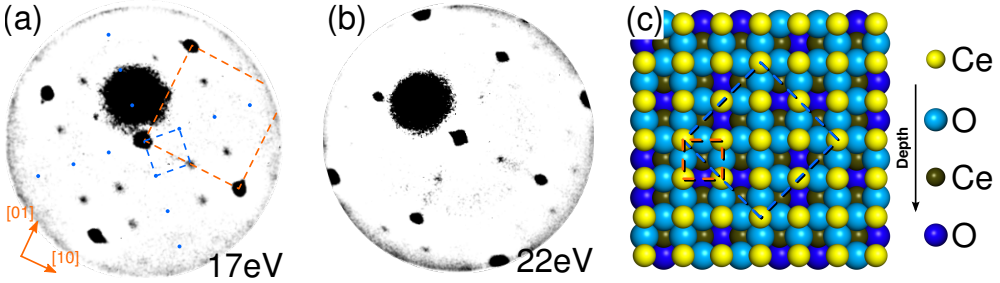

Figure 3.19: (a, b) LEED images that have been low-pass filtered to reduce the brightness of the inelastic background of the reduced CeO_x island. ^{SDS}*Increase blue dot size.* (c) Model of the bulk-terminated c-$Ce_2O_3(100)$ surface. The blue and red dashed squares indicate the $Ce_2O_3(100)$ and $CeO_2(100)$ surface unit cells, respectively.

absent due to mirror planes [128]. Since the (100) termination of bulk c-Ce_2O_3 is also a polar surface its structure should be modified by the charge compensation. The missing spots in the LEED pattern represent a valuable constraint for structural models of the charge compensated c-Ce_2O_3(100) surface. Specifically, the extinction of reflections indicates that there are two or more identical atoms or groups of atoms in the Ce_2O_3(100) surface unit cell [129], considerably reducing the number of models and structural variations that need to be considered in future calculations.

■ Conclusion

We have demonstrated the exclusive growth of the ceria(100) phase on the Cu(111) surface by controlling the oxygen chemical potential. Our *in situ* observations show that a high oxygen partial pressure increases the mobility of metal atoms on the Cu(111) surface, which is influencing the underlying growth kinetics. The exclusive growth of the ceria(100) phase represents an unexpected stability of the (100) phase with respect to the oxygen chemical potential, which challenges observations from previous theoretical calculations and which we have exploited in preparing a single-phase CeO_2(100)/Cu(111) model system. Furthermore, we showcase that the stoichiometry of the system can be controlled from CeO_2(100) to c-Ce_2O_3(100). This chemical reduction is directly linked to a structural transformation that is readily recognizable by a distinct $c(4 \times 4)$ surface reconstruction. This structure represents a unique realization of a well-ordered open ceria surface exposing exclusively the highly reactive Ce^{3+} ions. Our results present a viable approach to novel structural and chemical studies targeting the structure-activity relation in an catalytically relevant model system.

■ Acnowledgments

This work was supported by the U.S. Department of Energy, Office of Science, Office of Basic Energy Sciences, and Catalysis Science Program under contract No. DE-SC0012704. This work was also supported by the European COST Action CM1104, the Czech Science Foundation (GAČR 15-06759S), the Ministry of Education of the Czech Republic (LD13054) and the Grant Agency of Charles University in Prague (GAUK 794313).

3.4 Length-scale and preparation challenges in the utilization of model systems

Model systems are an established tool for isolation of structural features in physical chemistry. The clear advantage they provide in deconvolution of chemical processes over morphologically complex materials is indisputable. However, as with any other tool, one has to be mindful of their limitations. This is pertinent to the whole field of surface science, whose growth has reached a point where majority of published studies are comprised of multitechnique investigations. Obvious benefits of this development are accompanied by challenges associated with length-scale variation of data sets. Herein, the consequences of these challenges are discussed for the specific case of model systems used in physico-chemical studies.

Using state-of-the-art *in situ* characterization by time-resolved low-energy electron microscopy and photoelectron microscopy, the growth of cerium oxide on Cu(111) is followed. A significant structural and chemical heterogeneity at the microscale related to variance in preparation parameters and defects in the substrate is discovered, which can lead to an appreciable divergence from the model system premise. The fact that such heterogeneity can be easily missed both at the macroscale (e.g., by XPS) and atomic–nanoscale (e.g., by STM) has far-reaching consequences for the conjoined interpretation of area averaging and atomically resolved measurements. Considering the example of the (111) surface of cerium oxide, various discrepancies in the literature that can be related to the length-scale issue are discussed.

The findings emphasize that the control provided by the methodology explored in the previous sections is a double-edged sword. The rich variety accessible necessitates utmost precision of preparation parameters and attention to details, such as geometry of apparatuses, that are often glossed over. As sufficient precision is often not achievable, this imposes certain limits on conclusions that can be reached from the acquired data when discussing chemistry of explicit structural features. Here, it is appropriate to stress that the highlighted challenges are a part of a broader problem related to the funding of modern science being based on publication record. Specifically, the conclusions of published papers are often deliberately stretched to such extremes that they loose connection with the data reported, only to artificially achieve higher impact. The results reported in here serve as a remainder of the virtue of humility in science.

Exploiting micro–scale structural and chemical observations in real time for understanding chemical conversion: LEEM/PEEM studies over CeO_x–Cu(111)

Tomáš Duchoň[‡], Johanna Hackl[#], Jan Höcker[†], Kateřina Veltruská[‡], Vladimír Matolín[‡], Jens Falta[†§], Stefan Cramm[#], Slavomír Nemšák[#], Claus M. Schneider[#], Jan Ingo Flege[†], and Sanjaya D. Senanayake[¶]

[‡]Faculty of Mathematics and Physics, Department of Surface and Plasma Science, Charles University, V Holešovičkách 2, 18000 Prague 8, Czech Republic
[#]Peter Grünberg Institute (PGI-6), Forschungszentrum Jülich, 52425 Jülich, Germany
[†]Instiitute of Solid State Physics, University of Bremen, Otto-Hahn-Allee 1, 28359 Bremen, Germany
[§]MAPEX Center for Materials and Processess, University of Bremen, 28359 Bremen, Germany
[¶]Chemistry Department, Brookhaven National Laboratory, Upton, New York 11973, United States

Proper consideration of length-scales is critical for elucidating active sites/phases in heterogeneous catalysis, revealing chemical function of surfaces and identifying fundamental steps of chemical reactions. Using the example of ceria thin films deposited on the Cu(111) surface, we demonstrate the benefits of multi length-scale experimental framework for understanding chemical conversion. Specifically, exploiting the tunable sampling and spatial resolution of photoemission electron microscopy, we reveal crystal defect mediated structures of inhomogeneous copper–ceria mixed phase that grow during preparation of ceria/Cu(111) model systems. The density of the microsized structures is such that they are relevant to the chemistry, but unlikely to be found during investigation at the nanoscale or with atomic level investigations. Our findings highlight the importance of accessing micro-scale when considering chemical pathways over heteroepitaxially grown model systems.

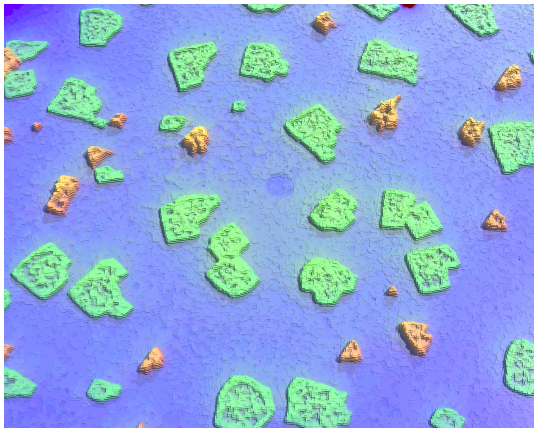

■ Introduction

Contemporary heterogeneous catalysis is taking advantage of a plethora of morphologically complex and often inhomogeneous materials enabled by advances in synthesis, fabrication and functionalization of nanostructures [130]. While these often provide superior performance, the rationale behind such improvements, including the atomic level active sites, is generally poorly understood. The primary obstacle of this is the inability to discriminate the fundamental steps of manifold chemical reactions proceeding over convoluted structural configurations of catalyst surfaces. A collective of processes prevail in chemical reactions, including rapid reactant activation or diffusion, intermediate formation, product desorption and mass transport over surfaces. Model systems, especially when prepared in the form of thin epitaxial films, can be used to reduce this complexity and isolate the individual configurations that may provide invaluable information about the elementary reaction steps and atomistic insight on active chemistry [5]. Systematic experimentation with models of compositional or redox/chemical state changes can be performed with nearly perfect reproducibility to make unbiased comparisons and establish principles for chemical reactivity or catalytic activity [97, 117]. A further benefit of this approach is the relative ease with which experimental data obtained from extended low-index surfaces can be coupled to theoretical calculations, most frequently performed using density functional theory [13].

However, the utilization of model systems typically comes with several assumptions one has to be mindful of. Specifically, the supposition that the model system and its behavior is truly representative of an ideal low index surface is a strong one, and especially so when the available chemical and structural data from the system do not share the same length scale, as is often the case. The most common methods used for chemical analysis average over areas in the order of mm to μm, while structural analysis that can support the above-mentioned assumption has to resolve features in the order of nm and less. Thus it is, for example, possible to carefully combine scanning tunneling microscopy with DFT [131], but conjoining the two with X-ray photoelectron spectroscopy can lead one to draw conclusions that may not correlate with spatial averaged structural and chemical information [132]. The length-scale challenge is schematically depicted in Fig. 3.20. In this letter, we will unravel the caveats of the model system approach by employing low energy electron microscopy and photoemission electron microscopy, techniques which allow characterizing the surface structure and chemistry on the same length-scale, in the study of ceria/Cu(111) model system, which has recently appeared in many physico-chemical studies [10].

■ Methods

Experiments were carried out in two separate LEEM instruments with a base pressure of 1×10^{-8} Pa: A commercial Elmitec LEEM-III and a FE-LEEM P90 instrument commercialized by SPECS. The FE-LEEM P90 is a permanent end station at the Research Center Jülich soft x-ray beamline UE56/1-SGM of the synchrotron facility BESSY II, Berlin, Germany, enabling the use of LEEM, μLEED and XAS-PEEM. Samples were prepared using identical growth proce-

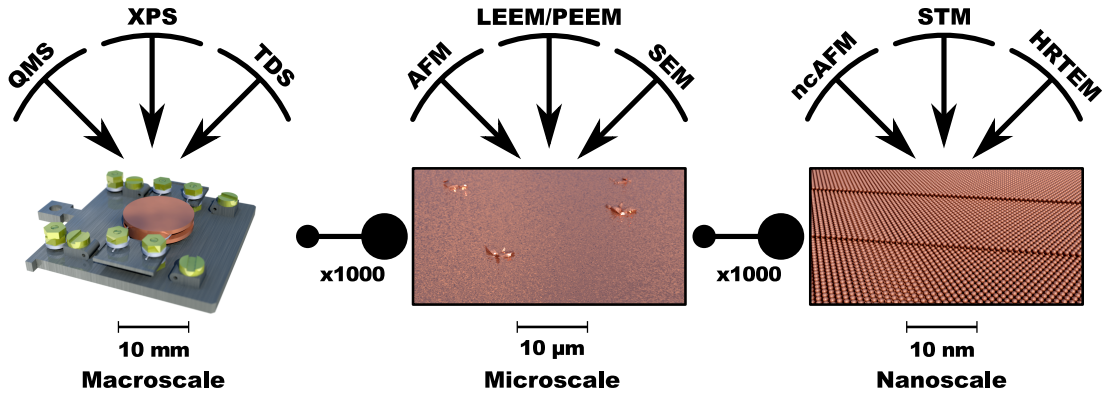

Figure 3.20: Schematic representation of the length-scale of various characterization techniques. The importance of the microscale information is highlighted by the possibility to miss relevant microsized structures on the surface.

dures in both instruments. The Cu(111) single crystals (MaTecK) were cleaned by several cycles of Ar^+ sputtering (1.5 keV) and annealing in vacuum at 600 °C. The cycles were interspaced by annealing in 5×10^{-5} Pa of oxygen at 600 °C, which has proved to be an effective way of forcing cerium atoms dissolved in the top part of the copper crystal (from prior ceria experiments) to the surface, where they can be more effectivelly cleaned by successive sputtering. Cerium was evaporated from an e-beam source in oxygen ambience (partial pressure ranging from 5×10^{-5} to 2×10^{-4} Pa) at 450 °C.

■ Results and Discussion

The ceria/Cu(111) system has been the focus of numerous chemical reactivity studies and has been extensively characterized by ISS, infrared spectroscopy (IR), XPS, LEED, STM, LEEM and modelled theoretically in the framework of DFT [10, 117, 133]. The growth of ceria on Cu(111) has been thought of as a simple diffusion limited process that results in the formation of CeO_x(111) epitaxial layers due to the nearly perfect 1.5 lattice coincidence with the substrate [31]. However, a recent discovery [116, 134] of the simultaneous nucleation of various ceria phases on the Cu(111) surface (see Fig. 3.21) has clearly shown the established principles of growth to be overly simplistic. Given that there is no general theory of oxides nucleation at the atomic scale, one has to carefully account for all the thermodynamic variables influencing the growth, most importantly the temperature and chemical potential of the present chemical elements and molecules. Specifically in the case of ceria/Cu(111), the surface oxygen chemical potential plays a decisive role in the formation of ceria layers exposing either the (111) or (100) surface [134]. This structural heterogeneity of models is likely to be a major influence to the subsequent titration of chemical reactivity and also catalytic activity.

While relevant thermodynamic parameters are provided in manuscripts, their variance can be considerable and confidence intervals are almost never investigated. This is especially important for the oxygen pressure used during the growth of ceria, which can vary, depending on the type of gauge used and the geometry of the experimental setup, by more than an order of magnitude. Furthermore, the

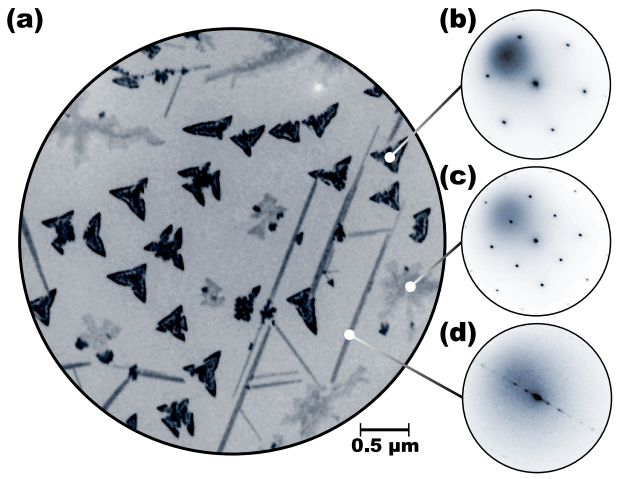

Figure 3.21: Various microscale phases of ceria growing on the Cu(111) surface at 450 °C in 5×10^{-7} Pa of O_2. (a) A 5 μm field of view LEEM image (E_p = 5.2 eV), local LEED patterns of (b) a triangular CeO_x(111) island (E_p = 36 eV), (c) a dendritic CeO_x(100) island (E_p = 36 eV) and (d) a needle-like ceria structure (E_p = 17 eV).

important parameter in ceria growth on Cu(111) is actually the surface oxygen chemical potential, which depends also on the Ce evaporation rate, a complex kinetic set of parameters. One can thus achieve conditions favorable to the nucleation of CeO_x(100) at the oxygen pressures typically used for preparation of CeO_x(111) by lowering the deposition rate and vice versa. Consequently, it is hard to transfer such an experiment from one apparatus to another. For example, inferring from an STM experiment conducted using one apparatus the morphology of a sample prepared in a different one is difficult, even with a very high degree of experimental controls. Specifically, it is very hard to disprove the existence of a minority phase (i.e., CeO_x(100) phase on a CeO_x(111)/Cu(111) sample) if such evidence cannot be observed by a conventional LEED apparatus. This in itself poses a major obstacle for the utilization of ceria/Cu(111) as a model system due to the chemistry of ceria being highly face and structure sensitive [11, 135]. The issue of phase heterogeneity is not limited to the ceria/Cu(111), but extends to other established ceria model systems, such as ceria/Ru(0001), too [136].

Furthermore, variations in chemistry observed as a result of the presence of defects in the surface of the model catalyst can also be important. The existence of microscopic defects, or even visible ones — such as scratches or dents, on the single crystal surface is often ignored but can be the locale for rich chemistry. The common practice of carefully repeating preparation recipes may, although helpful in other ways, have unwanted or unnoticed side effects, e.g., increases in defect or step density. While this is absolutely fine for highly local measurements where a defect-free area of the sample is carefully chosen for the analysis, area averaging measurements, such as XPS or activity measurements obtained from a reactor, may be strongly influenced by the history of the crystal. One important solution is to look for in situ methods where length-scales that are inclusive of large area effects in parallel with high resolution local area atomic probes, such as provided by LEEM/PEEM. Intensity–voltage LEEM exploits the material-specific variation of the specular reflectivity of low-energy electrons depending on kinetic energy

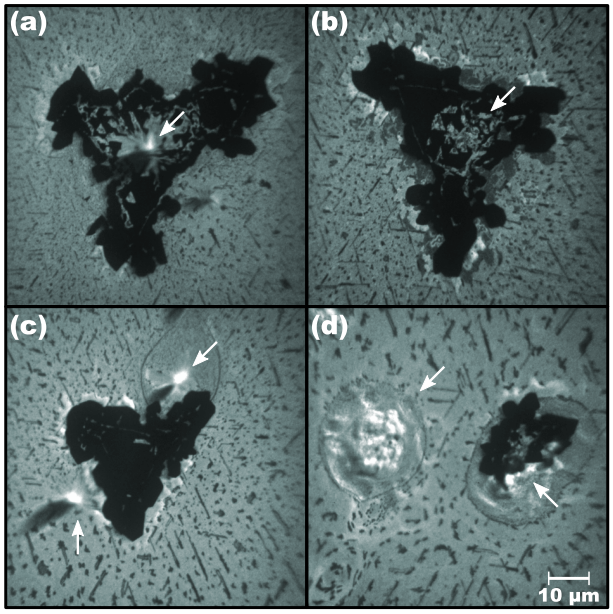

Figure 3.22: PEEM images of ceria related structures growing (a),(b) over, (c) around and (d) inside crystal defects in a Cu(111) single crystal during cerium evaporation in oxygen ambience at 450 °C. White arrows highlight the position of crystal defects. The smaller elongated objects are $CeO_x(100)$ islands growing along substrate steps. The images were acquired using a mercury-arc lamp as a source of photons.

[49], which owing to the underlying diffraction phenomena is largely determined by the local atomic structure of the sample. This way, I–V LEEM intrinsically provides mesoscale mappings representative of the local atomic structure with few nanometer and even temporal resolution (if dynamic I–V LEEM [49] is performed). However, the data is generally harder to interpret for complex structures of unknown chemical composition, suggesting the complementary use of (X-ray) PEEM in these cases.

Fig. 3.22 shows several examples of complex agglomerates growing at crystal defects in a Cu(111) single crystal during cerium evaporation in an oxygen background using PEEM. The lateral size of the structures shown in Fig. 3.22 can reach tens of micrometers, but the density depends highly on the quality of the single crystal surface. Based on the analysis of several single crystals from MaTecK, both brand new and a few years old ones, a 0.02–2 % of the surface area can be reasonably expected to be covered by the defect mediated structures, depending on the sample history. In order to gauge the significance of the seemingly low coverage we draw a comparison between the concentration of observed defects and step edges, as an example of catalytically relevant sites. A 1 % coverage equates to semi-infinite steps on vicinal surfaces separated by 20 nm or to steps on surfaces with average terrace area of 10000 nm^2. Step edges of comparable concentrations have been previously shown to markedly affect chemical reactions [109, 110, 137]. Furthermore, our estimate does not take into account the actual surface area of the structures and can considerably undervalue their effect. Consequently, while the complicated morphology and low density will make observation of regions of interest in STM quite unlikely, their contribution to signals

of area averaging techniques cannot be overlooked. Hence, the ability to observe such structures carefully in parallel with STM imaging is very important.

The approach to include multiple length-scales in the above example will enhance our understanding of the structure-reactivity relationship, while also allowing for a real-time observation of the chemical composition of the surface mediated structures. In addition, micro X-ray absorption spectroscopy (XAS) measurements can also reveal these structures to be an inhomogeneous, mixed Cu–O-Ce phase, with regions of varying ceria stoichiometry and copper content (see Fig. 3.23).

The measured Cu L_3 edge spectra (Fig. 3.23(b)) exhibit a two peak structure in the measured range, with maxima at 932.8 and 936.8 eV, characteristic for metallic copper. In fact, the spectra taken from regions A, C and D marked in Fig. 3.23(a) are practically identical to a reference spectrum of a clean copper single crystal (not shown). However, region B shows a prominent decrease of the second peak, which can be associated with the formation of copper oxide [138]. This could either mean that the copper is oxidized through a significant oxygen spillover from ceria, or that it forms a mixed oxide with ceria. We have mapped the loss of intensity of the second peak in real space by dividing a PEEM image taken at 932.8 eV by an image taken at 936.8 eV. The map shown in Fig. 3.23(c) reveals that the oxidized state is correlated with the defect mediated structure. Because we do not see oxidized copper around or below regular $CeO_x(100)$ and $CeO_x(111)$ islands even though oxygen is expected to be adsorbed on the surface in oxygen ambience in concentrations pertaining to the '29' and '44' Cu_xO structures [139, 140], this strongly suggests the formation of a copper–ceria mixed oxide in the defect mediated structures.

The analysis of measured Ce M_5 edge spectra (Fig. 3.23(b)) further supports this hypothesis. Because occupation of the highly localized f level dramatically changes the X-ray absorption fingerprint of Ce atoms, one can use fitting procedures to determine stoichiometry of ceria from of X-ray absorption spectra. A linear combination of referential Ce^{3+} and Ce^{4+} peaks [141] yields a stoichiometry of $CeO_{1.89\pm0.01}$, $CeO_{1.96\pm0.01}$, $CeO_{1.97\pm0.01}$ and $CeO_{1.80\pm0.01}$ for spectra from regions marked A, B, C and D in Fig. 3.23, respectively. While the spectra clearly illustrate the inhomegeneity of the defect mediated structure, a more significant finding is that the ceria retains its relatively high degree of reduction even in an oxygen ambient (5×10^{-7} Pa of O_2). This is consistent with the properties of a copper–ceria solid solution [142], which can, unlike pure ceria, preserve cerium atoms in a 3+ state even in oxygen ambient through electronic exchange with copper, i.e. by $Ce^{4+}+Cu^{1+} \rightarrow Ce^{3+}+Cu^{2+}$. It should be noted, that a lower concentration of oxygen vacancies, such as the one in region C, can be ascribed either to height variation of the structures or charge compensation of the polar $CeO_x(100)$ surface [9].

The presence of the mixed oxide on the surface can have a huge impact on the chemical processes proceeding over the ceria/Cu(111) model systems as copper–ceria is a well known catalyst utilized in several industrial processes, such as the water gas shift reaction [115, 143], preferential CO oxidation [144–146], methanol synthesis [117, 147], and others [6]. In fact, our observations can explain several inconsistencies between various ceria model systems that have been reported in the literature. An example that clearly illustrates the issue is the interaction

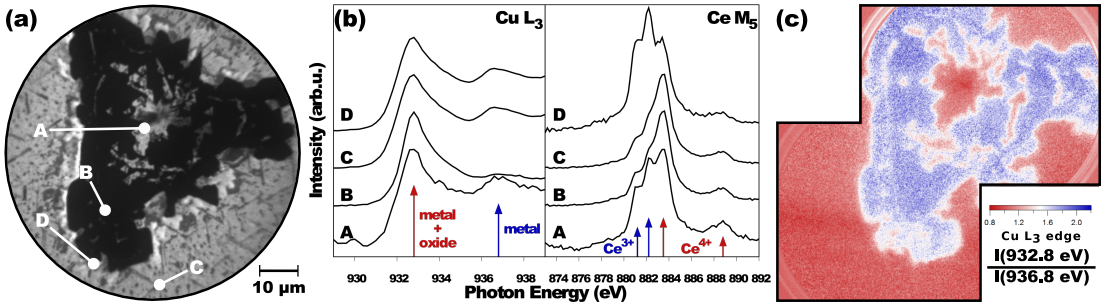

Figure 3.23: XAS analysis of a defect mediated structure. (a) A mercury-arc lamp PEEM image. (b) XAS spectra of the Cu L_3 edge and Ce M_5 edge collected from regions marked in (a). The red and blue arrows indicate features of specific chemical states. (c) Image map of the oxidation state of copper realized through a division of XAS-PEEM images collected at two characteristic energies of the Cu L_3 edge — 932.8 eV (oxide+metal) and 936.8 eV (metal).

of the (111) plane of ceria with water. Adsorbtion of water on reduced CeO_x was shown to lead to further reduction of the ceria surface in the case of reduced CeO_x(111)/Cu(111) [148] and oxidation of the ceria surface in the case of reduced CeO_x(111)/Ru(0001) [149]. Furthermore, reduced CeO_x(111)/Ru(0001) was reported to dissociate water, which lead to production of hydrogen at 600 K [150], but no such reaction was observed in the case of reduced CeO_x(111) on yttria-stabilized ZrO_2(111) [151]. Apart from the interaction with water, the ceria/Cu(111) model systems consistently exhibit a much richer chemistry in comparison with ceria/Ru(0001) model systems with respect to CO dissociation [152–154] and acetic acid decomposition [155, 156]. Taking into account that copper oxide plays an active role in the above-mentioned reactions [144], it is noteworthy that the effects related to the presence of the defect mediated structures will not be subdued by increasing the film thickness, which may otherwise mitigate support related effects that arise from the difference between thin films and bulk-like systems.

■ Conclusion

Our findings draw attention to the importance of new in situ methods to probe the dynamic nature of surface chemistry in model surfaces for the understanding of fundamental steps of catalyzed chemical reactions. The ability to observe reactions at multiple length-scales highlights the importance for providing structural and chemical data at the appropriate length-scale when discussing chemistry of explicit structural features. Especially apparent is also the fact that microscale information, which is often disregarded in the transition from macroscale to nanoscale, should weigh in more heavily when interpreting data from model systems.

■ Acknowledgements

This work was supported by the U.S. Department of Energy, Office of Science, Office of Basic Energy Sciences, and Catalysis Science Program under contract

No. DE-SC0012704. This work was also supported by the European COST Action CM1104, the Czech Science Foundation (GAČR 15-06759S) and the Grant Agency of Charles University in Prague (GAUK 472216).

3.5 Electron localization in ceria

Accurate description of ground state is fundamental for interpretation of various experimental techniques, prediction of physico-chemical properties, and, consequently, rational design of novel materials. Both theoretical and experimental approaches and their combination are, with great success, being employed in deduction of the ground state. However, with continuous advances in computational physics and instrumentation, previously accepted results are subjected to scrutiny and prone to change. An example of such a development in the past is the understanding of the bonding mechanism in MgO that shifted from a pure ionic [157, 158] to a more covalent picture [159, 160]. Similarly, the ground state of CeO_2 has been a controversial topic.

Principally, the whole issue boils down to the question of the occupation of the *4f* level in the ground state of CeO_2 and the nature of the respective *4f* electrons. In creating the CeO_2 molecule Ce atoms cede 4 electrons to the O atoms and change their nominal electron configuration from [Xe] $4f^1\ 5d^1\ 6s^2$ to [Xe] $4f^0$. The validity of the [Xe] $4f^0$ electron configuration of the ground state has been investigated by various experimental techniques. Notably, the presence of an empty $4f^1$ level has been demonstrated by bremsstrahlung isochromat spectroscopy (BIS) [161] and optical spectroscopy [162], leading to a covalent bonding picture in CeO_2 with an empty *4f* level. Contrary to these results, the ground state derived from interpretation of photoelectron spectroscopy experiments probing the Ce *3d* level is strongly mixed valent between $4f^0$ and $4f^1L$ (the L denoting a hole in the ligand) with a *4f* occupation of about 0.5 electrons [163]. Similar mixed valent configuration has been derived from resonant photoemission study of CeO_2 [164].

It has to be noted that the interpretation of photoemission spectroscopy (especially from the core levels) of strongly correlated materials (such as cerium oxide) is exceptionally difficult due to complex relaxation processes contributing to the final state of the photoemission process [165]. Specifically in the case of the Ce *3d* photoemission, the established interpretation is based on semiempirical Gunnarson-Schönhammer theory utilizing a single impurity Anderson hamiltonian [166], which is not adequate for the description of a possible *4f* coherent lattice in cerium oxide.

Herein, a novel approach to the issue of covalency in cerium oxide is presented by extending resonant photoelectron spectroscopy into angle resolved regime. This allows, in conjunction with density functional theory, to directly reveal covalent nature of *4f* admixture in the ground state of CeO_2. The results resolve a long-standing ambiguity of the ground state of CeO_2, update interpretation of resonant photoemission in cerium oxide, and offer important insights into core hole screening response in covalent compounds in general. The study represents a culmination of the research on heteroepitaxial growth of cerium oxide presented in the previous sections, which enabled this state-of-the-art investigation of electronic correlation effects relevant to reducible oxide chemistry by leveraging the isostructural transition between CeO_2 and Ce_2O_3.

Covalent versus localized nature of $4f$ electrons in ceria: resonant angle-resolved photoemission spectroscopy and density functional theory

Tomáš Duchoň[‡], Marie Aulická[‡], Eike F. Schwier[#], Hideaki Iwasawa[#], Chuanlin Zhao[§], Ye Xu[§], Kateřina Veltruská[‡], Kenya Shimada[#], and Vladimír Matolín[‡]

[‡]Faculty of Mathematics and Physics, Department of Surface and Plasma Science, Charles University, V Holešovičkách 2, 18000 Prague 8, Czech Republic
[#]Hiroshima Synchrotron Radiation Center, Hiroshima University, Higashi-Hiroshima, Hiroshima 839-0046, Japan
[§]Department of Chemical Engineering, Louisiana State University, Baton Rouge, Lousiana 70803, USA

We have conducted resonant angle-resolved photoemission spectroscopy of well defined $CeO_2(111)$ and c-$Ce_2O_3(111)$ model surfaces, revealing distinct f contributions in the valence band of the two compounds. In conjunction with density functional theory calculations, we show that the f contribution in CeO_2 is of a covalent nature, arising from hybridization with the O 2p bands. In contrast, c-Ce_2O_3 exhibits almost nondispersive f state at 1.3 eV, which is indicative of almost negligible c–f hybridization.

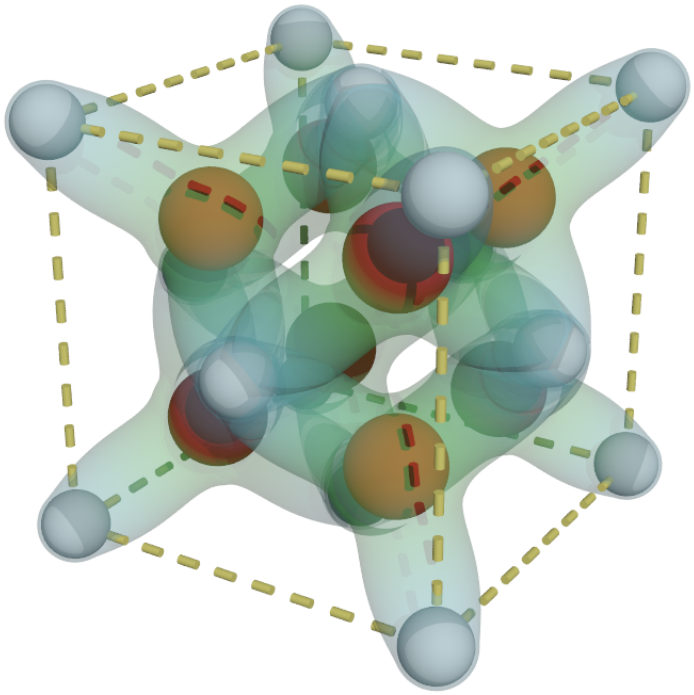

■ Introduction

The ground state of CeO_2 has been a controversial topic [161–164, 167–172]. The controversy involves the assignment of the nominally ionic CeO_2 to either a mixed valent or a covalent compound and arose partially due to the inability to distinguish these electronic configurations by core level photoelectron spectroscopy, namely that of the Ce *3d* level [172]. Strikingly, the ambiguity of the assignment is still prevalent in the scientific literature [173], sustained by a loose usage of the respective terms. By definition, mixed valent compounds contain cations in different oxidation states. The distinguishability of crystal sites occupied by the cations is related to the extent of the mixing between the two configurations (typically cation-cation mixing) [174]. This effectively leads to either highly unusual integral or non-integral mean oxidation state of the cation [175]. On the other hand, covalent compounds contain only one type of cation sites and exhibit non-integral valence as a consequence of hybridization (typically cation-anion mixing) [176]. In the case of ceria, where there are no crystallographically distinguishable cerium sites in the lattice, the fundamental difference between the two configurations lies in the character of the occupied states. The homogeneous mixed valent ground state would feature a partial occupation of the highly localized atomic-like Ce *4f* level [177] through valence fluctuation, while the covalent ground state would exhibit an empty Ce *4f* level with the bonding electrons spin-paired with the ligand (specifically the closed O *2p* shell) [176]. The two configurations would manifest a different response to electronic perturbations, such as a core hole, an oxygen vacancy, foreign interstitial or substitutional species, adsorbates or electronic potential in an electrochemical device. The importance of understanding behaviour of the electrons in ceria due to said perturbations is highlighted by recent studies showing gaps in understanding the bonding mechanism and reactivity of ceria [20] and metal oxides in general [8].

Notably, the established mixed valent interpretation of core-level photoemission from ceria[163], based on semiempirical Gunnarson-Schönhammer theory utilizing single impurity Anderson hamiltonian, has been called into question. Rigorously calculated configuration interaction wavefunctions for CeO_2 and Ce_2O_3 were used to provide ab initio theoretical description of core-level photoemission accounting for many-body effects [178–180]. The results show that experimental spectra can be modeled through covalent interaction, revealing possible error in the former approach.

Motivated by the above-mentioned controversy and the unsatisfactory understanding of photoemission in ceria in general, we herein present the results of a combined angle-resolved photoemission spectroscopy (ARPES) and density functional theory study of the *4f* electrons in ceria. Leveraging recent advances in *in situ* preparation of well-defined ceria model surfaces, we directly compare CeO_2, a nominal $4f^0$ compound, and c-Ce_2O_3, a nominal $4f^1$ compound, and reveal the covalent nature of the *4f* admixture into the O *2p* valence band in CeO_2 in contrast to the highly localized *4f* electrons in c-Ce_2O_3. As a consequence, we show that the resonant photoemission enhancement at the $4d \rightarrow 4f$ absorption threshold in CeO_2 does not originate from the occupation of localized *4f* states on Ce atoms in the ground state, but arises from the covalent character of the O *2p* valence band through interatomic effects.

■ Methods

ARPES measurements were performed with 110-130 eV p-polarized photons on the linear undulator beamline BL-1 at the Hiroshima Synchrotron Radiation Center (HiSOR) in Hiroshima University. The energy and momentum resolution was set at 30 meV and 0.015 $Å^{-1}$, respectively. The experiments were carried out with the sample cooled down to 12 K. Highly ordered epitaxial ceria films exposing the (111) surface of the fluorite lattice were prepared by reactive evaporation of Ce onto Cu(111) single crystal in 5×10^{-5} Pa of O_2 at substrate temperature of 250 °C in the preparation chamber connected to the ARPES chamber. The films were around 3 nm thick, which is enough to guarantee continuity and mitigation of possible size effects [1, 164] while still being thin enough to avoid charging during measurements. The stoichiometry of the prepared layers was carefully controlled using Ce-ceria interfacial reaction [61]. The preparation procedure has been described in detail in [1]. Briefly, metallic Ce is deposited onto ceria surface and the sample is heated to 600 °C. The elevated temperature allows oxygen to diffuse through the ceria lattice to the Ce metal overlayer, which then oxidizes and adopts the fluorite structure of the underlying ceria. Spin-polarized DFT calculations based on the Heyd-Scuseria-Ernzerhof (HSE06) [181] hybrid functional were carried out using the projected augmented wave (PAW) method as implemented in the VASP (version 5.3) [182, 183]. The (*4f*, *5s*, *5p*, *5d*, *6s*) states of Ce and (*2s*, *2p*) states of O were treated as valence states and expanded using a plane-wave basis set up to 400 eV. For bulk CeO_2, the lattice constant was optimized on a (11×11×11) Monkhorst-Pack k-point grid to be 5.40 Å, and the O *2p*–Ce *4f* band gap was calculated to be 3.5 eV, both in close agreement with previous experimental (5.41 Å [184] and 3 eV [161]) and HSE06 results (5.41 Å and 3.3 eV [185]). The equilibrium lattice constant of the c-Ce_2O_3 (bixbyite) was calculated to be 11.20 Å (vs. experimental value of 11.16 Å [186]) with all atoms in the bulk unit cell fully relaxed to below 0.03 eV/Å and the k-space sampled at the Γ-point only. The antiferromagnetic state was used although it was only marginally more stable than the ferromagnetic state. Electronic structures were calculated on a (3×3×3) Monkhorst-Pack k-point grid using the frozen optimized bulk structure. The Ce *4f*-*5d* band gap was calculated to be 2.3 eV (vs. experimental value of 2.5 eV [187]). Core level electron excitation (*4d*→*4f*) was done using the method of Köhler and Kresse [188] and was applied to all Ce atoms in CeO_2 and c-Ce_2O_3. The bulk oxidation energy for c-Ce_2O_3 + $\frac{1}{2}O_2 \rightarrow 2CeO_2$ was calculated to be -3.12 eV, with available estimates falling between -3.5 and -4.0 eV at ambient temperature [26, 75].

■ Results and Discussion

In order to elucidate the nature of the ground state of CeO_2 we use c-Ce_2O_3 as a reference $4f^1$ compound [61]. The advantage of this approach over other prototypical $4f^1$ compounds that have been previously used for the purpose, such as CeF_3 [169], is that we minimize the influence of structural and chemical variation on the electronic configuration. The Ce sublattice in both CeO_2 and c-Ce_2O_3 is practically identical, the only difference being ordered oxygen vacancies

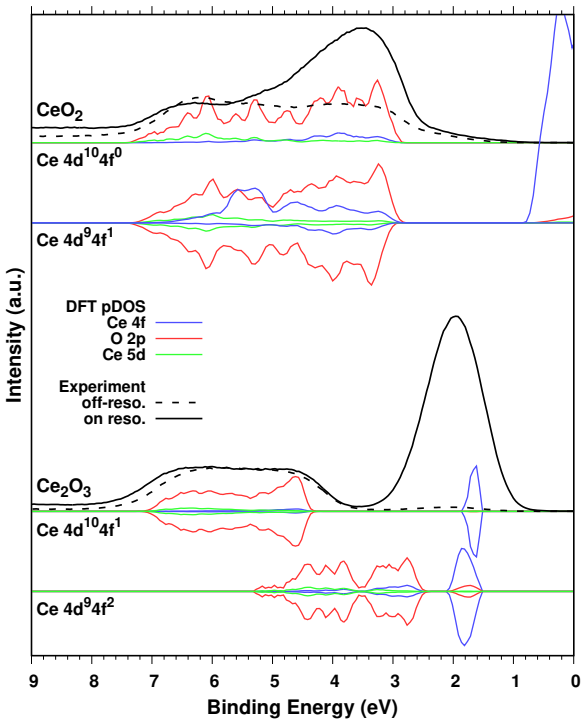

Figure 3.24: (color online). Partial density of states (pDOS) of CeO_2 and c-Ce_2O_3 as calculated from HSE06 exchange-correlation functional and measured by photoelectron spectroscopy (PES). The pDOS has been calculated for the ground state of CeO_2 and c-Ce_2O_3 and for an intermediate state with a Ce $4d$ electron excited into the Ce $4f$ level. The PES spectra are shown as measured off (dashed black lines, $h\nu = 115$ eV) and on (solid black lines, $h\nu = 125$ and 121 eV for CeO_2 and c-Ce_2O_3, respectively) the Ce $4d \rightarrow 4f$ resonance. The calculated DOS is shifted to coincide with the experimental data (the actual Fermi energy of the DOS plots in the figure is at 2.9 and 1.55 eV for CeO_2 and c-Ce_2O_3, respectively. The Ce_2O_3 pDOS has been scaled down by a factor of 32 to account for higher amount of Ce atoms in the unit cell in comparison with CeO_2.

in the O sublattice in c-Ce_2O_3 [25]. Moreover, we can exploit the isostructural $CeO_2 \leftrightarrow$c-Ce_2O_3 transition and use one sample for both systems, further reducing the extrinsic contributions to our experimental results [1].

Resonant photoemission is a commonly used tool for enhancing the intensity of photoemission features originating from states with low density and for gauging hybridization strength in correlated electron systems, especially the *c–f* hybridization of cerium compounds [189]. Particularly in ceria, the $4d \rightarrow 4f$ resonant transition is routinely used to reveal the occupation of the *4f* state, a fingerprint of Ce^{3+} [93]. However, both CeO_2 and c-Ce_2O_3 exhibit a resonant enhancement at the $4d \rightarrow 4f$ photoabsorption threshold (125 and 121 eV for CeO_2 and c-Ce_2O_3, respectively), albeit with different characters. The resonant feature in c-Ce_2O_3 directly overlaps the direct photoemission *4f* peak and has comparable width, while the resonant feature in CeO_2 overlaps the top of the O *2p* band and is noticeably wider than the *4f* photoemission peak in c-Ce_2O_3. The valence band photoemission spectra showing the resonant enhancement at the $4d \rightarrow 4f$ photoabsorption threshold for CeO_2 and c-Ce_2O_3 are shown in Fig. 3.24.

The resonant enhancement in c-Ce_2O_3 can be explained by constructive interference of the direct photoemission from the *4f* level with an indirect super Coster-Kronig decay of an intermediate $4d^9 4f^2$ state :

$$4d^{10}4f^1 + h\nu \rightarrow 4d^9 4f^2 \rightarrow 4d^{10}4f^0 + e^-,$$

where $h\nu$ and e^- stand for an incident photon and a photoelectron, respectively. To interpret the resonant enhancement in CeO_2 using the same arguments one would have to start from an initial configuration with one electron in the *4f* level — a $4d^{10}4f^1\underline{L}$ state. This would make CeO_2 essentially a $4f^1$ compound in the case of the covalent ground state. Consequently, the assumption of the $4d^{10}4f^1L$ initial state inevitably leads to the homogeneous mixed valent ground state of CeO_2 with a partial occupation of the *4f* level through mixing between $4f^0$ and $4f^1L$ configurations defined by the integer *4f* occupation number. However, this description is based on the assumed resonant enhancement process at the $4d \rightarrow 4f$ photoabsorption threshold in CeO_2 involving the ground state of the $4f^1L$ configuration, which is not self-evident. Specifically, the extent of final state effects in the resonant photoemission process has not been previously accounted for.

While the occupation of the localized (atomic-like) *4f* level in the homogeneous mixed valent ground state of ceria is expected to generate a dispersionless photoemission feature, the *p*-bonding mediated itinerant nature of extended covalent states (of *4f* and *2p* symmetry) would give rise to an observable dispersion in ARPES. In order to examine these effects we have followed the dispersions at the on-resonance for CeO_2 and c-Ce_2O_3 along the $\bar{M}$-$\bar{\Gamma}$-$\bar{M}$ direction (in surface Brillouin zone notation).

Figs. 3.25(b) and 3.25(c) show the on-resonance ARPES image plots for CeO_2 and c-Ce_2O_3, respectively. Compared with the off-resonance ARPES image plot for CeO_2 shown in Fig. 3.25(a), the dispersive features at the binding energy of 3–6 eV are clearly observable. Note that in Fig. 3.25(b) Ce *4f* derived spectral intensity is much enhanced at the binding energy of 3–4 eV where O *2p* states exist, indicating covalent hybridization between Ce *4f* and O *2p*. On the other hand, the *4f* derived spectral feature in c-Ce_2O_3 at the binding energy of 1.9

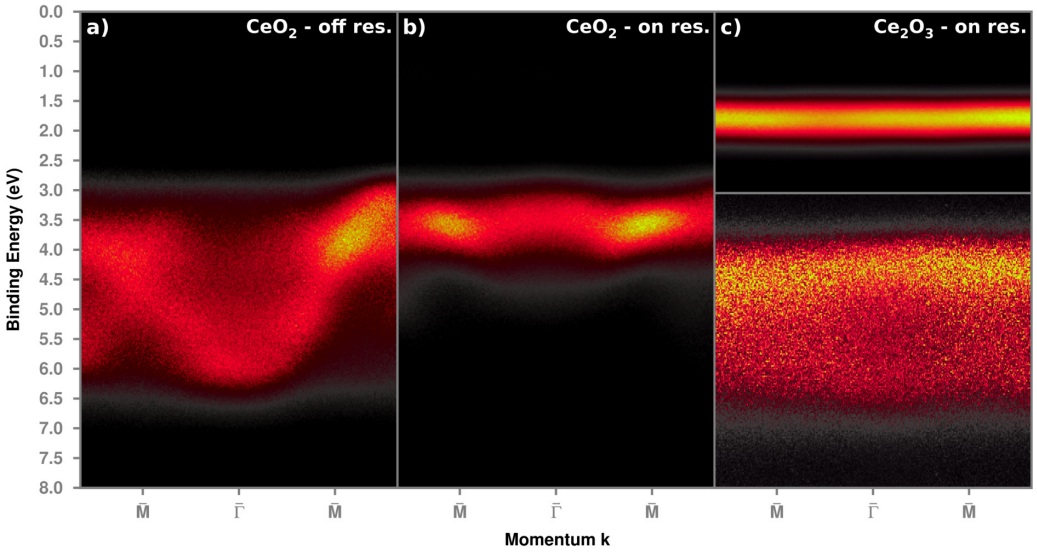

Figure 3.25: (color online). Dispersion of the valence band in CeO_2 and c-Ce_2O_3 in $\bar{M}$-$\bar{\Gamma}$-$\bar{M}$ direction of the surface Brillouin zone followed by resonant angle resolved photoelectron spectroscopy. a) Valence band of CeO_2 ($h\nu$ = 115 eV), b) and c) dispersion of the resonant feature at the $4d \rightarrow 4f$ photoabsorption threshold in CeO_2 ($h\nu$ = 125 eV) and c-Ce_2O_3 ($h\nu$ = 121 eV), respectively. The areas of the energy dispersive curves were normalized to 1 prior to plotting the maps. The bottom and upper part of c) were normalized separately in order to highlight the O *2p* bands.

eV exhibits no discernible dispersion within the experimental resolution (Fig. 3.25(c)). These results indicate different resonant photoemission process in the two compounds: more specifically, there is no occupation of atomic-like localized f states in the ground state of CeO_2.

In order to further ascertain the covalent hybridization in the valence band of ceria we have calculated electronic properties in the intermediate states ($4d^9 4f^1$ for CeO_2 and $4d^9 4f^2$ for c-Ce_2O_3). The density of states plots are shown in Fig. 3.24. We find, in agreement with previous DFT studies [190], that the O *2p* band in the ground state of CeO_2 has a small *4f* and *5d* admixture at the top and the bottom of the band, respectively. However, this alone cannot be used to abandon the pure ionic bonding picture in ceria (originating from the nominal electron configuration) as the degree of the mixing in the calculated partial density of states is comparable to other recognized ionic compounds, such as the NaCl [191]. On the other hand, the intermediate state shows an appreciable increase in the *4f* admixture into the O *2p* band, to such an extent that the valence band looks covalent in character. It should be noted that the major increase of the f contribution around 5-6 eV is related to the excited f electron of the intermediate state, which will be further discussed below. This behaviour is consistent with closed shell screening of the *4d* core hole by covalent electrons [192]. Appropriately, the response of O *2p* electrons to a *4d* core hole in c-Ce_2O_3 is less significant due to the occupation of the highly localized *4f* level by two electrons, which can effectively screen the positive charge of the core hole. An interesting aspect of the intermediate $4d^9 4f^1$ state of CeO_2 is that there is no

observable gap between the O *2p* pDOS and the *4f* pDOS at the fermi level (Fig. 3.24).

We examine band structure calculations along X-Γ-L (in bulk Brillouin zone notation), straight line close to the experimental setup, for the ground state and the intermediate state of CeO_2 (Fig. 3.26(a)). Apart from lifting of degeneracy of the *2p* bands, it can be seen that as a consequence of the point charge of the core hole the additional band of the intermediate state appears at 5 eV at Γ, directly overlapping the O *2p* level. It is noteworthy, that the excited electron does not occupy highly localized *4f* states, but a considerably hybridized one with O *2p* character.

In order to further ascertain the covalent hybridization in the valence band of ceria we have calculated electronic properties in the intermediate states ($4d^9 4f^1$ for CeO_2 and $4d^9 4f^2$ for c-Ce_2O_3). The density of states plots are shown in Fig. 3.24. We find, in agreement with previous DFT studies [190], that the O *2p* band in the ground state of CeO_2 has a small *4f* and *5d* admixture at the top and the bottom of the band, respectively. However, this alone cannot be used to abandon the pure ionic bonding picture in ceria (originating from the nominal electron configuration) as the degree of the mixing in the calculated partial density of states is comparable to other recognized ionic compounds, such as the NaCl [191]. On the other hand, the intermediate state shows an appreciable increase in the *4f* admixture into the O *2p* band, to such an extent that the valence band looks covalent in character. It should be noted that the major increase of the *f* contribution around 5-6 eV is related to the excited *f* electron of the intermediate state, which will be further discussed below. This behaviour is consistent with closed shell screening of the *4d* core hole by covalent electrons [192]. Appropriately, the response of O *2p* electrons to a *4d* core hole in c-Ce_2O_3 is less significant due to the occupation of the highly localized *4f* level by two electrons, which can effectively screen the positive charge of the core hole. An interesting aspect of the intermediate $4d^9 4f^1$ state of CeO_2 is that there is no observable gap between the O *2p* pDOS and the *4f* pDOS at the fermi level (Fig. 3.24).

We examine band structure calculations along X-Γ-L (in bulk Brillouin zone notation), straight line close to the experimental setup, for the ground state and the intermediate state of CeO_2 (Fig. 3.26(a)). Apart from lifting of degeneracy of the *2p* bands, it can be seen that as a consequence of the point charge of the core hole the additional band of the intermediate state appears at 5 eV at Γ, directly overlapping the O *2p* level. It is noteworthy, that the excited electron does not occupy highly localized *4f* states, but a considerably hybridized one with O *2p* character.

$$
\begin{aligned}
&(1)\ \text{Ce}\ 4d^{10}4f^{0}\ \text{O}\ 2p^{6} + h\nu \rightarrow\ \text{Ce}\ 4d^{10}4f^{0}\ \text{O}\ 2p^{5} + e^{-},\\
&(2)\ \text{Ce}\ 4d^{10}4f^{0}\ \text{O}\ 2p^{6} + h\nu \rightarrow\ \text{Ce}\ 4d^{9}4f^{1}\ \text{O}\ 2p^{6} \rightarrow\\
&\qquad\qquad\qquad\qquad\qquad\rightarrow\ \text{Ce}\ 4d^{10}4f^{0}\ \text{O}\ 2p^{5} + e^{-}.
\end{aligned}
$$

Now it is clear that the resonance enhancement at the *4d*→*4f* threshold for Ce^{4+} and Ce^{3+} atoms is of profoundly different nature. Since the resonant enhancement of the *f* derived spectral feature from Ce^{4+} atoms is caused by interatomic effects, it is likely to be sensitive to perturbations such as oxygen vacancies,

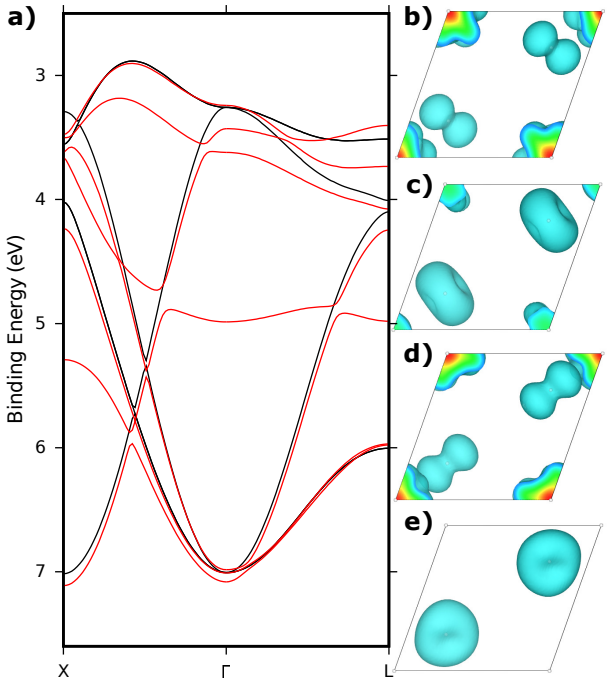

Figure 3.26: (color online). a) Band structure of CeO_2 calculated along X-Γ-L for the ground state (black) and the intermediate $4d^9 4f^1$ state (red). The extra $4f^1$ band of the intermediate state is at 5 eV at Γ. The calculated band structure has been shifted by 2.9 eV to coincide with the experimental data. Calculated Kohn-Sham wave functions at Γ-point of CeO_2 in the intermediate state are shown as cyan contours (corresponding to probability density of 2^{-5}; higher probability densities are shown in warmer colors as visible in cutout areas) in b) - the topmost O *2p* band, c) the second O *2p* band (the third has the same symmetry and is not shown), d) $4f^1$, e) - representative of the bottom three O *2p* bands. There are four cerium atoms and two oxygen atoms in the corners and in the middle of the displayed cut through the CeO_2 lattice, respectively. Periodic portions of the wave functions have been eliminated for clarity.

adsorbates, foreign substitutional, interstitial species, etc. On the other hand, the resonant process for Ce^{3+} atoms is less influenced by the perturbations because it is an intraatomic transition. This requires reexamination of the widely used formula for derivation of stoichiometry of various ceria-based materials from the ratio of resonant enhancement of Ce^{4+} and Ce^{3+} photoemission [12, 193–196]. Given the widespread use of the method, the observation of the interatomic effects in the resonance photoemission in ceria calls for a further study evaluating the validity of the direct proportion between the intensity of the resonant feature and the density of Ce^{4+} atoms with respect to the electronic perturbations in their vicinity.

■ Conclusion

We have presented the results of a combined experimental and theoretical study of the electronic structure of CeO_2. We find that there are no occupied localized f states in the ground state of CeO_2. Instead, we demonstrate that the f

contribution in CeO_2 is of a covalent nature, arising from hybridization with the O *2p* bands.This is in contrast to the nondispersive *4f* state at 1.9 eV in c-Ce_2O_3, where the O *2p* bands shifts to higher binding energy, reducing mixing with the *4f* states at the top. We show that, as a consequence of the covalent hybridization, the resonant photoemission process in CeO_2 involves interatomic core-hole screening, which is in contrast to the intraatomic process in Ce_2O_3. We suggest that the different nature of the two processes should be taken into account when interpreting resonant photoemission experiments from ceria and other covalent materials.

■ Acknowledgments

This work was supported by the Grant Agency of Charles University in Prague (GAUK 472216), the Czech Science Foundation (GAČR 15-06759S), Hiroshima Synchrotron Radiation Center (13-B-12) and Louisiana EPSCoR Program. The computing resources used in the project were provided by LSU-HPC, ORNL, and NERSC. E.F.S acknowledges financial support from the JSPS postdoctoral fellowship for overseas researchers as well as the Alexander von Humboldt Foundation (Grant No. P13783).

4. Summary

The thesis was focused on providing fundamental insights into structural and electronic properties of cerium oxide pertinent to its utilization in heterogeneous catalysis. The subject has been studied in the framework of model system approach employing state-of-the-art instrumentation available both at the Surface Physics group of the Department of Surface and Plasma Science at Charles University in Prague and at foreign laboratories. The studies presented in the thesis were published in peer-reviewed journals and gathered attention of the international scientific community (40 citations as of May 2017). The most important results are summarized below.

Ce–ceria interfacial interaction was employed in a rigorous study of oxygen vacancy ordering in cerium oxide. The method facilitated precise control of stoichiometry, which enabled stabilization of equilibrated phases of oxygen vacancies with long-range ordering. The ordered phases were characterized by a combination of surface analysis techniques, revealing a distinct symmetry with respect to the $CeO_2(111)$-(1×1) surface — $Ce_7O_12(111)$-$(\sqrt{7} \times \sqrt{7})R19.1°$, $Ce_5O_{10}(111)$-(3×3) and $Ce_2O_3(111)$-(4×4) — and a gradient of oxygen vacancies towards the surface. Importantly, the cerium sublattice stays essentially unperturbed throughout the transition from CeO_2 to Ce_2O_3 under these conditions. The oxygen vacancy co-ordination represents a new degree of freedom that can be exploited in advanced model cerium oxide catalysis. The results were also shown to be independent on the substrate used provided it is a metal.

Time-resolved *in situ* investigation of the effect of oxygen chemical potential at the surface of a metal single crystal on heteroepitaxial growth of cerium oxide was carried out. The real-time observation revealed unexpected variety in shape and structure of growing cerium oxide islands accessible through adjustment of the oxygen chemical potential. This enabled stabilization of energetically less favorable surface terminations of cerium oxide, specifically the $CeO_x(100)$. Flexibility of the methodology allowed for a first-of-a-kind direct comparison of different surface terminations of cerium oxide under identical conditions. This has been utilized in continuation of the oxygen vacancy ordering study, leading to the first observation of the fluorite $Ce_2O_3(100)$ surface exhibiting a $c(2 \times 2)$ reconstruction with respect to the $CeO_2(100)$ surface. The results also provide further insights into fundamental processes at play in heteroepitaxial growth of oxides in general.

The extraordinary control provided by the methodology developed heretofore emphasizes complexity of the reducible oxides growth. Making use of analysis at the microscale, considerable structural and chemical heterogeneity of cerium oxide model systems related to careless preparation procedures was exposed. The discovery has far-reaching consequences for interpretation of multitechnique investigations at diverging length-scales, which was illustrated by conflicting conclusions in contemporary literature on model cerium oxide systems. Specifically, the necessity for providing structural and chemical data at the same length-scale when discussing chemistry of explicit structural features was highlighted, as well as the importance of microscale characterization, that is often skipped when transitioning from macro- to nanoscale.

The knowledge accumulated during the above-mentioned studies culminated in a unique investigation of electronic structure of cerium oxide. For the first time it was possible to follow band dispersion of cerium oxide throughout isostructural CeO_2 to Ce_2O_3 transition. The results unambiguously established covalent hybridization in the ground state of CeO_2 and revised decades-old interpretation of photoemission from cerium oxide. The investigation also offered important insights into screening response to electronic perturbations, such as a core hole, in covalently bonded metal oxides in general.

The results of the thesis represent a significant advancement in understanding of electronic and structural properties of cerium oxide relevant to its ubiquitous utilization in heterogeneous catalysis. The model framework refined in the thesis allows for unprecedented control over the structure of cerium oxide. Importantly, many of the achievements are easily transferable to other important reducible oxides, making the conclusions reached points of general interest to the broad community of oxide-based heterogeneous catalysis.

Bibliography

[1] T. Duchoň, F. Dvořák, M. Aulická, V. Stetsovych, M. Vorokhta, D. Mazur, K. Veltruská, T. Skála, J. Mysliveček, I. Matolínová, and V. Matolín. Ordered phases of reduced ceria as epitaxial films on Cu(111). *J. Phys. Chem. C*, 118:357–365, 2014.

[2] R. Schlögl. Heterogeneous catalysis. *Angew. Chemie Int. Ed.*, 54:3465–3520, 2015.

[3] C. Doornkamp and V. Ponec. The universal character of the Mars and Van Krevelen mechanism. *J. Mol. Catal. A Chem.*, 162:19–32, 2000.

[4] G. A. Somorjai, K. R. McCrea, and J. Zhu. Active sites in heterogeneous catalysis: development of molecular concepts and future challenges. *Top. Catal.*, 18:157–166, 2002.

[5] H.-J. Freund. Model studies in heterogeneous catalysis. *Chem. - A Eur. J.*, 16:9384–9397, 2010.

[6] T. Montini, M. Melchionna, M. Monai, and P. Fornasiero. Fundamentals and catalytic applications of CeO_2-based materials. *Chem. Rev.*, 116:5987–6041, 2016.

[7] U. Diebold. The surface science of titanium dioxide. *Surf. Sci. Rep.*, 48:53–229, 2003.

[8] D. N. Mueller, M. L. Machala, H. Bluhm, and W. C. Chueh. Redox activity of surface oxygen anions in oxygen-deficient perovskite oxides during electrochemical reactions. *Nat. Commun.*, 6:6097, 2015.

[9] Y. Pan, N. Nilius, C. Stiehler, H.-J. Freund, J. Goniakowski, and C. Noguera. Ceria nanocrystals exposing wide (100) facets: structure and polarity compensation. *Adv. Mater. Interfaces*, 1:1400404, 2014.

[10] D. R. Mullins. The surface chemistry of cerium oxide. *Surf. Sci. Rep.*, 70:42–85, 2015.

[11] G. Vilé, S. Colussi, F. Krumeich, A. Trovarelli, and J. Pérez-Ramírez. Opposite face sensitivity of CeO_2 in hydrogenation and oxidation catalysis. *Angew. Chem. Int. Ed.*, 53:12069–12072, 2014.

[12] P. M. Albrecht and D. R. Mullins. Adsorption and reaction of methanol over CeO_x/(100) thin films. *Langmuir*, 29:4559–4567, 2013.

[13] J. Paier, C. Penschke, and J. Sauer. Oxygen defects and surface chemistry of ceria: quantum chemical studies compared to experiment. *Chem. Rev.*, 113:3949–3985, 2013.

[14] C. L. Muhich. Re-evaluating CeO_2 expansion upon reduction: noncounterpoised forces, not ionic radius effects, are the cause. *J. Phys. Chem. C*, 121(14):8052–8059, 2017.

[15] F. Esch, S. Fabris, L. Zhou, T. Montini, C. Africh, P. Fornasiero, G. Comelli, and R. Rosei. Electron localization determines defect formation on ceria substrates. *Science*, 309:752–755, 2005.

[16] N. Skorodumova, S. Simak, B. Lundqvist, I. Abrikosov, and B. Johansson. Quantum origin of the oxygen storage capability of ceria. *Phys. Rev. Lett.*, 89:166601, 2002.

[17] E. A. Kümmerle and G. Heger. The structures of c-$Ce_2O_{3+\delta}$, Ce_7O_{12}, and $Ce_{11}O_{20}$. *J. Solid State Chem.*, 147:485–500, 1999.

[18] M. Ganduglia-Pirovano, J. Da Silva, and J. Sauer. Density-functional calculations of the structure of near-surface oxygen vacancies and electron localization on CeO_2(111). *Phys. Rev. Lett.*, 102:026101, 2009.

[19] J. Kullgren, M. J. Wolf, C. W. M. Castleton, P. Mitev, W. J. Briels, and K. Hermansson. Oxygen vacancies versus fluorine at CeO_2(111): a case of mistaken identity? *Phys. Rev. Lett.*, 112:156102, 2014.

[20] J.-D. Cafun, K. O. Kvashnina, E. Casals, V. F. Puntes, and P. Glatzel. Absence of Ce^{3+} sites in chemically active colloidal ceria nanoparticles. *ACS Nano*, 7:10726–10732, 2013.

[21] J. Kullgren, K. Hermansson, and C. Castleton. Many competing ceria (110) oxygen vacancy structures: from small to large supercells. *J. Chem. Phys.*, 137:044705, 2012.

[22] M. Nolan, S. Grigoleit, D. C. Sayle, S. C. Parker, and G. W. Watson. Density functional theory studies of the structure and electronic structure of pure and defective low index surfaces of ceria. *Surf. Sci.*, 576:217–229, 2005.

[23] J. C. Conesa. Computer modeling of surfaces and defects on cerium dioxide. *Surf. Sci.*, 339:337–352, 1995.

[24] H. Okamoto. Ce–O (Cerium–Oxygen). *J. Phase Equilibria Diffus.*, 29:545–547, 2008.

[25] J. Da Silva. Stability of the Ce_2O_3 phases: a DFT+U investigation. *Phys. Rev. B*, 76:193108, 2007.

[26] A Trovarelli. *Catalysis by ceria and related materials.* Imperial College Press: London, 2002. ISBN 978-1860942990.

[27] D. R. Mullins, P. V. Radulovic, and S. H. Overbury. Ordered cerium oxide thin films grown on Ru(0001) and Ni(111). *Surf. Sci.*, 429:186–198, 1999.

[28] S. Eck, C. Castellarin-Cudia, S. Surnev, M. G. Ramsey, and F. P. Netzer. Growth and thermal properties of ultrathin cerium oxide layers on Rh(111). *Surf. Sci.*, 520:173–185, 2002.

[29] K.-D. Schierbaum. Ordered ultra-thin cerium oxide overlayers on Pt(111) single crystal surfaces studied by LEED and XPS. *Surf. Sci.*, 399:29–38, 1998.

[30] M. Alexandrou and R. M. Nix. The growth, structure and stability of ceria overlayers on Pd(111). *Surf. Sci.*, 321:47–57, 1994.

[31] T. Staudt, Y. Lykhach, L. Hammer, M. A. Schneider, V. Matolín, and J. Libuda. A route to continuous ultra-thin cerium oxide films on Cu(111). *Surf. Sci.*, 603:3382–3388, 2009.

[32] Y. J. Kim, Y. Gao, G. S. Herman, S. Thevuthasan, W. Jiang, D. E. McCready, and S. A. Chambers. Growth and structure of epitaxial CeO_2 by oxygen-plasma-assisted molecular beam epitaxy. *J. Vac. Sci. Technol., A*, 17:926, 1999.

[33] O. Stetsovych, F. Dvořák, L. Szabová, S. Fabris, J. Mysliveček, and V. Matolín. Nanometer-range strain distribution in layered incommensurate systems. *Phys. Rev. Lett.*, 109:266102, 2012.

[34] F. Dvořák, O. Stetsovych, M. Steger, E. Cherradi, I. Matolínová, N. Tsud, M. Škoda, T. Skála, J. Mysliveček, and V. Matolín. Adjusting morphology and surface reduction of $CeO_2(111)$ thin films on Cu(111). *J. Phys. Chem. C*, 115:7496–7503, 2011.

[35] F. Yang, Y. Choi, P. Liu, D. Stacchiola, J. Hrbek, and J. A. Rodriguez. Identification of 5–7 defects in a copper oxide surface. *J. Am. Chem. Soc.*, 133:11474–11477, 2011.

[36] L. Szabová, O. Stetsovych, F. Dvořák, M. Farnesi Camellone, S. Fabris, J. Mysliveček, and V. Matolín. Distinct physicochemical properties of the first ceria monolayer on Cu(111). *J. Phys. Chem. C*, 116:6677–6684, 2012.

[37] C. S. Fadley. X-ray photoelectron spectroscopy and diffraction in the hard X-ray regime: fundamental considerations and future possibilities. *Nucl. Instrum. Methods Phys. Res. Sect. A: Accel. Spectrom. Detect. Assoc. Equip.*, 547:24–41, 2005.

[38] J. J. Yeh and I. Lindau. Atomic subshell photoionization cross sections and asymmetry parameters: $1 \leq Z \leq 103$. *At. Data Nucl. Data Tables*, 32:1–155, 1985.

[39] J. Cooper. Photoionization from outer atomic subshells: a model study. *Phys. Rev.*, 128:681–693, 1962.

[40] S. Tanuma, C. J. Powell, and D. R. Penn. Calculation of electron inelastic mean free paths (IMFPs) VII: reliability of the TPP-2M IMFP predictive equation. *Surf. Interface Anal.*, 35:268–275, 2003.

[41] S. M. Goldberg, C. S. Fadley, and S. Kono. Photoionization cross-sections for atomic orbitals with random and fixed spatial orientation. *J. Electron Spectros. Relat. Phenomena*, 21:285–363, 1981.

[42] C. Westphal. The study of the local atomic structure by means of X-ray photoelectron diffraction. *Surf. Sci. Rep.*, 50:1–106, 2003.

[43] A. B. McLean, C. E. J. Mitchell, and D. M. Swanston. Implementation of an efficient analytical approximation to the Voigt function for photoemission lineshape analysis. *J. Electron Spectros. Relat. Phenomena*, 69:125–132, 1994.

[44] D. A. Shirley. High-resolution X-ray photoemission spectrum of the valence bands of gold. *Phys. Rev. B*, 5:4709–4714, 1972.

[45] S. Tougaard. Quantitative analysis of the inelastic background in surface electron spectroscopy. *Surf. Interface Anal.*, 11:453–472, 1988.

[46] A. Herrera-Gomez, M. Bravo-Sanchez, F. S. Aguirre-Tostado, and M. O. Vazquez-Lepe. The slope-background for the near-peak regime of photoemission spectra. *J. Electron Spectros. Relat. Phenomena*, 189:76–80, 2013.

[47] M. Wojdyr. Fityk : a general-purpose peak fitting program. *J. Appl. Crystallogr.*, 43:1126–1128, 2010.

[48] C. S. Fadley. X-ray photoelectron spectroscopy: progress and perspectives. *J. Electron Spectros. Relat. Phenomena*, 178-179:2–32, 2010.

[49] J. I. Flege and E. E. Krasovskii. Intensity-voltage low-energy electron microscopy for functional materials characterization. *Phys. Status Solidi RRL*, 8:463–477, 2014.

[50] F. Reinert and Ss. Hüfner. Photoemission spectroscopy—from early days to recent applications. *New J. Phys.*, 7:97, 2005.

[51] T. Duchoň, Diploma thesis: *Physically-chemical properties of epitaxial films $CeO_x/Cu(111)$*. Charles University: Prague, 2013.

[52] F. Dvořák, Doctoral thesis: *Interaction of Simple Molecules with Reducible Oxides: Model Studies of H_2O/CeO_x and CO/CuO_x. Charles University: Prague, 2013.*

[53] R. Vašina, V. Kolařík, P. Doležel, M. Mynář, M. Vondráček, V. Cháb, J. Slezák, C. Comicioli, and K. C. Prince. Mechanical design aspects of a soft X-ray plane grating monochromator. *Nucl. Instrum. Methods Phys. Res. Sect. A: Accel. Spectrom. Detect. Assoc. Equip.*, 467-468:561–564, 2001.

[54] MSB. `https://www.elettra.trieste.it/it/lightsources/elettra/elettra-beamlines/msb/beamline-description.html`. Accessed: 2017-05-31.

[55] K. Shimada, M. Arita, T. Matsui, K. Goto, S. Qiao, K. Yoshida, M. Taniguchi, H. Namatame, T. Sekitani, K. Tanaka, H. Yoshida, K. Shirasawa, N. Smolyakov, and A. Hiraya. Linear undulator beamline at a compact storage ring (HiSOR). *Nucl. Instrum. Methods Phys. Res. Sect. A: Accel. Spectrom. Detect. Assoc. Equip.*, 467-468:504–507, 2001.

[56] K. Shimada, M. Arita, Y. Takeda, H. Fujino, K. Kobayashi, T. Narimura, H. Namatame, and M. Taniguchi. High-resolution, low-temperature photoemission spectroscopy at the HiSOR linear undulator beamline. *Surf. Rev. Lett.*, 9:529–534, 2002.

[57] Elmitec LEEM-III. `http://www.elmitec-gmbh.com/Leem.php?Bereich=LEEM3`. Accessed: 2017-05-31.

[58] R. M. Tromp, J. B. Hannon, A. W. Ellis, W. Wan, A. Berghaus, and O. Schaff. A new aberration-corrected, energy-filtered LEEM/PEEM instrument. I. Principles and design. *Ultramicroscopy*, 110:852–861, 2010.

[59] R. M. Tromp, J. B. Hannon, W Wan, A Berghaus, and O Schaff. A new aberration-corrected, energy-filtered LEEM/PEEM instrument II. Operation and results. *Ultramicroscopy*, 127:25–39, 2013.

[60] S. D. Senanayake, D. Stacchiola, J. Evans, M. Estrella, L. Barrio, M. Pérez, J. Hrbek, and J. A. Rodriguez. Probing the reaction intermediates for the water-gas shift over inverse CeO_x/Au(111) catalysts. *J. Catal.*, 271:392–400, 2010.

[61] V. Stetsovych, F. Pagliuca, F. Dvořák, T. Duchoň, M. Vorokhta, M. Aulická, J. Lachnitt, S. Schernich, I. Matolínová, K. Veltruská, T. Skála, D. Mazur, J. Mysliveček, J. Libuda, and V. Matolín. Epitaxial cubic Ce_2O_3 films via Ce–CeO_2 interfacial reaction. *J. Phys. Chem. Lett.*, 4:866–871, 2013.

[62] C. L. Perkins, M. A. Henderson, C. H. F. Peden, and Gregory S. Herman. Self-diffusion in ceria. *J. Vac. Sci. Technol., A*, 19:1942–1946, 2001.

[63] J. Höcker, J.-O. Krisponeit, T. Schmidt, J. Falta, and J. I. Flege. The cubic-to-hexagonal phase transition of cerium oxide particles: dynamics and structure. *Nanoscale [advanced article]*, 2017. DOI: 10.1039/C6NR09760J.

[64] R. Olbrich, G. E. Murgida, V. Ferrari, C. Barth, A. M. Llois, M. Reichling, and M. V. Ganduglia-Pirovano. Surface stabilizes ceria in unexpected stoichiometry. *J. Phys. Chem. C*, 121:6844–6851, 2017.

[65] A. Trovarelli, C. de Leitenburg, M. Boaro, and G. Dolcetti. The utilization of ceria in industrial catalysis. *Catal. Today*, 50:353–367, 1999.

[66] I. E. Wachs. Catalysis science of supported vanadium oxide catalysts. *Dalton Trans.*, 42:11762–11769, 2013.

[67] S. A. C. Carabineiro, N. Bogdanchikova, P. B. Tavares, and J. L. Figueiredo. Nanostructured iron oxide catalysts with gold for the oxidation of carbon monoxide. *RSC Adv.*, 2:2957–2965, 2012.

[68] J. Rosen, G. S. Hutchings, and F. Jiao. Ordered mesoporous cobalt oxide as highly efficient oxygen evolution catalyst. *J. Am. Chem. Soc.*, 135:4516–4521, 2013.

[69] Y. Gorlin, B. Lassalle-Kaiser, J. D. Benck, S. Gul, S. M. Webb, V. K. Yachandra, J. Yano, and T. F. Jaramillo. In situ X-ray absorption spectroscopy investigation of a bifunctional manganese oxide catalyst with high activity for electrochemical water oxidation and oxygen reduction. *J. Am. Chem. Soc.*, 135:8525–8534, 2013.

[70] Y. Borchert, P. Sonstrom, M. Wilhelm, H. Borchert, and M. Baumer. Nanostructured praseodymium oxide: preparation, structure, and catalytic properties. *J. Phys. Chem. C*, 112:3054–3063, 2008.

[71] M. Schubert. CO oxidation over supported gold catalysts—"inert" and "active" support materials and their role for the oxygen supply during reaction. *J. Catal.*, 197:113–122, 2001.

[72] R. Maezono, S. Ishihara, and N. Nagaosa. Phase diagram of manganese oxides. *Phys. Rev. B*, 58:11583–11596, 1998.

[73] G. Ketteler, W. Weiss, W. Ranke, and R. Schlögl. Bulk and surface phases of iron oxides in an oxygen and water atmosphere at low pressure. *Phys. Chem. Chem. Phys.*, 3:1114–1122, 2001.

[74] P. Waldner and G. Eriksson. Thermodynamic modelling of the system titanium–oxygen. *CALPHAD: Comput. Coupling Phase Diagrams Thermochem.*, 23:189–218, 1999.

[75] M. Zinkevich, D. Djurovic, and F. Aldinger. Thermodynamic modelling of the cerium–oxygen system. *Solid State Ionics*, 177:989–1001, 2006.

[76] H. Katzke, P. Tolédano, and W Depmeier. Theory of morphotropic transformations in vanadium oxides. *Phys. Rev. B*, 68:024109, 2003.

[77] L. Ruh and V. A. Patel. Proposed phase relations in the HfO_2-rich portion of the system Hf–HfO_2. *J. Am. Ceram. Soc.*, 56:606–607, 1973.

[78] S. Ferro. Physicochemical and electrical properties of praseodymium oxides. *Int. J. Electrochem.*, 2011:1–7, 2011.

[79] R. Arroyave, L. Kaufman, and T. W. Eagar. Thermodynamic modeling of the Zr–O system. *CALPHAD: Comput. Coupling Phase Diagrams Thermochem.*, 26:95–118, 2002.

[80] P. Sonström, J. Birkenstock, Y. Borchert, L. Schilinsky, P. Behrend, K. Gries, K. Müller, A. Rosenauer, and M. Bäumer. Nanostructured praseodymium oxide: correlation between phase transitions and catalytic activity. *ChemCatChem*, 2:694–704, 2010.

[81] C. Franchini, R. Podloucky, F. Allegretti, F. Li, G. Parteder, S. Surnev, and F. P. Netzer. Structural and vibrational properties of two-dimensional Mn_xO_y layers on Pd(100): experiments and density functional theory calculations. *Phys. Rev. B*, 79:035420, 2009.

[82] K. Biedermann, M. Gubo, L. Hammer, and K. Heinz. Phases and phase transitions of hexagonal cobalt oxide films on Ir(100)-(1×1). *J. Phys.: Condens. Matter*, 21:185003, 2009.

[83] G. Ketteler and W. Ranke. Heteroepitaxial growth and nucleation of iron oxide films on Ru(0001). *J. Phys. Chem. B*, 107:4320–4333, 2003.

[84] M. V. Ganduglia-Pirovano, A. Hofmann, and J. Sauer. Oxygen vacancies in transition metal and rare earth oxides: current state of understanding and remaining challenges. *Surf. Sci. Rep.*, 62:219–270, 2007.

[85] N. J. Lawrence, J. R. Brewer, L. Wang, T.-S. Wu, J. Wells-Kingsbury, M. M. Ihrig, G. Wang, Y.-L. Soo, W.-N. Mei, and C. L. Cheung. Defect engineering in cubic cerium oxide nanostructures for catalytic oxidation. *Nano Lett.*, 11:2666–2671, 2011.

[86] S. P. Ray and D. E. Cox. Neutron diffraction determination of the crystal dtructure of Ce_7O_{12}. *J. Solid State Chem.*, 15:333–343, 1975.

[87] P. Knappe and L. Eyring. Preparation and electron microscopy of intermediate phases in the interval Ce_7O_{12}–$Ce_{11}O_{20}$. *J. Solid State Chem.*, 58:312–324, 1985.

[88] H. Wilkens, O. Schuckmann, R. Oelke, S. Gevers, A. Schaefer, M. Bäumer, M. H. Zoellner, T. Schroeder, and J. Wollschläger. Stabilization of the ceria ι-phase (Ce_7O_{12}) surface on Si(111). *Appl. Phys. Lett.*, 102:111602, 2013.

[89] H. Wilkens, O. Schuckmann, R. Oelke, S. Gevers, M. Reichling, A. Schaefer, M. Bäumer, M. H. Zoellner, G. Niu, T. Schroeder, and J. Wollschläger. Structural transitions of epitaxial ceria films on Si(111). *Phys. Chem. Chem. Phys.*, 15:18589–18599, 2013.

[90] T. Skála, F. Šutara, K. C. Prince, and V. Matolín. Cerium oxide stoichiometry alteration via Sn deposition: influence of temperature. *J. Electron Spectrosc. Relat. Phenom.*, 169:20–25, 2009.

[91] F. Pagliuca, P. Luches, and S. Valeri. Interfacial interaction between cerium oxide and silicon surfaces. *Surf. Sci.*, 607:164–169, 2013.

[92] C. J. Powell, A. Jablonski, I. S. Tilinin, S. Tanuma, and D. R. Penn. Surface sensitivity of auger-electron spectroscopy and X-ray photoelectron spectroscopy. *J. Electron Spectrosc. Relat. Phenom.*, 98-99:1–15, 1999.

[93] V. Matolín, M. Cabala, V. Cháb, I. Matolínová, K. C. Prince, M. Škoda, F. Šutara, T. Skála, and K. Veltruská. A resonant photoelectron spectroscopy study of SnO_x doped CeO_2 catalysts. *Surf. Interface Anal.*, 40:225–230, 2008.

[94] D. R. Mullins, S. H. Overbury, and D. R. Huntley. Electron spectroscopy of single crystal and polycrystalline cerium oxide surfaces. *Surf. Sci.*, 409:307–319, 1998.

[95] C. Castellarin-Cudia, S. Surnev, G. Schneider, R. Podlucky, M. G. Ramsey, and F. P. Netzer. Strain-induced formation of arrays of catalytically active sites at the metal–oxide interface. *Surf. Sci.*, 554:L120–L126, 2004.

[96] E. Vescovo and C. Carbone. Oxidation of epitaxial Ce films. *Phys. Rev. B*, 53:4142–4147, 1996.

[97] K. Mudiyanselage, S. D. Senanayake, L. Feria, S. Kundu, A. E. Baber, J. Graciani, A. B. Vidal, S. Agnoli, J. Evans, R. Chang, S. Axnanda, Z. Liu, J. F. Sanz, P. Liu, J. A. Rodriguez, and D. J. Stacchiola. Importance of the metal–oxide interface in catalysis: in situ studies of the water-gas shift reaction by ambient-pressure X-ray photoelectron spectroscopy. *Angew. Chem. Int. Ed.*, 52:5101–5105, 2013.

[98] S. Torbrügge, M. Reichling, A. Ishiyama, S. Morita, and Ó. Custance. Evidence of subsurface oxygen vacancy ordering on reduced $CeO_2(111)$. *Phys. Rev. Lett.*, 99:056101, 2007.

[99] G. E. Murgida and M. V. Ganduglia-Pirovano. Evidence for subsurface ordering of oxygen vacancies on the reduced $CeO_2(111)$ surface using density-functional and statistical calculations. *Phys. Rev. Lett.*, 110:246101, 2013.

[100] Y. Zhou, J. M. Perket, and J. Zhou. Growth of Pt nanoparticles on reducible $CeO_2(111)$ thin films: effect of nanostructures and redox properties of ceria. *J. Phys. Chem. C*, 114:11853–11860, 2010.

[101] K. Mašek, J. Beran, and V. Matolín. RHEED study of the growth of cerium oxide on Cu(111). *Appl. Surf. Sci.*, 259:34–38, 2012.

[102] C. Loschen, A. Migani, S. T. Bromley, F. Illas, and K. M. Neyman. Density functional studies of model cerium oxide nanoparticles. *Phys. Chem. Chem. Phys.*, 10:5730–5738, 2008.

[103] S. Turner, S. Lazar, B. Freitag, R. Egoavil, J. Verbeeck, S. Put, Y. Strauven, and G. Van Tendeloo. High sesolution mapping of surface reduction in ceria nanoparticles. *Nanoscale*, 3:3385–3390, 2011.

[104] G. D. Wang, D. D. Kong, Y. H. Pan, H. B. Pan, and J. F. Zhu. Low energy Ar-ion bombardment effects on the CeO_2 surface. *Appl. Surf. Sci.*, 258:2057–2061, 2012.

[105] W. Xiao, Q. Guo, and E. G. Wang. Transformation of $CeO_2(111)$ to $Ce_2O_3(0001)$ films. *Chem. Phys. Lett.*, 368:527–531, 2003.

[106] M. Aulická, T. Duchoň, F. Dvořák, V. Stetsovych, J. Beran, K. Veltruská, J. Mysliveček, K. Mašek, and V. Matolín. Faceting transition at the oxide–metal interface: (13 13 1) facets on Cu(110) induced by carpet-like ceria overlayer. *J. Phys. Chem. C*, 119:1851–1858, 2015.

[107] J.-L. Lu, H.-J. Gao, S. Shaikhutdinov, and H.-J. Freund. Morphology and defect structure of the $CeO_2(111)$ films grown on Ru(0001) as studied by scanning tunneling nicroscopy. *Surf. Sci.*, 600:5004–5010, 2006.

[108] B. Kaemena, S. D. Senanayake, A. Meyer, J. T. Sadowski, J. Falta, and J. I. Flege. Growth and morphology of ceria on ruthenium (0001). *J. Phys. Chem. C*, 117:221–232, 2013.

[109] O. Balmes, G. Prevot, X. Torrelles, E. Lundgren, and S. Ferrer. Diatomic steps in Pt(997) surfaces are better catalysts than monatomic steps for the CO oxidation reaction near atmospheric pressure. *ACS Catal.*, 6:1285–1291, 2016.

[110] B. Eren, D. Zherebetskyy, L. L. Patera, C. H. Wu, H. Bluhm, C. Africh, L.-W. Wang, G. A. Somorjai, and M. Salmeron. Activation of Cu(111) surface by decomposition into nanoclusters driven by CO adsorption. *Science*, 351:475–478, 2016.

[111] M. Capdevila-Cortada, G. Vilé, D. Teschner, J. Pérez-Ramírez, and N. López. Reactivity descriptors for ceria in catalysis. *Appl. Catal. B Environ.*, 197:299–312, 2016.

[112] H.-X. Mai, L.-D. Sun, Y.-W. Zhang, R. Si, W. Feng, H.-P. Zhang, H.-C. Liu, and C.-H. Yan. Shape-selective synthesis and oxygen storage behavior of ceria nanopolyhedra, nanorods, and nanocubes. *J. Phys. Chem. B*, 109:24380–24385, 2005.

[113] K. Zhou, X. Wang, X. Sun, Q. Peng, and Y. Li. Enhanced catalytic activity of ceria nanorods from well-defined reactive crystal planes. *J. Catal.*, 229:206–212, 2005.

[114] Tana, M. Zhang, J. Li, H. Li, Y. Li, and W. Shen. Morphology-dependent redox and catalytic properties of CeO_2 nanostructures: nanowires, nanorods and nanoparticles. *Catal. Today*, 148:179–183, 2009.

[115] S. Y. Yao, W. Q. Xu, A. C. Johnston-Peck, F. Z. Zhao, Z. Y. Liu, S. Luo, S. D. Senanayake, A. Martinez-Arias, W. J. Liu, and J. A. Rodriguez. Morphological effects of the nanostructured ceria support on the activity and stability of CuO/CeO_2 catalysts for the water-gas shift reaction. *Phys. Chem. Chem. Phys.*, 16:17183–17195, 2014.

[116] O. Stetsovych, J. Beran, F. Dvořák, K. Mašek, J. Mysliveček, and V. Matolín. Polarity driven morphology of $CeO_2(100)$ islands on Cu(111). *Appl. Surf. Sci.*, 285:766–771, 2013.

[117] J. Graciani, K. Mudiyanselage, F. Xu, A. E. Baber, J. Evans, S. D. Senanayake, D. J. Stacchiola, P. Liu, J. Hrbek, J. F. Sanz, and J. A. Rodriguez. Highly active copper–ceria and copper–ceria–titania catalysts for methanol synthesis from CO_2. *Science*, 345:546–550, 2014.

[118] D. R. Mullins, S. D. Senanayake, and T.-L. Chen. Adsorption and reaction of C_1-C_3 alcohols over $CeO_x(111)$ thin films. *J. Phys. Chem. C*, 114:17112–17119, 2010.

[119] J. Höcker, W. Cartas, A. Schaefer, M. Bäumer, J. F. Weaver, J. Falta, and J. I. Flege. Growth, structure, and stability of the high-index $TbO_x(112)$ surface on Cu(111). *J. Phys. Chem. C*, 119:14175–14184, 2015.

[120] P. Luches and S. Valeri. Structure, morphology and reducibility of epitaxial cerium oxide ultrathin films and nanostructures. *Materials*, 8:5818–5833, 2015.

[121] S. A. Chambers. Epitaxial growth and properties of doped transition metal and complex oxide films. *Adv. Mater.*, 22:219–248, 2010.

[122] N. V. Skorodumova, M. Baudin, and K. Hermansson. Surface properties of CeO_2 from first principles. *Phys. Rev. B*, 69:075401, 2004.

[123] M. M. Branda, R. M. Ferullo, M. Causá, and F. Illas. Relative stabilities of low index and stepped CeO_2 surfaces from hybrid and GGA+U implementations of density functional theory. *J. Phys. Chem. C*, 115:3716–3721, 2011.

[124] M. Fronzi, A. Soon, B. Delley, E. Traversa, and C. Stampfl. Stability and morphology of cerium oxide surfaces in an oxidizing environment: a first-principles investigation. *J. Chem. Phys.*, 131:104701, 2009.

[125] F. Yang, Y. Choi, S. Agnoli, P. Liu, D. Stacchiola, J. Hrbek, and J. A. Rodriguez. $CeO_2 \leftrightarrow CuO_x$ interactions and the controlled assembly of $CeO_2(111)$ and $CeO_2(100)$ nanoparticles on an oxidized Cu(111) substrate. *J. Phys. Chem. C*, 115:23062–23066, 2011.

[126] F. Jensen, F. Besenbacher, E. Lægsgaard, and I. Stensgaard. Oxidation of Cu(111): two new oxygen induced reconstructions. *Surf. Sci.*, 259:774–780, 1991.

[127] P. W. Tasker. The stability of ionic crystal surfaces. *J. Phys. C Solid State*, 12:4977–4984, 1979.

[128] T. Hahn. *International tables for crystallography Vol. A: space-group symmetry*. Springer, 5. edition, 2005. ISBN 978-0792365907.

[129] W. S. Yang and F. Jona. Missing spots in low-energy electron-diffraction patterns. *Phys. Rev. B*, 29:899–906, 1984.

[130] A. Tiwari and S. Titinchi, editors. *Advanced Catalytic Materials*. John Wiley & Sons, Inc.: Hoboken, NJ, 2015. ISBN 978-1118998281.

[131] J.-F. Jerratsch, X. Shao, N. Nilius, H.-J. Freund, C. Popa, M. V. Ganduglia-Pirovano, A. M. Burow, and J. Sauer. Electron localization in defective ceria films: a study with scanning-tunneling microscopy and density-functional theory. *Phys. Rev. Lett.*, 106:246801, 2011.

[132] G. N. Vayssilov, Y. Lykhach, A. Migani, T. Staudt, G. P. Petrova, N. Tsud, T. Skála, A. Bruix, F. Illas, K. C. Prince, V. Matolín, K. M. Neyman, and J. Libuda. Support nanostructure boosts oxygen transfer to catalytically active platinum nanoparticles. *Nat. Mater.*, 10:310–315, 2011.

[133] J. A. Rodriguez, J. Graciani, J. Evans, J. B. Park, F. Yang, D. Stacchiola, S. D. Senanayake, S. Ma, M. Pérez, P. Liu, J. F. Sanz, and J. Hrbek. Water-gas shift reaction on a highly active inverse $CeO_x/Cu(111)$ catalyst: unique role of ceria nanoparticles. *Angew. Chem., Int. Ed.*, 121:8191–8194, 2009.

[134] J. Höcker, T. Duchoň, K. Veltruská, V. Matolín, J. Falta, S. D. Senanayake, and J. I. Flege. Controlling heteroepitaxy by oxygen chemical potential: exclusive growth of (100) oriented ceria nanostructures on Cu(111). *J. Phys. Chem. C*, 120:4895–4901, 2016.

[135] D. R. Mullins, P. M. Albrecht, and F. Calaza. Variations in reactivity on different crystallographic orientations of cerium oxide. *Top. Catal.*, 56:1345–1362, 2013.

[136] J. I. Flege, J. Höcker, B. Kaemena, T. O. Menteş, A. Sala, A. Locatelli, S. Gangopadhyay, J. T. Sadowski, S. D. Senanayake, and J. Falta. Growth and characterization of epitaxially stabilized ceria(001) nanostructures on Ru(0001). *Nanoscale*, 8(20):10849–10856, 2016.

[137] B. L. M. Hendriksen, M. D. Ackermann, R. van Rijn, D. Stoltz, I. Popa, O. Balmes, A. Resta, D. Wermeille, R. Felici, S. Ferrer, and J. W. M. Frenken. The role of steps in surface catalysis and reaction oscillations. *Nat. Chem.*, 2:730–734, 2010.

[138] M. Grioni, J. F. van Acker, M. T. Czyžyk, and J. C. Fuggle. Unoccupied electronic structure and core-hole effects in the X-ray-absorption spectra of Cu_2O. *Phys. Rev. B*, 45:3309–3318, 1992.

[139] A. J. Therrien, R. Zhang, F. R. Lucci, M. D. Marcinkowski, A. Hensley, J.-S. McEwen, and E. C. H. Sykes. Structurally accurate model for the '29'-structure of Cu_xO/Cu(111): a DFT and STM study. *J. Phys. Chem. C*, 120:10879–10886, 2016.

[140] F. Jensen, F. Besenbacher, and I. Stensgaard. Two new oxygen induced reconstructions on Cu(111). *Surf. Sci.*, 269-270:400–404, 1992.

[141] J. Höcker, T. O. Menteş, A. Sala, A. Locatelli, T. Schmidt, J. Falta, S. D. Senanayake, and J. I. Flege. Unraveling the dynamic nanoscale reducibility ($Ce^{4+} \rightarrow Ce^{3+}$) of CeO_x–Ru in hydrogen activation. *Adv. Mater. Interfaces*, 2:1500314, 2015.

[142] S. Hočevar, J. Batista, and J. Levec. Wet oxidation of phenol on $Ce_{1-x}Cu_xO_{2-\delta}$ catalyst. *J. Catal.*, 184:39–48, 1999.

[143] X. Wang, J. A. Rodriguez, J. C. Hanson, D. Gamarra, A. Martínez-Arias, and M. Fernández-García. In situ studies of the active sites for the water gas shift reaction over Cu–CeO_2 catalysts: complex interaction between metallic copper and oxygen vacancies of ceria. *J. Phys. Chem. B*, 110:428–434, 2006.

[144] F. Wang, R. Büchel, A. Savitsky, M. Zalibera, D. Widmann, S. E. Pratsinis, W. Lubitz, and F. Schüth. In situ EPR study of the redox properties of CuO–CeO_2 catalysts for preferential CO oxidation (PROX). *ACS Catal.*, 6:3520–3530, 2016.

[145] S. D. Senanayake, D. Stacchiola, and J. A. Rodriguez. Unique properties of ceria nanoparticles supported on metals: novel inverse ceria/copper catalysts for CO oxidation and the water-gas shift reaction. *Acc. Chem. Res.*, 46:1702–1711, 2013.

[146] S. Yao, K. Mudiyanselage, W. Xu, A. C. Johnston-Peck, J. C. Hanson, T. Wu, D. Stacchiola, J. A. Rodriguez, H. Zhao, K. A. Beyer, K. W. Chapman, P. J. Chupas, A. Martínez-Arias, R. Si, T. B. Bolin, W. Liu, and S. D. Senanayake. Unraveling the dynamic nature of a CuO/CeO_2 catalyst for CO oxidation in operando : a combined study of XANES (fluorescence) and DRIFTS. *ACS Catal.*, 4:1650–1661, 2014.

[147] S. D. Senanayake, P. J. Ramírez, I. Waluyo, S. Kundu, K. Mudiyanselage, Z. Liu, Z. Liu, S. Axnanda, D. J. Stacchiola, J. Evans, and J. A. Rodriguez. Hydrogenation of CO_2 to methanol on CeO_x/Cu(111) and ZnO/Cu(111) catalysts: role of the metal–oxide interface and importance of Ce^{3+} sites. *J. Phys. Chem. C*, 120:1778–1784, 2016.

[148] V. Matolín, I. Matolínová, F. Dvořák, V. Johánek, J. Mysliveček, K. C. Prince, T. Skála, O. Stetsovych, N. Tsud, M. Václavů, and B. Šmíd. Water interaction with CeO_2(111)/Cu(111) model catalyst surface. *Catal. Today*, 181:124–132, 2012.

[149] D. R. Mullins, P. M. Albrecht, T.-L. Chen, F. C. Calaza, M. D. Biegalski, H. M. Christen, and S. H. Overbury. Water dissociation on CeO_2(100) and CeO_2(111) thin films. *J. Phys. Chem. C*, 116:19419–19428, 2012.

[150] Lj. Kundakovic, D. R. Mullins, and S. H. Overbury. Adsorption and reaction of H_2O and CO on oxidized and reduced Rh/CeO_x(111) surfaces. *Surf. Sci.*, 457:51–62, 2000.

[151] M. A. Henderson, C. L. Perkins, M. H. Engelhard, S. Thevuthasan, and C. H. F. Peden. Redox properties of water on the oxidized and reduced surfaces of CeO_2(111). *Surf. Sci.*, 526:1–18, 2003.

[152] D. R. Mullins and K. Z. Zhang. Metal–support interactions between Pt and thin film cerium oxide. *Surf. Sci.*, 513:163–173, 2002.

[153] M. Happel, J. Mysliveček, V. Johánek, F. Dvořák, O. Stetsovych, Y. Lykhach, V. Matolín, and J. Libuda. Adsorption sites, metal–support interactions, and oxygen spillover identified by vibrational spectroscopy of adsorbed CO: a model study on Pt/ceria catalysts. *J. Catal.*, 289:118–126, 2012.

[154] A. Neitzel, Y. Lykhach, T. Skála, N. Tsud, M. Vorokhta, D. Mazur, K. C. Prince, V. Matolín, and J. Libuda. Surface sites on Pt–CeO_2 mixed oxide catalysts probed by CO adsorption: a synchrotron radiation photoelectron spectroscopy study. *Phys. Chem. Chem. Phys.*, 16:24747–24754, 2014.

[155] F. C. Calaza, T. L. Chen, D. R. Mullins, Y. Xu, and S. H. Overbury. Reactivity and reaction intermediates for acetic acid adsorbed on CeO_2(111). *Catal. Today*, 253:65–76, 2015.

[156] A. Neitzel, Y. Lykhach, V. Johánek, N. Tsud, T. Skála, K. C. Prince, V. Matolín, and J. Libuda. Decomposition of acetic acid on model Pt/CeO_2 catalysts: the effect of surface crowding. *J. Phys. Chem. C*, 119:13721–13734, 2015.

[157] P. F. Walch and D. E. Ellis. One-electron interpretation of optical absorption and soft-X-ray data in MgO. *Phys. Rev. B*, 8:5920–5933, 1973.

[158] N. Daude, C. Jouanin, and C. Gout. Electronic band structure of magnesium and calcium oxides. *Phys. Rev. B*, 15:2399–2405, 1977.

[159] Y.-N. Xu and W. Y. Ching. Self-consistent band structures, charge distributions, and optical-absorption spectra in MgO, α-Al_2O_3, and $MgAl_2O_4$. *Phys. Rev. B*, 43:4461–4472, 1991.

[160] O. E. Taurian, M. Springborg, and N. E. Christensen. Self-consistent electronic structures of MgO and SrO. *Solid State Commun.*, 55:351–355, 1985.

[161] E. Wuilloud, B. Delley, W.-D. Schneider, and Y. Baer. Spectroscopic evidence for localized and extended f-symmetry states in CeO_2. *Phys. Rev. Lett.*, 53:202–205, 1984.

[162] F. Marabelli and P. Wachter. Covalent insulator CeO_2: optical reflectivity measurements. *Phys. Rev. B*, 36:1238–1243, 1987.

[163] A. Fujimori. Mixed-valent ground state of CeO_2. *Phys. Rev. B*, 28:2281–2283, 1983.

[164] M. Matsumoto, K. Soda, K. Ichikawa, S. Tanaka, Y. Taguchi, K. Jouda, O. Aita, Y. Tezuka, and S. Shin. Resonant photoemission study of CeO_2. *Phys. Rev. B*, 50:11340–11346, 1994.

[165] A. Schattke and M. A. Van Hove. *Solid-state photoemission and related methods*. WILEY-VCH: Weinheim, 2003. ISBN 978-3527403349.

[166] O. Gunnarsson and K. Schönhammer. Electron spectroscopies for Ce compounds in the impurity model. *Phys. Rev. B*, 28:4315, 1983.

[167] D. D. Koelling, A. M. Boring, and J. H. Wood. The electronic structure of CeO_2 and PrO_2. *Solid State Commun.*, 47:227–232, 1983.

[168] W.-D. Schneider, B. Delley, E. Wuilloud, J.-M. Imer, and Y Baer. Electron-spectroscopic manifestations of the 4f states in light rare-earth solids. *Phys. Rev. B*, 32:6819–6831, 1985.

[169] G. Kaindl, G. K. Wertheim, G. Schmiester, and E. V. Sampathkumaran. Mixed valency versus covalency in rare-earth core-electron spectroscopy. *Phys. Rev. Lett.*, 58:606–609, 1987.

[170] R. C. Karnatak, J.-M. Esteva, H. Dexpert, M Gasgnier, P. E. Caro, and L Albert. X-ray absorption studies of CeO_2, PrO_2, and TbO_2. I. Manifestation of localized and extended f states in the 3d absorption spectra. *Phys. Rev. B*, 36:1745–1749, 1987.

[171] H. Nakamatsu, T. Mukoyama, and H. Adachi. Ionic and covalent bonds in CeO_2 crystal. *Chem. Phys. Lett.*, 247:168–172, 1995.

[172] P. Wachter. Empty f-states, Kondo insulators—or what? *Phys. B Condens. Matter*, 300:105–120, 2001.

[173] E. Shoko, M. F. Smith, and R. H. McKenzie. Mixed valency in cerium oxide crystallographic phases: valence of different cerium sites by the bond valence method. *Phys. Rev. B*, 79:134108, 2009.

[174] M. B. Robin and P. Day. Mixed valence chemistry—a survey and classification. *Adv. Inorg. Chem. Radiochem.*, 10:247–422, 1968.

[175] Peter Day, N. S. Hush, and R. J. H. Clark. Mixed valence: origins and developments. *Philos. Trans. A. Math. Phys. Eng. Sci.*, 366:5–14, 2008.

[176] L. Pauling. *The nature of the chemical bond and the structure of molecules and crystals: an introduction to modern structural chemistry*. Cornell University Press: New York, 1960. ISBN 978-0801403330.

[177] C. M. Varma. Mixed-valence compounds. *Rev. Mod. Phys.*, 48:219–238, 1976.

[178] C. J. Nelin, P. S. Bagus, E. S. Ilton, S. A. Chambers, H. Kuhlenbeck, and H.-J. Freund. Relationships between complex core level spectra and materials properties. *Int. J. Quantum Chem.*, 110:2752–2764, 2010.

[179] P. S. Bagus and C. J. Nelin. Covalent interactions in oxides. *J. Electron Spectros. Relat. Phenomena*, 194:37–44, 2014.

[180] P. S. Bagus, C. J. Nelin, Y. Al-Salik, E. S. Ilton, and H. Idriss. Multiplet splitting for the XPS of heavy elements: dependence on oxidation state. *Surf. Sci.*, 643:142–149, 2016.

[181] J. Heyd, G. E. Scuseria, and M. Ernzerhof. Hybrid functionals based on a screened Coulomb potential. *J. Chem. Phys.*, 124:219906, 2006.

[182] G. Kresse and J. Furthmüller. Efficient iterative schemes for ab initio total-energy calculations using a plane-wave basis set. *Phys. Rev. B*, 54:11169–11186, 1996.

[183] G. Kresse and D. Joubert. From ultrasoft pseudopotentials to the projector augmented-wave method. *Phys. Rev. B*, 59:1758–1775, 1999.

[184] L. Gerward, J. Staun Olsen, L. Petit, G. Vaitheeswaran, V. Kanchana, and A. Svane. Bulk modulus of CeO_2 and PrO_2—an experimental and theoretical study. *J. Alloys Compd.*, 400:56–61, 2005.

[185] P. J. Hay, R. L. Martin, J. Uddin, and G. E. Scuseria. Theoretical study of CeO_2 and Ce_2O_3 using a screened hybrid density functional. *J. Chem. Phys.*, 125:034712, 2006.

[186] G.-y. Adachi and N. Imanaka. The binary rare earth oxides. *Chem. Rev.*, 98:1479–1514, 1998.

[187] A. V. Prokofiev, A. I. Shelykh, and B. T. Melekh. Periodicity in the band gap variation of Ln_2X_3 (X = O, S, Se) in the lanthanide series. *J. Alloys Compd.*, 242:41–44, 1996.

[188] L. Köhler and G. Kresse. Density functional study of CO on Rh(111). *Phys. Rev. B*, 70:165405, 2004.

[189] A. Sekiyama, T. Iwasaki, K. Matsuda, Y. Saitoh, Y. Ônuki, and S. Suga. Probing bulk states of correlated electron systems by high-resolution resonance photoemission. *Nature*, 403:396–398, 2000.

[190] R. Gillen, S. J. Clark, and J. Robertson. Nature of the electronic band gap in lanthanide oxides. *Phys. Rev. B*, 87:125116, 2013.

[191] B. Li, A. Michaelides, and M. Scheffler. Density functional theory study of flat and stepped NaCl(001). *Phys. Rev. B*, 76:075401, 2007.

[192] P. S. Bagus, E. S. Ilton, and C. J. Nelin. The interpretation of XPS spectra: insights into materials properties. *Surf. Sci. Rep.*, 68:273–304, 2013.

[193] Y. Lykhach, S. M. Kozlov, T. Skála, A. Tovt, V. Stetsovych, N. Tsud, F. Dvořák, V. Johánek, A. Neitzel, J. Mysliveček, S. Fabris, V. Matolín, K. M. Neyman, and J. Libuda. Counting electrons on supported nanoparticles. *Nat. Mater.*, 15:284–288, 2015.

[194] J. Shi, A. Schaefer, A. Wichmann, M. M. Murshed, T. M. Gesing, A. Wittstock, and M. Bäumer. Nanoporous gold-supported ceria for the water–gas shift reaction: UHV inspired design for applied catalysis. *J. Phys. Chem. C*, 118:29270–29277, 2014.

[195] A. Khare, R. J. Choudhary, K. Bapna, D. M. Phase, and S. P. Sanyal. Resonance photoemission studies of (111) oriented CeO_2 thin film grown on Si(100) substrate by pulsed laser deposition. *J. Appl. Phys.*, 108:103712, 2010.

[196] D. C. Grinter, C. Muryn, A. Sala, C.-M. Yim, C. L. Pang, T. O. Menteş, A. Locatelli, and G. Thornton. Spillover reoxidation of ceria nanoparticles. *J. Phys. Chem. C*, 120:11037–11044, 2016.

List of Abbreviations

ARPES	angle-resolved photoemission spectroscopy
BIS	bremsstrahlung isochromat spectroscopy
ceria	cerium oxide
DFT	density functional theory
FWHM	full width at half maximum
GGA	generalized gradient approximation
ISS	ion scattering spectroscopy
ICSD	Inorganic Crystal Structure Database
IR	infrared spectroscopy
I–V	intensity–voltage
LDA	local-density approximation
LEED	low-energy electron diffraction
LEEM	low-energy electron microscopy
PAW	projected augmented wave
PCD	Pearson's Crystal Data
PES	photoemission spectroscopy
PEEM	photoemission electron microscopy
redox	reduction–oxidation
RPES	resonant photoemission spectroscopy
SIE	self-interaction error
STM	scanning tunneling microscopy
UHV	ultra-high vacuum
XAS	X-ray absorption spectroscopy
XMCD	X-ray magnetic circular dichroism
XPS	X-ray photoelectron spectroscopy

Attachments

1. Implementation of photoelectron spectroscopy analysis in Fytik

```
class FuncVoigt4L : public Function
{
    DECLARE_FUNC_OBLIGATORY_METHODS(Voigt4L, Function)
    bool get_height(realt* a) const { *a = av_[0]; return
       ↪ true; }
    bool get_fwhm(realt* a) const { *a = 0.5346*av_[2]+
       ↪ sqrt(0.2166*av_[2]*av_[2]+av_[3]*av_[3]); return
       ↪  true; }
};

class FuncVoigt4Lsh : public Function
{
    DECLARE_FUNC_OBLIGATORY_METHODS(Voigt4Lsh, Function)
    bool get_height(realt* a) const { *a = av_[0]; return
       ↪ true; }
    bool get_fwhm(realt* a) const { *a = 0.5346*av_[2]+
       ↪ sqrt(0.2166*av_[2]*av_[2]+av_[3]*av_[3]); return
       ↪  true; }
};

class FuncVoigt4Lbg : public Function
{
    DECLARE_FUNC_OBLIGATORY_METHODS(Voigt4Lbg, Function)
    bool get_area(realt* a) const;
    bool get_height(realt* a) const { *a = av_[0]; return
       ↪ true; }
    bool get_fwhm(realt* a) const { *a = 0.5346*av_[2]+
       ↪ sqrt(0.2166*av_[2]*av_[2]+av_[3]*av_[3]); return
       ↪  true; }
};

CALCULATE_VALUE_BEGIN(FuncVoigt4L)
        double X_val = (x - av_[1])*2*sqrt(log(2))/av_[3];
        double Y_val = av_[2]*sqrt(log(2))/av_[3];

        double voigt_A[4] =
           ↪ {-1.2150,-1.3509,-1.2150,-1.3509};
        double voigt_B[4] =
           ↪ {1.2359,0.3786,-1.2359,-0.3786};
        double voigt_C[4] =
           ↪ {-0.3085,0.5906,-0.3085,0.5906};
        double voigt_D[4] =
           ↪ {0.0210,-1.1858,-0.0210,1.1858};
```

```
        double partialSum = 0;

        for(int j = 0; j < 4; j++)
        {
                partialSum += (voigt_C[j]*(Y_val-voigt_A[j
                    ↪ ])+voigt_D[j]*(X_val-voigt_B[j]))/((
                    ↪ Y_val-voigt_A[j])*(Y_val-voigt_A[j])
                    ↪ +(X_val-voigt_B[j])*(X_val-voigt_B[j
                    ↪ ]));
        }
CALCULATE_VALUE_END((av_[2]*av_[0]*sqrt(M_PI)*sqrt(log(2))
    ↪ /av_[3])*partialSum)

CALCULATE_DERIV_BEGIN(FuncVoigt4L)
        double X_val = (x - av_[1])*2*sqrt(log(2))/av_[3];
        double Y_val = av_[2]*sqrt(log(2))/av_[3];
        double constant = av_[2]*av_[0]*sqrt(M_PI)*sqrt(
            ↪ log(2))/av_[3];

        double voigt_A[4] =
            ↪ {-1.2150,-1.3509,-1.2150,-1.3509};
        double voigt_B[4] =
            ↪ {1.2359,0.3786,-1.2359,-0.3786};
        double voigt_C[4] =
            ↪ {-0.3085,0.5906,-0.3085,0.5906};
        double voigt_D[4] =
            ↪ {0.0210,-1.1858,-0.0210,1.1858};

        double alpha[4], beta[4];
        double partialSum = 0, V = 0, dVdx = 0, dVdy = 0;

        for(int j = 0; j < 4; j++)
        {
                partialSum += (voigt_C[j]*(Y_val-voigt_A[j
                    ↪ ])+voigt_D[j]*(X_val-voigt_B[j]))/((
                    ↪ Y_val-voigt_A[j])*(Y_val-voigt_A[j])
                    ↪ +(X_val-voigt_B[j])*(X_val-voigt_B[j
                    ↪ ]));
        }

        for(int j = 0; j < 4; j++)
        {
                alpha[j]=voigt_C[j]*(Y_val-voigt_A[j])+
                    ↪ voigt_D[j]*(X_val-voigt_B[j]);
                beta[j]=(Y_val-voigt_A[j])*(Y_val-voigt_A[
                    ↪ j])+(X_val-voigt_B[j])*(X_val-
                    ↪ voigt_B[j]);
                V+=alpha[j]/beta[j];
```

```
                dVdx+=(voigt_D[j]*beta[j]-2.0*(X_val-
                    ↪ voigt_B[j])*alpha[j])/(beta[j]*beta[
                    ↪ j]);
                dVdy+=(voigt_C[j]*beta[j]-2.0*(Y_val-
                    ↪ voigt_A[j])*alpha[j])/(beta[j]*beta[
                    ↪ j]);
        }
        dy_dx = constant*dVdx*2*sqrt(log(2))/av_[3];
        dy_dv[0] = constant*V/av_[0];
        dy_dv[1] = constant*dVdx*(-2*sqrt(log(2))/av_[3]);
        dy_dv[2] = constant*(V/av_[2]+dVdy*sqrt(log(2))/
            ↪ av_[3]);
        dy_dv[3] = -constant*V/av_[3]+constant*dVdx*((x-
            ↪ av_[1])*2*sqrt(log(2)))*(-1/(av_[3]*av_[3]))
            ↪ +constant*dVdy*(av_[2]*sqrt(log(2))*(-1/(av_
            ↪ [3]*av_[3])));
CALCULATE_DERIV_END((av_[2]*av_[0]*sqrt(M_PI)*sqrt(log(2))
    ↪ /av_[3])*partialSum)

CALCULATE_VALUE_BEGIN(FuncVoigt4Lsh)
        double X_val = (x - av_[1])*2*sqrt(log(2))/av_[3];
        double Y_val = av_[2]*sqrt(log(2))/av_[3];
        double constant = av_[2]*av_[0]*sqrt(M_PI)*sqrt(
            ↪ log(2))/av_[3];

        double voigt_A[4] =
            ↪ {-1.2150,-1.3509,-1.2150,-1.3509};
        double voigt_B[4] =
            ↪ {1.2359,0.3786,-1.2359,-0.3786};
        double voigt_C[4] =
            ↪ {-0.3085,0.5906,-0.3085,0.5906};
        double voigt_D[4] =
            ↪ {0.0210,-1.1858,-0.0210,1.1858};

        double partialSum = 0;
        double background = 0;

        for(int j = 0; j < 4; j++)
        {
                double Abar = voigt_C[j]*(Y_val-voigt_A[j
                    ↪ ])-voigt_D[j]*voigt_B[j];
                double Bbar = voigt_D[j];
                double Cbar = (Y_val-voigt_A[j])*(Y_val-
                    ↪ voigt_A[j]);
                double Dbar = voigt_B[j];
                double Substitution = (x - av_[1])*2*sqrt(
                    ↪ log(2))/av_[3];
```

```
                partialSum += (voigt_C[j]*(Y_val-voigt_A[j
                    ↪ ])+voigt_D[j]*(X_val-voigt_B[j]))/((
                    ↪ Y_val-voigt_A[j])*(Y_val-voigt_A[j])
                    ↪ +(X_val-voigt_B[j])*(X_val-voigt_B[j
                    ↪ ]));
                background += -Abar*atan((Dbar-
                    ↪ Substitution)/sqrt(Cbar))/sqrt(Cbar)
                    ↪ +Bbar*( 0.5*log(Cbar+(Dbar-
                    ↪ Substitution)*(Dbar-Substitution))-
                    ↪ Dbar*atan((Dbar-Substitution)/sqrt(
                    ↪ Cbar))/sqrt(Cbar) )-0.0*(Abar+Dbar)
                    ↪ *(M_PI/2)/sqrt(Cbar);
        }
CALCULATE_VALUE_END(constant*partialSum+av_[4]*constant*
    ↪ av_[3]*(1/(2*sqrt(log(2))))*background)

CALCULATE_DERIV_BEGIN(FuncVoigt4Lsh)
        double X_val = (x - av_[1])*2*sqrt(log(2))/av_[3];
        double Y_val = av_[2]*sqrt(log(2))/av_[3];
        double constant = av_[2]*av_[0]*sqrt(M_PI)*sqrt(
            ↪ log(2))/av_[3];

        double voigt_A[4] =
            ↪ {-1.2150,-1.3509,-1.2150,-1.3509};
        double voigt_B[4] =
            ↪ {1.2359,0.3786,-1.2359,-0.3786};
        double voigt_C[4] =
            ↪ {-0.3085,0.5906,-0.3085,0.5906};
        double voigt_D[4] =
            ↪ {0.0210,-1.1858,-0.0210,1.1858};

        double alpha[4], beta[4];
        double partialSum = 0, V = 0, dVdx = 0, dVdy = 0;
        double background = 0, dbglwidth = 0, dbgpos = 0,
            ↪ dbgx = 0, dbggwidth = 0;

        for(int j = 0; j < 4; j++)
        {
                partialSum += (voigt_C[j]*(Y_val-voigt_A[j
                    ↪ ])+voigt_D[j]*(X_val-voigt_B[j]))/((
                    ↪ Y_val-voigt_A[j])*(Y_val-voigt_A[j])
                    ↪ +(X_val-voigt_B[j])*(X_val-voigt_B[j
                    ↪ ]));
                background += voigt_C[j]*(-M_PI/2)+(
                    ↪ voigt_D[j]/2)*(-log( (Y_val-voigt_A[
                    ↪ j])*(Y_val-voigt_A[j])+((x-av_[1])
                    ↪ *2*sqrt(log(2))/av_[3]-voigt_B[j])
                    ↪ *((x-av_[1])*2*sqrt(log(2))/av_[3]-
```

```
    ↪ voigt_B[j]) ))+voigt_C[j]*(Y_val-
    ↪ voigt_A[j])*(-atan((x-av_[j])*2*sqrt
    ↪ (log(2))/(av_[3]*(Y_val-voigt_A[j]))
    ↪ -voigt_B[j]/(Y_val-voigt_A[j]))/(
    ↪ Y_val-voigt_A[j]));

alpha[j]=voigt_C[j]*(Y_val-voigt_A[j])+
    ↪ voigt_D[j]*(X_val-voigt_B[j]);
beta[j]=(Y_val-voigt_A[j])*(Y_val-voigt_A[
    ↪ j])+(X_val-voigt_B[j])*(X_val-
    ↪ voigt_B[j]);
V+=alpha[j]/beta[j];
dVdx+=(voigt_D[j]*beta[j]-2.0*(X_val-
    ↪ voigt_B[j])*alpha[j])/(beta[j]*beta[
    ↪ j]);
dVdy+=(voigt_C[j]*beta[j]-2.0*(Y_val-
    ↪ voigt_A[j])*alpha[j])/(beta[j]*beta[
    ↪ j]);

dbglwidth+=av_[4]*constant*av_[3]*(1/(2*
    ↪ sqrt(log(2))))*( (-voigt_D[j]/2)
    ↪ *(2*(Y_val-voigt_A[j])*sqrt(log(2))/
    ↪ av_[3])/((Y_val-voigt_A[j])*(Y_val-
    ↪ voigt_A[j])+((x-av_[1])*2*sqrt(log
    ↪ (2))/av_[3]-voigt_B[j])*((x-av_[1])
    ↪ *2*sqrt(log(2))/av_[3]-voigt_B[j]))
    ↪ + (-voigt_C[j])*( -((x-av_[1])*2*
    ↪ sqrt(log(2))-voigt_B[j]*av_[3]) * (
    ↪ sqrt(log(2))) / ( ((x-av_[1])*2*sqrt
    ↪ (log(2))-voigt_B[j]*av_[3])*((x-av_
    ↪ [1])*2*sqrt(log(2))-voigt_B[j]*av_
    ↪ [3])+av_[3]*av_[3]*(Y_val-voigt_A[j
    ↪ ])*(Y_val-voigt_A[j]) ) ) );
dbgx+=av_[4]*constant*av_[3]*(1/(2*sqrt(
    ↪ log(2))))*( (-voigt_D[j]/2)*(2*( (x-
    ↪ av_[1])*2*sqrt(log(2))/av_[3]-
    ↪ voigt_B[j] )*2*sqrt(log(2))/av_[3])
    ↪ /((Y_val-voigt_A[j])*(Y_val-voigt_A[
    ↪ j])+((x-av_[1])*2*sqrt(log(2))/av_
    ↪ [3]-voigt_B[j])*((x-av_[1])*2*sqrt(
    ↪ log(2))/av_[3]-voigt_B[j])) + (-
    ↪ voigt_C[j])*( (av_[3]*(Y_val-voigt_A
    ↪ [j])*(2*sqrt(log(2)))) / ( ((x-av_
    ↪ [1])*2*sqrt(log(2))-voigt_B[j]*av_
    ↪ [3])*((x-av_[1])*2*sqrt(log(2))-
    ↪ voigt_B[j]*av_[3])+av_[3]*av_[3]*(
    ↪ Y_val-voigt_A[j])*(Y_val-voigt_A[j])
    ↪ ) ) );
```

```
                dbgpos+=av_[4]*constant*av_[3]*(1/(2*sqrt(
                    ↪ log(2))))*( (-voigt_D[j]/2)*(2*( (x-
                    ↪ av_[1])*2*sqrt(log(2))/av_[3]-
                    ↪ voigt_B[j] )*(-2)*sqrt(log(2))/av_
                    ↪ [3]) /((Y_val-voigt_A[j])*(Y_val-
                    ↪ voigt_A[j])+((x-av_[1])*2*sqrt(log
                    ↪ (2))/av_[3]-voigt_B[j])*((x-av_[1])
                    ↪ *2*sqrt(log(2))/av_[3]-voigt_B[j]))
                    ↪ + (-voigt_C[j])*( (av_[3]*(Y_val-
                    ↪ voigt_A[j]) * (-2*sqrt(log(2)))) / (
                    ↪  ((x-av_[1])*2*sqrt(log(2))-voigt_B[
                    ↪ j]*av_[3])*((x-av_[1])*2*sqrt(log(2)
                    ↪ )-voigt_B[j]*av_[3])+av_[3]*av_[3]*(
                    ↪ Y_val-voigt_A[j])*(Y_val-voigt_A[j])
                    ↪  ) ) );
                dbggwidth+=av_[4]*constant*av_[3]*(1/(2*
                    ↪ sqrt(log(2))))*( (-voigt_D[j]/2)*(
                    ↪ 2*(Y_val-voigt_A[j])*(-av_[2]*sqrt(
                    ↪ log(2))/(av_[3]*av_[3]))+2*((x-av_
                    ↪ [1])*2*sqrt(log(2))/av_[3]-voigt_B[i
                    ↪ ])*(-(x-av_[1])*2*sqrt(log(2))*(1/(
                    ↪ av_[3]*av_[3])) ) )/((Y_val-voigt_A[
                    ↪ j])*(Y_val-voigt_A[j])+((x-av_[1])
                    ↪ *2*sqrt(log(2))/av_[3]-voigt_B[j])
                    ↪ *((x-av_[1])*2*sqrt(log(2))/av_[3]-
                    ↪ voigt_B[j])) + (-voigt_C[j])*( (
                    ↪ voigt_A[j]*(x-av_[1])*2*sqrt(log(2))
                    ↪ -voigt_B[j]*av_[2]*sqrt(log(2))) / (
                    ↪  ((x-av_[1])*2*sqrt(log(2)))*((x-av_
                    ↪ [1])*2*sqrt(log(2)))-2*((x-av_[1])
                    ↪ *2*sqrt(log(2)))*voigt_B[j]*av_[3]+
                    ↪ av_[3]*av_[3]*(voigt_B[j]*voigt_B[j
                    ↪ ]+voigt_A[j]*voigt_A[j])+av_[2]*av_
                    ↪ [2]*log(2)-2*voigt_A[j]*av_[2]*av_
                    ↪ [3]*sqrt(log(2)) ) ) );
}

dy_dx = constant*dVdx*2*sqrt(log(2))/av_[3]+dbgx;
dy_dv[0] = constant*V/av_[0]+av_[4]*constant*av_
    ↪ [3]*(1/(2*sqrt(log(2))))*background/av_[0];
dy_dv[1] = constant*dVdx*(-2*sqrt(log(2))/av_[3])+
    ↪ dbgpos;
dy_dv[2] = constant*(V/av_[2]+dVdy*sqrt(log(2))/
    ↪ av_[3])+av_[4]*constant*av_[3]*(1/(2*sqrt(
    ↪ log(2))))*background/av_[2]+dbglwidth;
dy_dv[3] = -constant*V/av_[3]+constant*dVdx*((x-
    ↪ av_[1])*2*sqrt(log(2)))*(-1/(av_[3]*av_[3]))
    ↪ +constant*dVdy*(av_[2]*sqrt(log(2))*(-1/(av_
```

```
            ↪ [3]*av_[3]))+dbggwidth;
        dy_dv[4] = constant*av_[3]*(1/(2*sqrt(log(2))))*
            ↪ background;
CALCULATE_DERIV_END((av_[2]*av_[0]*sqrt(M_PI)*sqrt(log(2))
    ↪ /av_[3])*partialSum+av_[4]*constant*av_[3]*(1/(2*
    ↪ sqrt(log(2))))*background)

CALCULATE_VALUE_BEGIN(FuncVoigt4Lbg)
        double X_val = (x - av_[1])*2*sqrt(log(2))/av_[3];
        double Y_val = av_[2]*sqrt(log(2))/av_[3];
        double constant = av_[2]*av_[0]*sqrt(M_PI)*sqrt(
            ↪ log(2))/av_[3];

        double voigt_A[4] =
            ↪ {-1.2150,-1.3509,-1.2150,-1.3509};
        double voigt_B[4] =
            ↪ {1.2359,0.3786,-1.2359,-0.3786};
        double voigt_C[4] =
            ↪ {-0.3085,0.5906,-0.3085,0.5906};
        double voigt_D[4] =
            ↪ {0.0210,-1.1858,-0.0210,1.1858};

        double partialSum = 0;
        double background = 0;
        double background2 = 0;
        double bg2_aTan = 0;
        double bg2_bTan = 0;
        double bg2_aLog = 0;
        double bg2_bLog = 0;

        for(int j = 0; j < 4; j++)
        {
                partialSum += (voigt_C[j]*(Y_val-voigt_A[j
                    ↪ ])+voigt_D[j]*(X_val-voigt_B[j]))/((
                    ↪ Y_val-voigt_A[j])*(Y_val-voigt_A[j])
                    ↪ +(X_val-voigt_B[j])*(X_val-voigt_B[j
                    ↪ ]));
                background += voigt_C[j]*(-M_PI/2)+(
                    ↪ voigt_D[j]/2)*(-log( (Y_val-voigt_A[
                    ↪ j])*(Y_val-voigt_A[j])+((x-av_[1])
                    ↪ *2*sqrt(log(2))/av_[3]-voigt_B[j])
                    ↪ *((x-av_[1])*2*sqrt(log(2))/av_[3]-
                    ↪ voigt_B[j]) ))+voigt_C[j]*(Y_val-
                    ↪ voigt_A[j])*(-atan((x-av_[j])*2*sqrt
                    ↪ (log(2))/(av_[3]*(Y_val-voigt_A[j]))
                    ↪ -voigt_B[j]/(Y_val-voigt_A[j]))/(
                    ↪ Y_val-voigt_A[j]));
```

```
                bg2_aTan = 2*sqrt(log(2))/(av_[3]*(Y_val-
                    ↪ voigt_A[j]));
                bg2_bTan = av_[1]*2*sqrt(log(2))/(av_[3]*(
                    ↪ Y_val-voigt_A[j]))+voigt_B[j]/(Y_val
                    ↪ -voigt_A[j]);
                bg2_aLog = (Y_val-voigt_A[j])*(Y_val-
                    ↪ voigt_A[j]);
                bg2_bLog = av_[1]*2*sqrt(log(2))/av_[3]+
                    ↪ voigt_B[j];

                background2 += (-M_PI/2)*voigt_C[j]*x-
                    ↪ voigt_C[j]*((log(bg2_aTan*bg2_aTan*x
                    ↪ *x-2*bg2_aTan*bg2_bTan*x+bg2_bTan*
                    ↪ bg2_bTan+1)-2*(bg2_bTan-bg2_aTan*x)*
                    ↪ atan(bg2_bTan-bg2_aTan*x))/(-2*
                    ↪ bg2_aTan))-(voigt_D[j]/2)*(-(
                    ↪ bg2_bLog-x)*(log(bg2_aLog+(bg2_bLog-
                    ↪ x)*(bg2_bLog-x))-2)-2*sqrt(bg2_aLog)
                    ↪ *atan((bg2_bLog-x)/(sqrt(bg2_aLog)))
                    ↪ );
        }
CALCULATE_VALUE_END((av_[2]*av_[0]*sqrt(M_PI)*sqrt(log(2))
    ↪ /av_[3])*partialSum+av_[4]*constant*av_[3]*(1/(2*
    ↪ sqrt(log(2))))*background+av_[5]*constant*av_
    ↪ [3]*(1/(2*sqrt(log(2))))*(background2-1))

CALCULATE_DERIV_BEGIN(FuncVoigt4Lbg)
        double X_val = (x - av_[1])*2*sqrt(log(2))/av_[3];
        double Y_val = av_[2]*sqrt(log(2))/av_[3];
        double constant = av_[2]*av_[0]*sqrt(M_PI)*sqrt(
            ↪ log(2))/av_[3];

        double voigt_A[4] =
            ↪ {-1.2150,-1.3509,-1.2150,-1.3509};
        double voigt_B[4] =
            ↪ {1.2359,0.3786,-1.2359,-0.3786};
        double voigt_C[4] =
            ↪ {-0.3085,0.5906,-0.3085,0.5906};
        double voigt_D[4] =
            ↪ {0.0210,-1.1858,-0.0210,1.1858};

        double alpha[4], beta[4];
        double partialSum = 0, V = 0, dVdx = 0, dVdy = 0;
        double background = 0, dbglwidth = 0, dbgpos = 0,
            ↪ dbgx = 0, dbggwidth = 0;

        for(int j = 0; j < 4; j++)
        {
```

```
partialSum += (voigt_C[j]*(Y_val-voigt_A[j
    ↪ ])+voigt_D[j]*(X_val-voigt_B[j]))/((
    ↪ Y_val-voigt_A[j])*(Y_val-voigt_A[j])
    ↪ +(X_val-voigt_B[j])*(X_val-voigt_B[j
    ↪ ]));
background += voigt_C[j]*(-M_PI/2)+(
    ↪ voigt_D[j]/2)*(-log( (Y_val-voigt_A[
    ↪ j])*(Y_val-voigt_A[j])+((x-av_[1])
    ↪ *2*sqrt(log(2))/av_[3]-voigt_B[j])
    ↪ *((x-av_[1])*2*sqrt(log(2))/av_[3]-
    ↪ voigt_B[j]) ))+voigt_C[j]*(Y_val-
    ↪ voigt_A[j])*(-atan((x-av_[j])*2*sqrt
    ↪ (log(2))/(av_[3]*(Y_val-voigt_A[j]))
    ↪ -voigt_B[j]/(Y_val-voigt_A[j]))/(
    ↪ Y_val-voigt_A[j]));

alpha[j]=voigt_C[j]*(Y_val-voigt_A[j])+
    ↪ voigt_D[j]*(X_val-voigt_B[j]);
beta[j]=(Y_val-voigt_A[j])*(Y_val-voigt_A[
    ↪ j])+(X_val-voigt_B[j])*(X_val-
    ↪ voigt_B[j]);
V+=alpha[j]/beta[j];
dVdx+=(voigt_D[j]*beta[j]-2.0*(X_val-
    ↪ voigt_B[j])*alpha[j])/(beta[j]*beta[
    ↪ j]);
dVdy+=(voigt_C[j]*beta[j]-2.0*(Y_val-
    ↪ voigt_A[j])*alpha[j])/(beta[j]*beta[
    ↪ j]);

dbglwidth+=av_[4]*constant*av_[3]*(1/(2*
    ↪ sqrt(log(2))))*( (-voigt_D[j]/2)
    ↪ *(2*(Y_val-voigt_A[j])*sqrt(log(2))/
    ↪ av_[3])/((Y_val-voigt_A[j])*(Y_val-
    ↪ voigt_A[j])+((x-av_[1])*2*sqrt(log
    ↪ (2))/av_[3]-voigt_B[j])*((x-av_[1])
    ↪ *2*sqrt(log(2))/av_[3]-voigt_B[j]))
    ↪ + (-voigt_C[j])*( -((x-av_[1])*2*
    ↪ sqrt(log(2))-voigt_B[j]*av_[3]) * (
    ↪ sqrt(log(2))) / ( ((x-av_[1])*2*sqrt
    ↪ (log(2))-voigt_B[j]*av_[3])*((x-av_
    ↪ [1])*2*sqrt(log(2))-voigt_B[j]*av_
    ↪ [3])+av_[3]*av_[3]*(Y_val-voigt_A[j
    ↪ ])*(Y_val-voigt_A[j]) ) ) );
dbgx+=av_[4]*constant*av_[3]*(1/(2*sqrt(
    ↪ log(2))))*( (-voigt_D[j]/2)*(2*( (x-
    ↪ av_[1])*2*sqrt(log(2))/av_[3]-
    ↪ voigt_B[j] )*2*sqrt(log(2))/av_[3])
    ↪ /((Y_val-voigt_A[j])*(Y_val-voigt_A[
```

```
                ↪ j])+((x-av_[1])*2*sqrt(log(2))/av_
                ↪ [3]-voigt_B[j])*((x-av_[1])*2*sqrt(
                ↪ log(2))/av_[3]-voigt_B[j])) + (-
                ↪ voigt_C[j])*( (av_[3]*(Y_val-voigt_A
                ↪ [j])*(2*sqrt(log(2)))) / ( ((x-av_
                ↪ [1])*2*sqrt(log(2))-voigt_B[j]*av_
                ↪ [3])*((x-av_[1])*2*sqrt(log(2))-
                ↪ voigt_B[j]*av_[3])+av_[3]*av_[3]*(
                ↪ Y_val-voigt_A[j])*(Y_val-voigt_A[j])
                ↪ ) ) );
            dbgpos+=av_[4]*constant*av_[3]*(1/(2*sqrt(
                ↪ log(2))))*( (-voigt_D[j]/2)*(2*( (x-
                ↪ av_[1])*2*sqrt(log(2))/av_[3]-
                ↪ voigt_B[j] )*(-2)*sqrt(log(2))/av_
                ↪ [3])/((Y_val-voigt_A[j])*(Y_val-
                ↪ voigt_A[j])+((x-av_[1])*2*sqrt(log
                ↪ (2))/av_[3]-voigt_B[j])*((x-av_[1])
                ↪ *2*sqrt(log(2))/av_[3]-voigt_B[j]))
                ↪ + (-voigt_C[j])*( (av_[3]*(Y_val-
                ↪ voigt_A[j]) * (-2*sqrt(log(2)))) / (
                ↪ ((x-av_[1])*2*sqrt(log(2))-voigt_B[
                ↪ j]*av_[3])*((x-av_[1])*2*sqrt(log(2)
                ↪ )-voigt_B[j]*av_[3])+av_[3]*av_[3]*(
                ↪ Y_val-voigt_A[j])*(Y_val-voigt_A[j])
                ↪ ) ) );
            dbggwidth+=av_[4]*constant*av_[3]*(1/(2*
                ↪ sqrt(log(2))))*( (-voigt_D[j]/2)*(
                ↪ 2*(Y_val-voigt_A[j])*(-av_[2]*sqrt(
                ↪ log(2))/(av_[3]*av_[3]))+2*((x-av_
                ↪ [1])*2*sqrt(log(2))/av_[3]-voigt_B[i
                ↪ ])*(-(x-av_[1])*2*sqrt(log(2))*(1/(
                ↪ av_[3]*av_[3])) ))/((Y_val-voigt_A[
                ↪ j])*(Y_val-voigt_A[j])+((x-av_[1])
                ↪ *2*sqrt(log(2))/av_[3]-voigt_B[j])
                ↪ *((x-av_[1])*2*sqrt(log(2))/av_[3]-
                ↪ voigt_B[j])) + (-voigt_C[j])*( (
                ↪ voigt_A[j]*(x-av_[1])*2*sqrt(log(2))
                ↪ -voigt_B[j]*av_[2]*sqrt(log(2))) / (
                ↪ ((x-av_[1])*2*sqrt(log(2)))*((x-av_
                ↪ [1])*2*sqrt(log(2)))-2*((x-av_[1])
                ↪ *2*sqrt(log(2)))*voigt_B[j]*av_[3]+
                ↪ av_[3]*av_[3]*(voigt_B[j]*voigt_B[j
                ↪ ]+voigt_A[j]*voigt_A[j])+av_[2]*av_
                ↪ [2]*log(2)-2*voigt_A[j]*av_[2]*av_
                ↪ [3]*sqrt(log(2)) ) ) );
    }

    dy_dx = constant*dVdx*2*sqrt(log(2))/av_[3]+dbgx;
```

```
        dy_dv[0] = constant*V/av_[0]+av_[4]*constant*av_
            ↪ [3]*(1/(2*sqrt(log(2))))*background/av_[0];
        dy_dv[1] = constant*dVdx*(-2*sqrt(log(2))/av_[3])+
            ↪ dbgpos;
        dy_dv[2] = constant*(V/av_[2]+dVdy*sqrt(log(2))/
            ↪ av_[3])+av_[4]*constant*av_[3]*(1/(2*sqrt(
            ↪ log(2))))*background/av_[2]+dbglwidth;
        dy_dv[3] = -constant*V/av_[3]+constant*dVdx*((x-
            ↪ av_[1])*2*sqrt(log(2)))*(-1/(av_[3]*av_[3]))
            ↪ +constant*dVdy*(av_[2]*sqrt(log(2))*(-1/(av_
            ↪ [3]*av_[3])))+dbggwidth;
        dy_dv[4] = constant*av_[3]*(1/(2*sqrt(log(2))))*
            ↪ background;
        dy_dv[5] = 0; //DEFINE!
CALCULATE_DERIV_END((av_[2]*av_[0]*sqrt(M_PI)*sqrt(log(2))
    ↪ /av_[3])*partialSum+av_[4]*constant*av_[3]*(1/(2*
    ↪ sqrt(log(2))))*background)

bool FuncVoigt4Lbg::get_area(realt* a) const
{
        double constant = av_[2]*av_[0]*sqrt(M_PI)*sqrt(
            ↪ log(2))/av_[3];
        double voigt_C[4] =
            ↪ {-0.3085,0.5906,-0.3085,0.5906};
        double areaSum = 0;
        for(int i = 0; i < 4; i++)
        {
                areaSum += M_PI*voigt_C[i]*constant*av_
                    ↪ [3]/(2*sqrt(log(2)));
        }
        *a = areaSum;
        return true;
}
```